Ivo Samuel
Caniceiro Azenha

Síntese, caraterização e modelação de membranas zeolíticas para separação de gases

Synthesis, characterization and modeling of zeolitic membranes for gas separation

**Ivo Samuel
Caniceiro Azenha**

Síntese, caraterização e modelação de membranas zeolíticas para separação de gases

Synthesis, characterization and modeling of zeolitic membranes for gas separation

o júri

Presidente   Prof.ª Doutora Maria Inês Purcell de Portugal Branco
Professora Auxiliar do Departamento de Química da Universidade de Aveiro

Doutor João Manuel do Paço Quesado Delgado
Investigador Auxiliar do Centro de Estudos da Construção da Faculdade de Engenharia da Universidade do Porto

Prof. Doutor Carlos Manuel Santos da Silva
Professor Auxiliar do Departamento de Química da Universidade de Aveiro (orientador)

agradecimentos

O meu agradecimento a todos os que ao longo do semestre direta ou indiretamente me ajudaram e incentivaram a desenvolver estre trabalho, em especial:

Ao meu orientador, Doutor Carlos Manuel Santos da Silva, pela oportunidade, apoio e incentivo incondicionais e sobretudo amizade.

Ao meu co-orientador, Simão Pedro Cardoso, pela amizade e paciência ao longo do semestre.

A todo o grupo EgiChem pelos bons momentos, companheirismo e pelas oportunidades de aprendizagem proporcionadas.

Ao meu amigo, Sérgio Manuel Santos, pela ajuda na revisão da escrita da tese e pelas discussões produtivas, bons momentos.

À Diana Branco pelo carinho, incentivo e apoio demonstrado, estando sempre presente em todos os momentos.

Finalmente, à minha família por todo o apoio e incentivo ao longo deste percurso académico, que, sem a sua presença, jamais teria sido percorrido.

palavras-chave

membranas, separação gasosa, zeólitos, titanossilicatos, modelação, Maxwell-Stefan

resumo

O interesse por membranas inorgânicas tem crescido significativamente devido a propriedades notáveis como a elevada estabilidade mecânica, térmica e química, e a capacidade de efetuarem separações seletivas assentes na afinidade e diâmetro moleculares, atuando como *peneiros moleculares*.

Os objetivos principais deste trabalho foram: (i) a aplicação do formalismo de Maxwell-Stefan (MS) à permeação de gases em membranas zeolíticas de forma a explorar o seu potencial puramente preditivo; (ii) o desenvolvimento de novos fatores termodinâmicos de MS para as isotérmicas de Dubinin-Astakhov e Dubinin-Radushkevich; (iii) a modelação da permeação de água em membranas zeolíticas 13X e 4A, precedida de um estudo rigoroso da influência dos dados de equilíbrio e das difusividades efetivas sobre os resultados; (iv) síntese e caracterização de membranas de titanossilicato AM-3 (Aveiro-Manchester número três) para separação de gases.

No que respeita à preparação das membranas de AM-3, estas foram sintetizadas hidrotermicamente em suportes tubulares de α-alumina pelo método de crescimento secundário. Observou-se a formação do filme de AM-3 por difração de raios X e microscopia eletrónica de varrimento. Efetuou-se ainda um estudo de pH tendo-se observado que na gama de concentrações em causa não se conseguiu obter uma fase pura de AM-3. A caracterização dinâmica da membrana de AM-3 mostrou a existência de macro e/ou meso defeitos devido à permeância (do hélio) diminuir com o aumento da temperatura. A realização de ciclos consecutivos de aquecimento e arrefecimento permitiu aumentar os valores de permeância.

Relativamente à modelação foram derivados pela primeira vez os fatores termodinâmicos de MS para as isotérmicas de Dubinin-Astakhov e Dubinin-Radushkevich. Estes foram validados com sucesso, usando dados de metano e etano em membrana de silicalite-1. Os resultados mostraram que estes fatores são simultaneamente capazes de correlacionar a permeação de gases puros e prever, a partir deles, a separação de misturas binárias, o que é um feito notável nesta área de investigação. As difusividades do metano e etano são essencialmente independentes da concentração no sólido.

A permeação de água através de membranas de zeólitos 13X e 4A foi prevista usando a abordagem de MS. A influência da temperatura e da carga do sólido sobre as difusividades efetivas foi previamente modelada, tendo-se observado comportamentos muito distintos e não lineares nos dois materiais. Os resultados evidenciaram fluxos mais elevados para o zeólito 13X (devido ao maior tamanho de poro), que diminuem com o aumento da temperatura. No caso do zeólito 4A o comportamento foi o oposto.

keywords

abstract

The interest on inorganic membranes has been growing significantly due to their remarkable properties like mechanical, thermal and chemical stabilities, and the ability to perform selective separations based on the kinetic diameter and surface affinity, acting as molecular sieves.

The main objectives of this work were: (i) the application of the Maxwell-Stefan (MS) formalism to gas permeation through zeolite-type membranes in order to explore its potential as purely predictive tool; (ii) the development of new MS thermodynamic factors for the Dubinin-Astakhov and Dubinin-Radushkevich isotherms, since they are fundamental in the field of microporous materials; (iii) modeling water permeation through zeolites 13X and 4A membranes after accurate analysis of the influence of isotherm data and effective diffusivity upon permeation; (iv) synthesis and characterization of AM-3 (Aveiro Manchester number 3) titanosilicate membranes for gas separation.

Regarding membranes preparation, they were synthesized hydrothermally up to three consecutive times on tubular α-alumina supports through a secondary growth technique. Through X-ray diffraction and scanning electron microscopy it was possible to conclude that after three depositions the AM-3 becomes clearly evident. The influence of pH was also studied and it was verified that a pure phase of AM-3 was not obtained. The dynamic characterization of the membrane disclosed the existence of macro and/or meso-defects, since helium permeances decreased with increasing temperature. The consecutive heating and cooling cycles were able to enhance gas permeance values.

Concerning modeling, the MS thermodynamic factors of Dubinin-Astakhov and Dubinin-Radushkevich isotherms were derived for the first time. These factors were successfully validated using published data for methane and ethane on a silicalite-1 membrane. The results showed they are simultaneously able to correlate pure gas permeation and are capable of predicting binary mixture separation, which is a much more important achievement in this field. It was also disclosed that the methane and ethane diffusivities are essentially independent of the fractional occupancy.

The water permeation through zeolites 13X and 4A membranes was predicted using MS approach. The influence of temperature and solid loading upon the effective diffusivities was previously modeled, being possible to observe very distinct and non-linear behaviors for both materials. The results evidenced higher fluxes for zeolite 13X, due to its higher pore size. Moreover the flux decreases with increasing temperature, being the opposite verified for the zeolite 4A membrane.

Contents

List of Figures

List of Tables

Nomenclature

Acronyms

AARD   Absolute Average Relative Deviation

BPR   Back pressure regulator

DA   Dubinin-Astakhov

DR   Dubinin-Radushkevich

DGS   Dusty Gas Model

GC   Gas chromatograph

MFC   Mass Flow Controller

MS   Maxwell-Stefan

SSS   Sodium silicate solution

SMR   Steam Methane Reforming

TC   Temperature Controller

WK   Wicke-Kallenbach

Greek Symbols

μ Chemical potential (J mol^{-1})

θ Fractional occupancy

λ Mean free path (m)

δ Membrane thickness (m)

Π_i Permeance of species i (mol m^{-2} s^{-1} Pa^{-1})

ε Porosity

$\alpha_{i,j}$ Separation factor of species i over j

α Separation factor or constant parameter of the Langmuir-Freundlich and Toth isotherms

ρ, ρ_p Solid density (kg m^{-3})

Γ Thermodynamic factor

τ Tortuosity

η Viscosity (Pa s)

Subscripts

Kn   Knudsen

LF   Langmuir-Freundlich

N   Nitta

0   Reference condition

sat   Saturation

i, j Species i, j

T   Toth

List of Symbols

E_a Activation energy (J mol^{-1})

V_m^0 Adsorbate molar volume (m^3 mol^{-1})

b Adsorption parameter (Pa^{-1})

b_0 Adsorption parameter at the temperature T_0 (Pa^{-1})

q Amount of adsorbed species (mol kg^{-1})

P_m Arithmetic mean pressure (Pa)

R   Gas constant (J mol^{-1} K^{-1})

d_k Kinetic diameter (m)

$Đ$ Maxwell-Stefan diffusivity (m^2 s)

$\bar{u}$ Mean velocity of diffusing species (m s^{-1})

W_0 Micropore volume (m^3 kg^{-1})

N Molar flux (mol m^{-2} s^{-1})

y Molar fraction on the permeate side

x Molar fraction on the retentate side

M Molecular weight (kg mol^{-1})

d_p Pore diameter (m)

D Self diffusion coefficient (m^2 s^{-1})

$[B]$ Square matrix of inverted Maxwell-Stefan diffusivities (m^2 s^{-1})

A Surface area (m^2)

T Temperature (K)

P Total Pressure (Pa)

Chapter 1

Introduction

The problem of air pollution is reaching limits of considerable dangerousness for both humans and surrounding environment, being the direct consequence of the continuous release of combustion products provided by energy systems employing, specially, fossil fuels. In this context, hydrogen may play an important role, since its combustion with pure oxygen produces only water.

Hydrogen may be stored both in liquid or gas forms and be later converted into thermal energy and electricity with high conversion efficiency. Thus, it can be seen as a clean energy carrier.

Despite being the most abundant element, hydrogen does not occur in nature in molecular form with the same abundance. Therefore it must be produced in some way. Actually, hydrogen may be produced in several ways: starting from fossil sources by reforming and gasification processes; starting from renewable sources by electrolysis, gasification or pyrolysis, and by exploiting nuclear energy by appropriate thermo-chemical processes [1, 2].

Currently the dominant industrial method to produce hydrogen is the well established steam methane reforming (SMR) process [3]. Natural gas reforming is the most efficient, economical and widely used process for hydrogen production. SMR is a catalytic process that involves a reaction between natural gas, or other light hydrocarbons, and steam at high temperatures, $700 - 1000$ ℃ and pressures of $3 - 25$ bar. The products are hydrogen, carbon monoxide and carbon dioxide, and to obtain a high degree of purity, further separation processes are required. The hydrogen purification, however, requires high energy input [4].

The coupling of a reaction system with a membrane may present enormous advantages when the chemical process is limited by equilibrium. In such cases, the removal of one of the main products may drive the reaction towards its completion, improving hydrogen production or achieving the same conversions for lower temperatures. Furthermore, if the membrane is highly selective for the hydrogen, the costs associated with its purification can be considerably reduced. In conclusion, membrane reactors (MR) allow a desired cost reduction because of this process intensification and reaction yields enhancement. In this context, zeolite and

1

zeolite-type membranes, with their uniform pore size distribution and superior thermal and chemical stability over the well established palladium membranes, may play an important role towards a hydrogen economy, i.e. an economy where the hydrogen is the main energy carrier in the supply cycle [4].

Modeling is then a fundamental tool to interpret experimental data, predict dynamic behavior of any process, optimize its operating conditions and perform the scale up from laboratory to industrial scale. In this context the versatile Maxwell-Stefan formalism is the most recommended approach to describe multicomponent transport.

Structure of the Thesis

This document is divided into six chapters. In Chapter 2 the fundamentals of membrane processes are briefly presented followed by a more detailed description of inorganic membranes, where synthesis and some characterization techniques are focused. This chapter provides a global overview of the topics covered in this work.

Chapter 3 describes the mass transport mechanisms and phenomena prevailing in microporous materials, first for single gases and then for multicomponent systems, where the Maxwell-Stefan formalism is presented. This chapter is indispensable for modeling, representing and interpreting the results obtained in chapter 5.

Chapter 4 presents the experimental set-up and the membrane synthesis procedures adopted here.

Chapter 5 contains all the modeling and experimental results. The modeling results are first presented. New expressions for the thermodynamic factors for Dubinin-Astakhov and Dubinin-Radushkevich isotherms were derived, used to describe single component diffusion of methane and ethane on a silicalite-1 membrane and with the pure data extracted (diffusivities), the binary permeation of those components was totally predicted. Additionally the influence of the surface loading upon the diffusivities was assessed. Continuing in the modeling, the water permeation was totally predicted, using diffusion and adsorption data present in the literature, through a membrane of zeolite 13x and 4A using the Maxwell-Stefan equations. The experimental results are then presented. AM-3 synthesis and its characterization was the subject of all of the experimental section.

The major conclusions and some of the future work are presented in the last chapter, the chapter 6.

Chapter 2

Membrane Processes

In membrane processes, a semipermeable barrier (the membrane) is the responsible for the partial separation of a feed consisting of a mixture of two or more components under the action of a driving force. As a result, the feed mixture is fractioned into a retentate (the part of the feed that does not pass through the membrane) and a permeate (the part of the feed that actually permeates through the membrane). Additionally a sweep agent (a liquid or a gas) can be employed in order to facilitate the removal of the permeate, as depicted in figure 2.1 [5, 6].
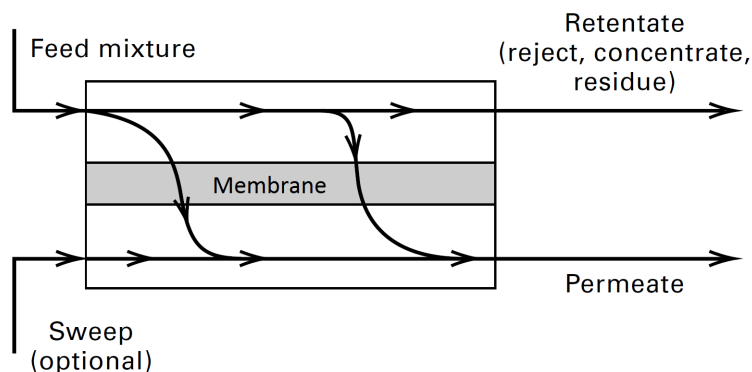
Figure 2.1: General layout of a membrane module (adapted from [6]).

According to the driving force one may have different membrane processes. Thus, it is possible to distinguish between microfiltration, ultrafiltration, nanofiltration, dialysis, electrodialysis, reverse osmosis, gas permeation and pervaporation.

Membrane processes have some interesting features over the traditional ones. The separation can be carried out continuously, they require low energy consumption, they are easily combined with other separation processes, the scale-up is usually easy to accomplish, and no additives are required [5]. The replacement of some of the existent processes with membrane separations has the potential of reducing costs and save energy. However, to be a

well succeeded technology it needs, for example, the production of a high-mass-transfer flux, defect-free and durable membranes on a large scale and the fabrication of compact and economical modules of high surface area per unit volume. Additionally it may require a previous stage to clean or purify the feed stream and it is also necessary to control carefully the operating conditions to prevent the degradation of the membrane functionality due to fouling, caking or plugging [5, 6].

Generally, the products in the feed stream are miscible and a high degree of separation is hard to achieve. A wide variety of materials can be used as semipermeable barriers, ranging from nonporous (dense) polymeric films to porous polymeric, ceramic or metal materials or even a liquid, gel or gas [6].

Due to the different possible barriers and to obtain a more informative understanding, the membranes should be grouped and classified according to their characteristics. One first possible and clear classification is related with their nature: they can be natural or synthetic. It is an important first classification since the structure and functionality of each group are entirely different and consequently it is a determining key aspect in the the performance of a given membrane [5, 7]. Although out of the scope of this thesis, the natural membranes can be further divided into living and non-living membranes. On the other hand, the synthetic membranes can be divided into organic (polymeric or liquid) and inorganic membranes (e.g., metal, ceramic, and zeolite type materials). Synthetic membranes can be grouped according to their morphology or structure. Concerning their structure they can be symmetric or asymmetric. This two classes can be further subdivided as represented in figure 2.2. With respect to their morphology they can be classified into dense (non-porous) or porous membranes. The porous membranes are macroporous ($d_\mathrm{p} > 50$ nm), mesoporous ($2 < d_\mathrm{p} < 50$ nm) or microporous ($d_\mathrm{p} < 2$ nm), following the IUPAC classification [5, 7, 8].
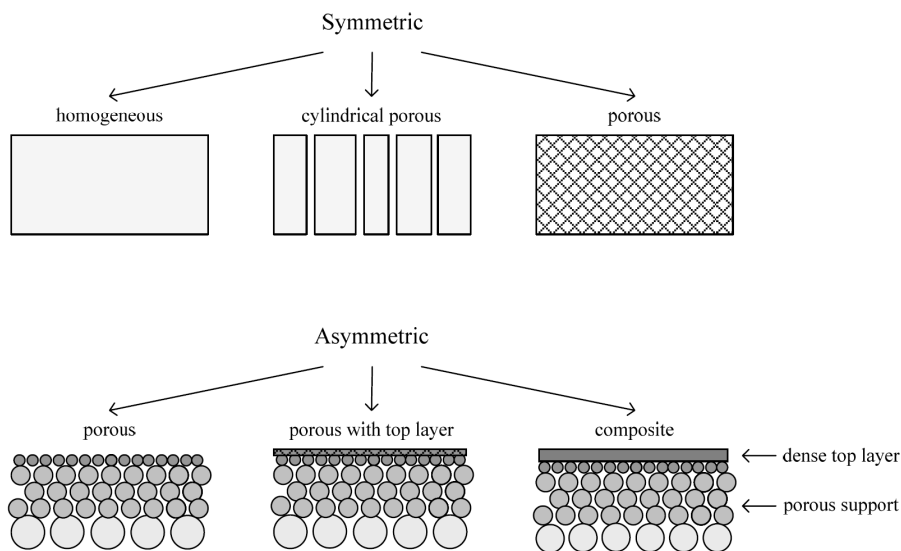
Figure 2.2: Inorganic membrane structures (adapted from [9]).

4

Symmetric membranes (or isotropic) are made out of a single material and have one morphological structure. They are usually thick in order to overcome mechanical limitations and the resistance to mass transfer is determined by the total thickness. On the other hand, asymmetric membranes can be composed by various layers with decreasing pore size and different morphologies combined with a supporting system. If a thin dense top layer is present, the final membrane has the high selectivity characteristic of a dense membrane combined with the high permeation rate of a porous membrane [5, 8].

In order to use membranes on an industrial scale, large surface areas are usually required. The simplest unit in which the membrane is assembled is called module. Depending on the shape of the membrane they can be assembled into different type of modules, being the performance of each module different. All the different modules arise from two essential shapes of membranes: flat and tubular. Plate-and-frame and spiral-wound modules involve flat membranes whereas tubular, capillary and hollow-fiber modules stem from tubular membrane configurations [5, 6].

To provide a good separation and to be economically advantageous over other processes, membranes should exhibit: a high selectivity and high permeance. These two key parameters are commonly used to describe the performance of a given membrane. The selectivity describes the capacity of a given component to permeate over the other components while the permeance is related with the permeation rate and determines its production. These two parameters are opposite to each other. Having both high selectivity and high permeance is not always possible. However, for example, low selectivity can be compensated with a multistage process and low permeance with an increase of surface area [6]. The molar transmembrane flux of species i across the membrane can be defined by the following relation

$$N_i = \frac{P_{M,i}}{\delta} \times (\text{driving force}) = \Pi_i \times (\text{driving force}) \qquad (2.1)$$

where $P_{M,i}$ is the permeability of species i, δ is the thickness of the membrane and Π_i is the permeance. For gases at sufficiently low pressures one may use the partial pressure difference across the membrane as the driving force resulting in

$$N_i = \frac{P_{M,i}}{\delta} \times (p_{f,i} - p_{p,i}) = \Pi_i \times (x_i P_f - y_i P_p) \qquad (2.2)$$

where subscripts f and p stand for feed and permeate, respectively, P is the total pressure and x_i and y_i are the molar fractions of i in the feed and in the permeate, respectively [5, 6]. The membrane selectivity towards a mixture is usually expressed in terms of a separation factor. For a mixture with components i an j the separation factor is defined by

$$\alpha_{i/j} = \frac{y_i \times x_j}{y_j \times x_i} \qquad (2.3)$$

The value of $\alpha_{i,j}$ is chosen in such a way that its value is greater than the unity. If $\alpha_{i/j} = \alpha_{j/i}$ no separation is achieved. It should be noted that in real gaseous mixtures the real separation factor is not equal to the ideal separation factor given by:

$$\alpha_{i/j,ideal} = \frac{\Pi_i}{\Pi_j} \tag{2.4}$$

$\alpha_{i/j,ideal}$ is defined for the limiting situation of very high feed pressure, o.e. $P_f > P_p$. Nonetheless, the ideal values present in the literature can be used as a starting point for the selection of the membrane material [5].

2.1 Inorganic Membranes

In principle, all kinds of different synthetic materials can be used for preparing membranes. The basic principle involved is to modify the material by means of an appropriate technique so as to obtain a membrane with proper morphology for a given separation. The selection of the material will determine the separation principle allowed, i.e., not every kind of separation can be performed with every kind of material [5].

Inorganic materials generally possess superior chemical and thermal stabilities relative to polymeric materials. Their use as membranes started in the separation of nuclear fuels by Knudsen flow through porous ceramic membranes. Among all different inorganic materials, three types can be easily distinguished: ceramic membranes, glass membranes, and metallic membranes. The ceramic membranes are formed by combining a metal with a non-metal in the form of an oxide, nitride or carbide. They form the main class of inorganic membranes. Metal membranes, for instance, result from sintering metal powders, e.g., tungsten, molybdenum or palladium. Glass membranes (silica, SiO_2) are usually prepared by leaching techniques on demixed glasses [5, 8].

Inorganic materials are much more tolerant with respect to pH than the polymeric ones, being able to handle a wide range of solvents and pH values. Another important aspect is the ease of cleaning especially in high fouling applications. In contrast to polymeric membranes, inorganic materials can be cleaned with many kinds of agents and for much longer periods [5]. Concerning temperature stability, the fact that they can be used under harsher environments allows the coupling of a membrane system with a chemical reaction, where the membrane itself can act as catalyst as well as a selective barrier to one of the components. Mechanical strength is one parameter to take into account if the process involves high pressures or if the membrane is self supported. Despite their high tensile modulus, they are usually very brittle [5].

Among the most studied microporous inorganic membranes are the amorphous metal oxides and the zeolite-type materials. While the first ones suffer from hydrothermal instability,

the last group exhibit a much higher thermal and hydrothermal robustness.

2.1.1 Zeolite Membranes

The name of zeolite was firstly introduced by the Swedish mineralogist Axel Fredrick who, back in 1756, first saw that stilbite, a natural mineral, lost water when heated. Thus, zeolite derives from the classical Greek and means "boiling stone".

Zeolite and zeolite-like materials do not comprise an easily definable family of crystaline solids. Zeolites are three-dimensional microporous crystalline solids with a well defined structure and cavities in the molecular range. Although classically defined as crystalline hydrated aluminosilicates, the definition of zeolites has sometimes been expanded to include aluminophosphates, silicoaluminophosphates, gallosilicates, titanosilicates, metallo-sulfides, metallo-oxides, etc [10, 11]. Their structure consists of a three-dimensional network of TO_4 tetrahedra (T=Si,Al) linked to each other by shared oxygen atoms [12]. An isolated SiO_4 group contains a charge of -4 while it is neutral in a solid containing an O/Si ratio of two since each oxygen atom is connected with two Si atoms. Since the AlO_4 unit charge is -1, globally, the zeolite carries a negative net charge, which is neutralized by extra-framework cations, usually from the Groups I and II of periodic table [8, 9, 12]. The combination of tetrahedral SiO_4 and AlO_4 allows the zeolite to have a monodisperse pore size distribution and a higher mechanical strength compared with amorphous materials. In addition to the extra-framework cations, water molecules may also be present in the cavities of the zeolite. Thus, a zeolite can be seen as having three components

$$M^{z+}_{n/m} \qquad [Si_{1-n}Al_nO_2] \qquad nH_2O$$

Extra-framework cations   Zeolite framework   Sorbed water molecules
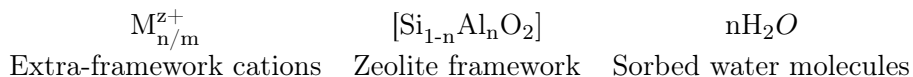
Their framework is comprised of assemblies of TO_4 in which the vertices are shared to form secondary building units (SBUs) (figure 2.3). The secondary units are invariably non-chiral and a unit cell always contains an integral number of them. This SBUs are interconnected to form a wide range of polyhedra which in turn generate the infinitely extended frameworks of the various crystal structures [11].

Another classification that simplifies comparisons in terms of adsorptive, molecular sieving and catalytic behavior is according to their pore dimensions, being small (6-,8- and 9-membered rings), medium (10- membered rings), large (12- membered rings) and ultra-large pore materials (14-,18- and 20- membered rings) as illustrated in figure 2.4 [13].

The remarkable properties of zeolites account for their extensive use in a wide range of applications. Molecular sieving or size exclusion is the capacity to perform a separation based on the different size and shape of molecules. While a given molecule with a dimension inferior to the pore diameter is able to get into and pass through the zeolite structure, a larger molecule will be rejected and will not cross through the zeolite. This is a inherent
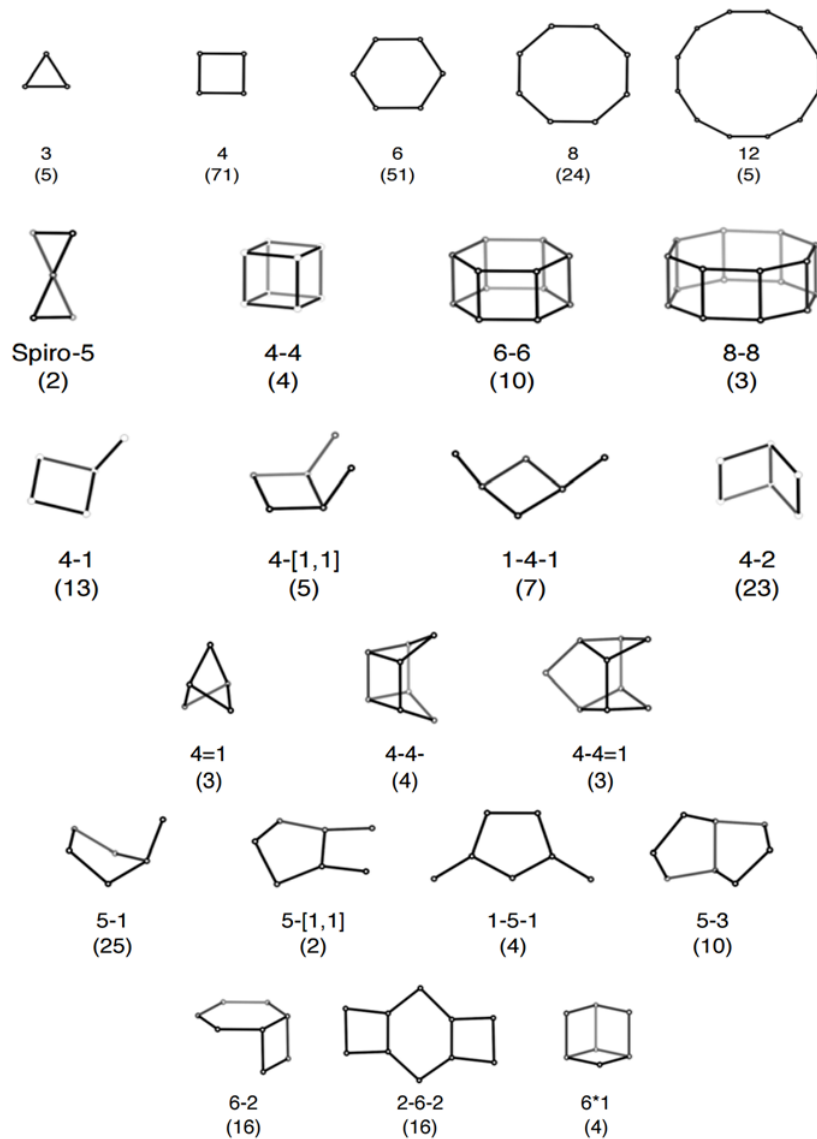
Figure 2.3: Secondary Building Units.
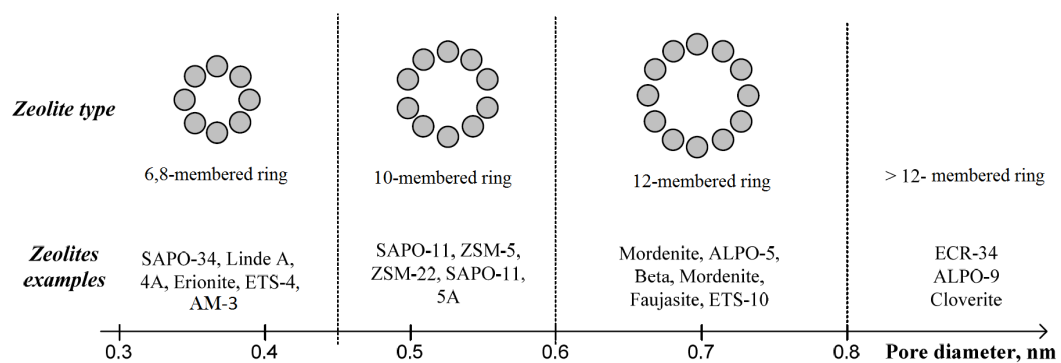
Figure 2.4: Zeolite pore size classification (adapted from [9]).

characteristic of zeolite and zeolite-type materials, and the separation can be so sharp that molecules even with sub-Å differences can be separated.

Ion exchange is another characteristic associated to zeolite and zeolite-type materials. The extraframework cations can be exchanged by other cations changing the stability, adsorption, selectivity and catalytic abilities. Thus, according to the desired properties, zeolites can be fine-tuned to their final application.

Their high internal surface area, high thermal stability and the previous stated characteristics makes them suitable for a wide range of applications, namely, decontamination of gaseous streams, removal of heavy metals from the environment, catalysis and as water softening agents [8, 12, 14, 15].

2.1.2 Zeolite Membrane Synthesis

Zeolite membranes can be divided into three categories: polymer-zeolite composite membranes, self-supported membranes and supported membranes. The latter are by far the most widely used type of membranes. Various types of supports can be used but in most cases, zeolite membranes are synthesized upon a macroporous alumina support. When selecting a support its thermal and chemical resistances to the synthesis media as well as the difference in thermal expansion coefficients are important factors to have in mind. In addition its roughness is also another important parameter. Sometimes, if the surface of the support is not suited to synthesize a defect-free membrane, an intermediate thin layer with a narrow pore-size distribution is often deposited previously on the support [8, 16].

There are three main ways to synthesize supported zeolite membranes: the in-situ direct crystallization, the dry or wet gel method and the seeding and secondary growth method.

In-situ direct crystallization

The wide application of this method is based on its simplicity, since it is one-step process where the requirement for specially designed substrates as well as a seeding step is eliminated [17]. The membrane is synthesized under autogenous pressure, occurring the nucleation and growth of the crystals on the surface of the support grains. A relatively thin zeolite layer is formed on the surface and in the pores of the support and therefore, additional hydrothermal synthesis are required to get a good quality membrane. One limitation of this method is the long induction period and the homogeneous nucleation which alter the membrane quality. Additionally, the reproducibility is also another limitation [8, 18, 19].

Dry or wet gel method

It involves the deposition of an aluminosilicate gel over the support and the following crystallization under vapors of trimethylamine, ethylenediamine and water. This type of synthesis method prevents homogeneous nucleation, improving controllability and reducing

chemical consumption, being more attractive for large scale production. The zeolite films formed suffer often from cracks and other defects due to the large volume shrinkage during the transformation from gel to zeolite [18].

Seeding and secondary growth

This last method involves the growth of a layer of seed crystals previously synthesized and deposited on the support. The support with the zeolite seed layer is then brought into contact with the zeolite synthesis solution, growing into a continuous film. It is considered one of the most attractive and flexible methods for orienting the formation of consolidated thin membranes [18, 20]. It eliminates one source of irreproducibility by going directly to crystal growth, avoiding complex processes that occur in the early stages of the crystal growth, allowing not only the expansion of the range of synthesis compositions but also the use of dilute sols. In addition, the derived membranes are generally highly permeable and selective. Nowadays, the secondary seeded growth method has become the prominent path for the preparation of zeolite membranes and is the most versatile and flexible approach. Generally involves more steps but it gives a better control of the zeolite membrane quality [19].

2.1.3 Titanosilicates

Since the first discover of titanosilicate TS-1, the synthesis of titanosilicate molecular sieves has attracted considerable research attention [21]. The structure of these materials consists of interlinked octahedral and tetrahedral forming well defined three dimensional frameworks with channels of molecular dimensions [22, 23]. Thus, similarly to zeolites, they are able to perform separations based on the size and shape of molecules. Besides, they offer several other advantages over classical zeolite membranes, namely: (i) in general, a pure phase may be obtained in the absence of costly organic templates, avoiding calcination treatments, which sometimes are the source of defects and/or loss of active surface groups; (ii) they are usually prepared under relatively mild pH conditions, reducing the chemical attack on the support surfaces; (iii) the mixed octahedral-tetrahedral oxides present novel possibilities of isomorphous framework substitution allowing the fine tuning of the catalytic and adsorption properties of a given membrane, while preserving its microporous structure; (iv) in general they possess a high basicity, complementing, in some way, the acid properties of classical zeolites [14, 22].

AM-3 (Aveiro Manchester number 3) is a microporous titanosilicate analogous to the natural mineral penkvilksite found in Mont Saint-Hilaire, Québec (Canada), and the Kola Peninsula (Russia), with an ideal formula $Na_4Ti_2SiO_2 2.5H_2O$ [23]. Its structure consists of SiO_4 tetrahedra connected by individual TiO_6 octahedra forming a three-dimensional framework of 6-ring channels which are partially occupied by sodium cations and water molecules (figure 2.5) [22].
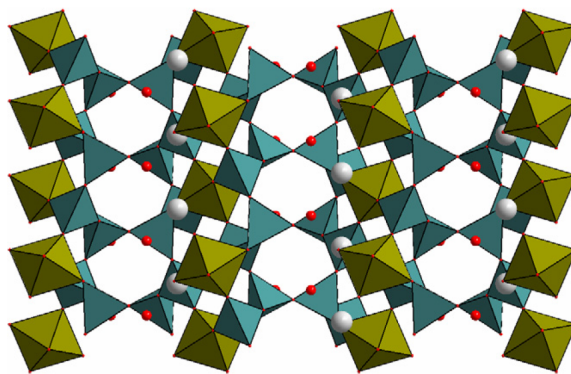
Figure 2.5: Polyhedral representation of AM-3 structure viewed along [2 0 0] direction. Large and small circles depict, respectively, sodium ions and water molecules.

AM-3 adsorbs nitrogen in a low extent but copious amounts of water being reversibly dehydrated. Moreover, the synthesis of AM-3 is environmentally friendly, in the sense that no templates are used and the pH is moderate. In figure 2.6 scanning electron micrograph images of AM-3 are presented [22, 24].
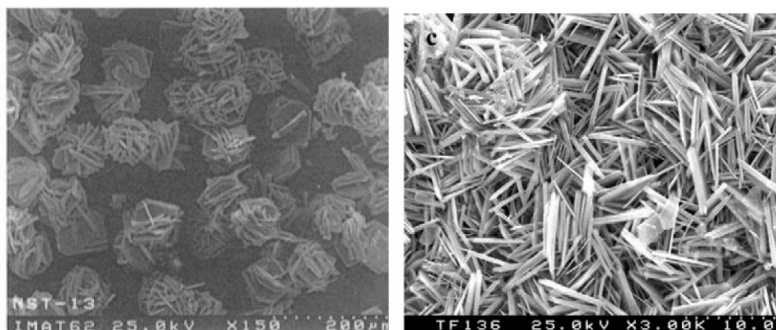
Figure 2.6: SEM images of AM-3.

2.2 Characterization Methods

The development of efficient methods able to evaluate membrane quality is a key aspect for large scale applications. Due to the diversity of materials there is no universal method to characterise all of them and frequently more than one method is applied simultaneously to obtain a detailed insight. Two different types of methods are generally used: static and dynamic methods. While the static methods allow the study of the physico-chemical properties, the dynamic ones allow the detection of defects on the membrane which, in turn, can compromise its performance [16].

Static Methods

The techniques applied in powder characterization can also be applied to the characterization of membranes. X-Ray Diffraction (XRD) and Scanning Electron Microscopy (SEM)

are by far the most used techniques [25]. Concerning zeolites, XRD is able to identify the zeotype formed and the present impurities. The orientation of the crystals formed can also be studied. SEM, in its turn, can be used to analyze the crystals, i.e., their size and shape, their distribution along the support and the thickness, homogeneity and adhesion of the zeolite layer [8, 16, 25].

Dynamic Methods

Gas permeation measurements of pure gases or multicomponent mixtures are required in order to evaluate the quality and the performance of the membrane. These measurements provide useful information about the effective pore structure and the existence of intercrystaline defects. In addition, the measurement of the permeances of several gases as a function of temperature can be used to find the permeation mechanism through the membrane in terms of two phenomena: adsorption and/or diffusion [9, 16]. Additionally, the transient gas permeation through a membrane can also be used to measure its effective thickness in a non-destructive way [26].

The permeation of gaseous mixtures will determine for instance the capacity of a membrane to perform the desired separation, being the ultimate test to apply to a given membrane.

Chapter 3

Gas Adsorption and Transport Phenomena in Porous Membranes

Prediction and correlation of permeation and separation behavior requires knowledge on single and multicomponent diffusion, adsorption and structure parameters. Understanding mass transport mechanisms is essential for accurate modeling of permeances, which is then fundamental to interpret experimental data, predict the dynamic behavior of any process, optimize operating conditions and scale-up from laboratory to large scale utilization. Thus, modeling is fundamental for the interpretation of experimental data and as a simulation tool.

3.1 Single gas permeation

According to the pore size diameter (d_p), several transport mechanisms can be distinguished. When $d_\mathrm{p} > 50$ nm, viscous flow dominates and the fluid flows as a whole, being the collisions between molecules much more important than the collisions between molecules and pore surface. As the pore size decreases ($2 < d_\mathrm{p} < 50$ nm), the last interactions become more frequent, the mean free path of a molecule becomes similar or slightly larger than the pore diameter and the flow pattern falls in the Knudsen regime. In small micropores ($d_\mathrm{p} < 2$ nm), due to their dimensions, molecules are not so free as in the viscous or Knudsen regimes, and collisions between molecules and pore walls are dominant. Thus, molecules may never completely escape from the surface force field and the diffusion becomes an activated process. Here, if the interactions between molecules and surface is strong enough, molecules may lose their gaseous identity and the diffusion is called surface diffusion [7]. If the interactions are not so strong, molecules remain their gaseous state and the diffusion is called activated gaseous diffusion. Therefore, in micropores and mesopores collisions between molecules and pore surface are fundamental, while in macropores those collisions can be neglected [27]. In figure 3.1 the referred mechanisms are illustrated.
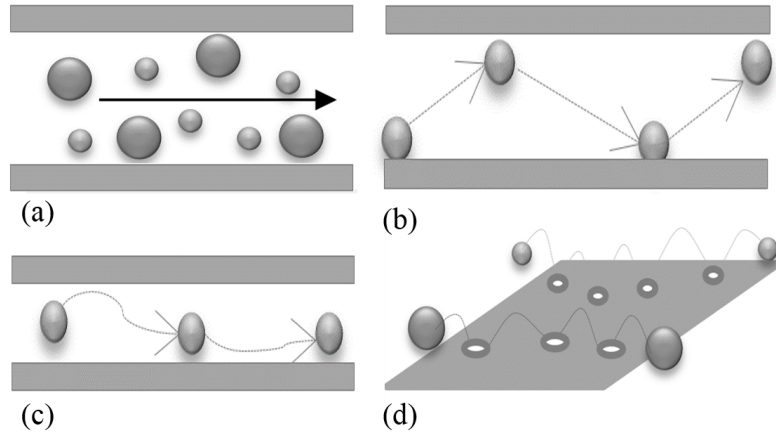
Figure 3.1: Transport mechanisms in porous media: (a) viscous flow; (b) Knudsen diffusion; (c) activated gaseous diffusion; (d) surface diffusion (adapted from [27]).

3.1.1 Viscous Flow

In the case of viscous flow, the molar flux under a pressure gradient can be described by a Hagen-Poiseuille type law:

$$J_{\mathrm{v}} = -\frac{\varepsilon}{\tau}\frac{d_{\mathrm{p}}^2}{32\eta}\frac{P}{RT}\frac{dP}{dz} \tag{3.1}$$

where μ is the gas viscosity, P and T are the total pressure and temperature, respectively, R is the ideal gas constant, z is the spatial coordinate, and ε and τ are the porosity and tortuosity, respectively. The integration of the last equation, under steady-state conditions, allows the determination of the permeance over the whole membrane thickness δ:

$$\Pi_{\mathrm{v}} = \frac{\varepsilon}{\tau}\frac{d_{\mathrm{p}}^2}{32\eta}\frac{P_{\mathrm{m}}}{RT\delta} \tag{3.2}$$

where P_{m} is the arithmetic mean pressure between the two sides of the membrane. Through these last two equations one may regard that under viscous flow the permeance increases with pressure and declines with temperature due to the presence not only of variable T but also due to the viscosity [27].

3.1.2 Knudsen diffusion

Knudsen diffusivity, D_{Kn}, may be expressed by the product between a geometric factor (1/3), a characteristic length (pore diameter) and the velocity of gas molecules. Since the pore is a three-dimensional structure, only the molecules moving towards the desired direction are considered, thus, the incorporation of the factor 1/3:

$$D_{\mathrm{Kn}} = \frac{d_{\mathrm{p}}}{3}\left(\frac{8RT}{\pi M}\right)^{1/2} \tag{3.3}$$

14

where M is the molar mass of the diffusing gas. Combining the last equation with Fick's first law allows the determination of the Knudsen diffusion flux, which is given by

$$J_{\text{Kn}} = -\frac{\varepsilon d_{\text{p}}}{3\tau} \left(\frac{8}{\pi RTM} \right)^{1/2} \frac{dP}{dz} \tag{3.4}$$

and the integration over the whole membrane thickens δ gives the Knudsen diffusion permeance

$$\Pi_{\text{Kn}} = \frac{\varepsilon d_{\text{p}}}{3\tau\delta} \left(\frac{8}{\pi RTM} \right)^{1/2} \tag{3.5}$$

The introduction of the factor ε/τ accounts for structural effects. Through equation 3.5 one may see that the permeance is pressure-independent, decreases with increasing temperature and molecular weight [7, 19, 27].

3.1.3 Diffusion on Micropores

As mentioned above, the transport in micropores may be explained as an activated process and thus, the Fick diffusion coefficient may be expressed as:

$$D = g\bar{u}l_{\text{d}}\exp\left(\frac{-E_{\text{a}}}{RT} \right) \tag{3.6}$$

where g is a geometrical factor, $\bar{u}$ the mean velocity of diffusing species and l_{d} the diffusion length [27]. The exponential therm may be seen as the probability of a given molecule to have enough energy to overcome an energy barrier. The driving force responsible for mass transport in micropores is best seen as the chemical potential gradient. Thus, in isothermal conditions and assuming ideal gas behavior, $\mu = \mu_0 + RT\ln P$, where μ_0 is the standard chemical potential, the permeation flux of a single gas is given by

$$J = -Ð\rho_{\text{p}}q\frac{d\ln P}{dz} \tag{3.7}$$

where $Ð$ is a diffusion coefficient analogous to the Maxwell-Stefan (MS) diffusivity [27, 28, 29]. Equation 3.7 may be rearranged, introducing a thermodynamic factor $\Gamma \equiv \partial\ln P/\partial\ln q$:

$$J = -\rho_{\text{p}}\Gamma Ð\frac{\partial q}{\partial z} \tag{3.8}$$

and the integration of this last equation is only possible if the relation between P and q is known, i.e., if adsorption data are known. The Darken equation, $D = Ð\Gamma$ translates the concentration dependence of Fick diffusivity [27].

3.1.3.1 Activated gaseous diffusion

The activated transport of gaseous molecules inside the pores may be considered to occur jump by jump from site to site subjected to an energy barrier. Therefore, in a certain way it may be seen as an activated Knudsen diffusion. The diffusivity of gaseous molecules is given by:

$$D_{\text{g}} = \frac{1}{Z} l_{\text{d}} \left(\frac{8RT}{\pi M} \right)^{0.5} \exp\left(-\frac{E_{\text{a,g}}}{RT} \right) \tag{3.9}$$

where l_{d} is the diffusion length (the distance between to adjacent sites of low energy), $1/Z$ is the geometrical factor, being Z the number of adjacent sites, and $E_{\text{a,g}}$ is the activation energy [27, 30]. If it is considered that there is no formal adsorption, the flux (equation 3.10) and the permeance (equation 3.11) may be expressed in terms of pressure gradient:

$$J_{\text{g}} = -\frac{1}{Z} l_{\text{d}} \left(\frac{8}{\pi MRT} \right)^{0.5} \exp\left(-\frac{E_{\text{a,g}}}{RT} \right) \frac{dP}{dz} \tag{3.10}$$

$$\Pi_{\text{g}} = -\frac{l_{\text{d}}}{Z\delta} \left(\frac{8}{\pi MRT} \right)^{1/2} \exp\left(\frac{-E_{\text{a,g}}}{RT} \right) \tag{3.11}$$

Through this two last equations is possible to see that the gas permeance shows an exponential dependence on temperature [27].

3.1.3.2 Surface diffusion

Among the several approaches proposed to describe surface diffusion, the hopping model is the most frequently adopted, which postulates that molecules move over the surface hopping between adjacent adsorption sites. The Fick diffusivity may be expressed as

$$D_{\text{s}}(q) = \frac{l_{\text{d}}^2}{Z} v(q) \exp\left(\frac{-E_{\text{a,s}}}{RT} \right) \tag{3.12}$$

where l_{d} represents the diffusion length, $1/Z$ the geometrical factor [30] and $v(q)$ the jump frequency. Considering $D_{\text{s}}^0(q) = \frac{l_{\text{d}}^2}{Z} v(q)$ the relation between Fick and corrected diffusivities is

$$D_{\text{s}}(q) = Đ_{\text{s}}\varGamma = Đ_{\text{s}}^0 \varGamma \exp\left(\frac{-E_{\text{a,s}}}{RT} \right) \tag{3.13}$$

Finally, to determine the flux and permeance of adsorbed molecules, the isotherm must be known in order to evaluate the thermodynamic factor. The dependence of surface permeance on temperature is not so straightforward as the previous cases [27].

In real membrane systems, all the transport mechanisms may be expected to contribute to the overall permeation flux, being the total flux equal to the sum of all contributions. The transport mechanism controlling the permeation process may be discriminated from the permeation-temperature behavior. For non-adsorbable gases, diffusion is expected to increase

consistently with increasing temperature. However the presence of defects, and thus, the viscous and/or Knudsen mechanisms, causes the appearing of a minimum in the permeance since each mechanism decreases with temperature.

For strongly adsorbing species at low temperature permeance increases with temperature because diffusivity increases with temperature regardless the decrease of surface coverage (Region II, figure 3.2). At a given temperature, the decrease in the adsorbed species becomes dominant and the permeance decreases (Region III, figure 3.2) [31]. At even higher temperatures adsorption becomes negligible and permeance is expected to increase exponentially due to the nature of diffusion through micropores (Region IV, figure 3.2). Again, a minimum is usually observed at lower temperatures [27].
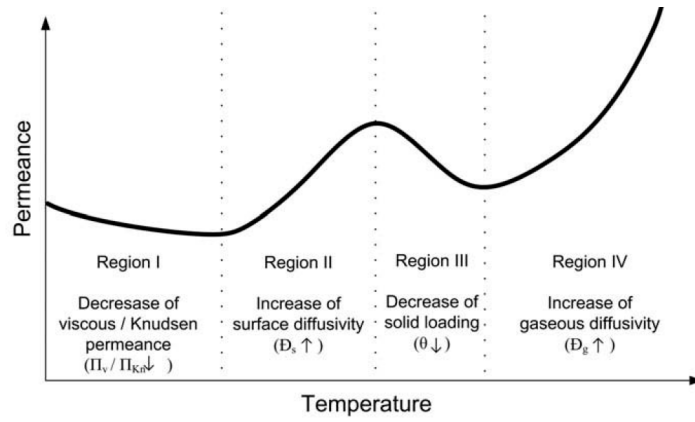
Figure 3.2: Qualitative behavior of pure gas permeance as function of temperature (adapted from [27]).

3.2 Multicomponent permeation

Three possible approaches are used to describe multicomponent mass transport, these being the Fickian formalism, the thermodynamics of irreversible processes (IT) theory, and the generalized Maxwell-Stefan (MS) equations [27].

The MS formalism is the most widely used approach and is recognized to be the most advantageous and preferable alternative. The relative simplicity and beauty lies on the fact that the MS equations are easily derived from a momentum balance on the present components [28, 32].

In order to cause a relative molecular motion in a binary mixture, a force should be exerted on each component. This force on one component is balanced by an opposite friction force due to the second component and is proportional to its relative velocity and to the molar fraction of the second species, x_2. The resulting balance may be expressed by

$$\nabla \mu_1 = \frac{RT}{D_{12}} x_2 (u_1 - u_2) \tag{3.14}$$

where u_1 and u_2 are the velocities of components 1 and 2, respectively, and $\mathcal{D}_{12}$ is the MS diffusivity describing the interaction between the two components [9]. Taking into account that $N_i = c_t x_i u_i$, where c_t if the total molar concentration, equation 3.14 may be written as

$$-\frac{x_1}{RT}\nabla\mu_1 = \frac{x_2 N_1 - x_1 N_2}{c_t \mathcal{D}_{12}} \tag{3.15}$$

Without loss of generality, the MS model presented for a binary mixture can be extended multicomponent systems expressing the balances between the chemical potential gradient of species i and the friction force exerted on i by all the remaining species j

$$-\frac{x_i}{RT}\nabla\mu_i = \sum_{\substack{j=1 \\ j\neq i}}^{n} \frac{x_j N_i - x_i N_j}{c_t \mathcal{D}_{ij}} = \sum_{\substack{j=1 \\ j\neq i}}^{n} \frac{x_j J_i - x_i J_j}{c_t \mathcal{D}_{ij}}, \ N_i = J_i + x_i N_{total} \tag{3.16}$$

In micropores, molecules are always under the influence of the surface force field. The diffusion of adsorbed species may be described assuming the surface sites as a $(n+1)^{th}$ pseudo-species of the multicomponent system, by analogy with the Dusty Gas Model (DGM). According to DGM, the porous solid is considered as a collection of stationary molecules uniformly distributed in space. Those dust molecules are considered part of the multicomponent system, forming the $(n+1)^{th}$ component [28, 29]. As a result, surface diffusion can be describe by:

$$-\frac{\theta_i}{RT}\nabla\mu_i = \sum_{\substack{j=1 \\ j\neq i}}^{n} \frac{\theta_j N_i^s - \theta_i N_j^s}{\rho_p \varepsilon q_{sat} \mathcal{D}_{ij}^s} + \frac{N_i^s}{\rho_p \varepsilon q_{sat} \mathcal{D}_i^s} \tag{3.17}$$

for molecules with equal q_{sat}, where ρ_p and ε are the matrix porosity and density, respectively. The first term on the righ-hand side in equation 3.17 represents the friction that all species exert on i while the other term represents the forces exerted by the surface on i. Thus $\mathcal{D}_{ij}^s$ expresses interaction between moving species i and j while $\mathcal{D}_i^s$ molecule-walls interactions.

Assuming equilibrium between liquid and solid, the surface chemical potential may be expressed in terms of chemical potential gradients of surface occupancy by introducing the thermodynamic factors Γ_{ij}. If additionally one considers low pressures, the following equation applies:

$$\frac{\theta_i}{RT}\nabla\mu_i = \sum_{j=1}^{n} \Gamma_{ij}\nabla\theta_j, \text{where } \Gamma_{ij} = \theta_i \frac{\partial \ln P_i}{\partial \theta_j} \tag{3.18}$$

At higher pressures fugacity should be used instead. Equations 3.18 and 3.17 may be combined and expressed in matrix form, leading to the Maxwell-Stefan model for surface diffusion:

$$(N^s) = -\rho_p \varepsilon q_{sat} [B^s]^{-1}[\Gamma](\nabla\theta) \tag{3.19}$$

being the elements of $[B^s]$ defined as follows:

$$B_{ii}^s = \frac{1}{\mathcal{D}_i^s} + \sum_{\substack{j=1 \\ j \neq i}}^{n} \frac{\theta_j}{\mathcal{D}_{ij}^s}, \ B_{ij}^s = -\frac{\theta_i}{\mathcal{D}_{ij}^s} \tag{3.20}$$

Mass transport of multicomponent mixtures may be predicted with MS equations based only on single component adsorption and diffusion data [27]. Vignes correlation (equation 3.21) provides a link between single and multicomponent mixtures:

$$\mathcal{D}_{ij}^s = \left(\mathcal{D}_i^s\right)^{\frac{\theta_i}{\theta_i + \theta_j}} \left(\mathcal{D}_j^s\right)^{\frac{\theta_j}{\theta_i + \theta_j}} \tag{3.21}$$

allowing the prediction of $\mathcal{D}_{ij}^s$ based only on pure component data, $\mathcal{D}_i^s$ and $\mathcal{D}_j^s$ [27, 28].

Maxwell-Stefan diffusivity may be easily interpreted and predicted since it can be described as an inverse of a drag coefficient, reflecting purely pair interactions in the opposite to Fick diffusivity which joins drag effects and non-ideality effects, being expected to exhibit strong composition dependece [27].

3.3   Influence of the surface loading

The MS diffusivity is frequently assumed as concentration-independent, despite being generally function of the fractional coverage (θ). Assuming that a molecule only migrates from a different site to another when it is empty a simple model to describe the loading dependence is given by the following equation

$$\mathcal{D}_i = \mathcal{D}_i^s(0)(1 - \theta_1 - \theta_2 - ... - \theta_n) \tag{3.22}$$

which is sometimes called *strong confinement scenario* (SCS) [28, 33, 34]. The term $\mathcal{D}_i^s(0)$ represents the case in which there is no influence of the surface loading, *weak confinement scenario* (WCS) described by

$$\mathcal{D}_i = \mathcal{D}_i^s(0) \tag{3.23}$$

Another possible way to describe the surface loading is provided by the quasi-chemical theory of Reed and Ehrlich [35]

$$\mathcal{D}_s(\theta) = \mathcal{D}_s(0)\frac{(1 + \varepsilon')^{z'+1}}{(1 + \varepsilon'/f)^{z'}}, \ \text{where} \tag{3.24}$$

$$f = \exp\left(\frac{\Delta E}{RT}\right), \ \varepsilon' = \frac{(\beta - 1 + 2\theta)f}{2(1 - \theta)}, \ \beta = \sqrt{1 - 4\theta(1 - \theta)(1 - f^{-1})} \tag{3.25}$$

where ΔE represents is the energy increment of the system when a new neighbor is introduced in the lattice, and the coordination number z' is the maximum number of nearest neighbors [33, 36]. The limiting case of zero loading dependence WCS cannot be reached from equation

3.24.

3.4 Adsorption and Thermodynamic Factors

Several models are available in the literature capable of describing single and multicomponent adsorption. Langmuir, Nitta, Langmuir-Freundlich, Toth, Dubinin-Raduskhevich and Dubinin-Astakhov are briefly discussed here.

Langmuir Isotherm. The Langmuir isotherm (table 3.1 and 3.2) is one of the most used approaches to describe adsorption equilibrium in microporous materials. This model is based on several basic assumptions: i) adsorption onto the surface is localized in a fixed number of well-defined sites; ii) each site can accommodate only one adsorbate molecule; iii) all sites are energetically equivalent, i.e., the surface is homogeneous; and iv) there is no interaction between adjacent adsorbed molecules.

Nitta Isotherm. Provides an extension of the Langmuir isotherm. Assumes localized monolayer adsorption at surface and allows for multisite adsorption, where each molecule may be adsorbed on n active sites. The single a multicomponent isotherm may be found in tables 3.1 and 3.2.

Langmuir-Freundlich Isotherm. In order to overcome the limitations of the Freundlich isotherm, the absence of linear behavior at low pressures and a maximum plateau for sufficiently high pressures, an empirical extension of the Freundlich model is frequently adopted, the Langmuir-Freundlich isotherm (table 3.1 and 3.2).

Toth Isoterm. Toth isotherm (table 3.1 and 3.2) satisfies both high and low pressure limits, in spite of combining features of Langmuir and Langmuir-Freundlich Isotherms.

In table 3.1 and 3.2 single and multicomponent isotherms, respectively, and their corresponding thermodynamic factors are provided [27, 37].

Table 3.1: Single-component isotherms and their corresponding thermodynamic factors [37].

Isotherm		Thermodynamic Factor
Langmuir	$\theta = \frac{q}{q_{\text{sat}}} = \frac{b_{\text{L}}P}{1+b_{\text{L}}P}$	$\Gamma = \frac{1}{1-\theta}$
Nitta	$n_{\text{Nit}}b_{\text{Nit}}P = \frac{\theta}{(1-\theta)^{n_{\text{Nit}}}}$	$\Gamma = \frac{1-\theta(1-n_{\text{Nit}})}{1-\theta}$
Langmuir-Freundlich	$\theta = \frac{q}{q_{\text{sat}}} = \frac{(b_{\text{LF}}P)^{1/n_{\text{LF}}}}{1+(b_{\text{LF}}P)^{1/n_{\text{LF}}}}$	$\Gamma = \frac{n_{\text{LF}}}{1-\theta}$
Toth	$\theta = \frac{q}{q_{\text{sat}}} = \frac{b_{\text{T}}P}{[1+(b_{\text{T}}P)^{\text{t}}]^{1/\text{t}}}$	$\Gamma = \frac{\theta^{-\text{t}}}{\theta^{-\text{t}}-1}$

Isotherm parameters usually change with temperature and thus they should not be considered constant. The b_{L}, b_{Nit}, b_{LF} and b_{T} parameters of Langmuir, Nitta, Langmuir-Freundlich

Table 3.2: Multicomponent isotherms and their corresponding binary thermodynamic factors [37].

Isotherm		Thermodynamic Factors
Langmuir	$\theta_i = \frac{b_{L,i}P_i}{1+\sum_{j=1}^N b_{L,j}P_j}$	$\Gamma_{11} = 1 + \frac{\theta_1}{1-(\theta_1+\theta_2)}$, $\Gamma_{12} = \frac{\theta_1}{1-(\theta_1+\theta_2)}$ $\Gamma_{21} = \frac{\theta_2}{1-(\theta_1+\theta_2)}$, $\Gamma_{22} = 1 + \frac{\theta_2}{1-(\theta_1+\theta_2)}$
Nitta	$n_{Nit,i}b_{Nit,i}P =$ $\frac{\theta}{(1-\sum_{j=1}^N \theta)^{n_{Nit,i}}}$	$\Gamma_{11} = \frac{\theta_1(1-n_{Nit,1})+\theta_2-1}{(\theta_1+\theta_2)-1}$, $\Gamma_{12} = -\frac{\theta_1 n_{Nit,1}}{(\theta_1+\theta_2)-1}$ $\Gamma_{21} = -\frac{\theta_2 n_{Nit,2}}{(\theta_1+\theta_2)-1}$, $\Gamma_{22} = \frac{\theta_2(1-n_{Nit,2})+\theta_1-1}{(\theta_1+\theta_2)-1}$
Langmuir -Freundlish	$\theta_i = \frac{(b_{LF,i}P_i)^{1/n_{LF,i}}}{1+\sum_{j=1}^N (b_{LF,j}P_j)^{1/n_{LF,j}}}$	$\Gamma_{11} = \frac{\theta_2-1}{(1/n_{LF,1})(\theta_1+\theta_2-1)}$, $\Gamma_{12} = -\frac{\theta_2}{(1/n_{LF,2})(\theta_1+\theta_2-1)}$ $\Gamma_{21} = -\frac{\theta_1}{(1/n_{LF,1})(\theta_1+\theta_2-1)}$, $\Gamma_{22} = \frac{\theta_1-1}{(1/n_{LF,2})(\theta_1+\theta_2-1)}$
Toth	$\theta_i = \frac{b_{T,i}P_i}{[1+\sum_{j=1}^N (b_{T,j}P_j)^{t_T}]^{1/t_T}}$	$A = (t_1 - t_2)P_1 P_2 \ln(b_{r,1}P_1)$

$$B = (t_1 - t_2)P_1 P_2 \ln(b_{t,2}P_2)$$

$$C = [A + t_T(P_1 + P_2)^2](b_{t,1}P_1)^{t_T} + B(b_{t,2}P_2)^{t_T} + t_T(P_1 + P_2)^2$$

$$D = [-B + t_T(P_1 + P_2)^2](b_{t,2}P_2)^{t_T} - A(b_{t,1}P_1)^{t_T}$$

$$E = [A + t_T(P_1 + P_2)^2](b_{t,1}P_1)^{t_T} + B(b_{t,2}P_2)^{t_T}$$

$$F = [-B + t_T(P_1 + P_2)^2](b_{t,2}P_2)^{t_T}) - A(b_{t,1}P_1)^{t_T} + t_T(P_1 + P_2)^2$$

$$\Omega = 1 + (b_{t,1}P_1)^{t_T} + (b_{t,2}P_2)^{t_T}$$

$$\Gamma_{11} = \frac{-P_1 P_2(t_1-t_2)\Omega\ln\Omega+Ct_T}{t_T^2(P_1+P_2)^2}, \quad \Gamma_{12} = \frac{[P_1 P_2(t_1-t_2)\Omega\ln\Omega+Dt_T]b_{t,1}P_1}{t_T^2(P_1+P_2)^2 b_{t,2}P_2}$$
$$\Gamma_{21} = \frac{[-P_1 P_2(t_1-t_2)\Omega\ln\Omega+Et_T]b_{t,2}P_2}{t_T^2(P_1+P_2)^2 b_{t,1}P_1}, \quad \Gamma_{22} = \frac{P_1 P_2(t_1-t_2)\Omega\ln\Omega+Ft_T}{t_T^2(P_1+P_2)^2}$$

and Toth, respectively, may be represented by the following relation:

$$b = b_0 \exp\left[\frac{Q_{st}}{RT_0}\left(\frac{T_0}{T} - 1\right)\right] \tag{3.26}$$

where b_0 represents parameter b at temperature T_0 and Q_{st} the isosteric heat of adsorption [37]. In Nitta isotherm, n_{Nit} is temperature independent. However, in Langmuir-Freundlich and Toth isotherms, n_{LF} and t_i parameters depend upon temperature as follows:

$$\frac{1}{n_{LF}} = \frac{1}{n_{LF,0}} + \alpha_{LF}\left(1 - \frac{T_0}{T}\right) \tag{3.27}$$

$$t_i = t_0 + \alpha_t\left(1 - \frac{T_0}{T}\right) \tag{3.28}$$

where α_{LF} and α_t are constant parameters. In Toth multicomponent isotherm the hetero-

geneity factor is calculated from those of the pure components as:

$$t_{\mathrm{T}} = \sum_{j=1}^{N} y_{\mathrm{j}} t_{\mathrm{j}} \tag{3.29}$$

Finally the temperature dependency of the saturation capacity can be represented by the following empirical relation:

$$q_{\mathrm{sat}} = q_{\mathrm{sat},0} \, \exp\left[\chi \left(1 - \frac{T}{T_0} \right) \right] \tag{3.30}$$

being $q_{\mathrm{sat},0}$ the saturation capacity at temperature T_0 and χ a constant parameter [37].

Dubinin-Radushkevich. The Dubinin-Radushkevich isotherm is the most versatile and useful model for describing equilibrium adsorption of organic vapors on ordinary commercial activated carbons [38]. The single vapor equation for q moles adsorbed in equilibrium with its vapor at pressure P, can be expressed as:

$$q = \frac{W_0}{V_{\mathrm{m}}^0} \, \exp\left[- \left(\frac{RT}{\beta E_0} \right)^2 [\ln(P_{\mathrm{sat}}/P)]^2 \right] \tag{3.31}$$

being W_0 the micropore volume of the adsorbent and E_0 its reference adsorption energy, V_{m}^0 is the molar volume of the adsorbate, β is its affinity coefficient relative to the reference, and P_{sat} is the vapor pressure of the unadsorbed bulk at temperature T [39]. The inclusion of β allows the application of the parameters of micropore volume and reference adsorption energy measured with one vapor to predict the adsorption of other vapors. Benzene is usually the reference [38]. The Dubinin-Radushkevich isotherm can be seen as a particular case of the Dubinin-Astakhov isotherm, in which n = 2. Therefore, the seminal equation is:

$$q = \frac{W_0}{V_{\mathrm{m}}^0} \, \exp\left[- \left(\frac{RT}{\beta E_0} \right)^{\mathrm{n}} [\ln(P_{\mathrm{sat}}/P)]^{\mathrm{n}} \right] \tag{3.32}$$

The Dubinin-Astakhov isotherm for a binary mixture of components i and j in the fractional form may be expressed by [40]:

$$\theta_{\mathrm{i}} = \frac{\left[1 - \exp\left[- \left[\frac{RT \, \ln(P_{\mathrm{sat},j}/P_{\mathrm{j}})}{E_{\mathrm{j}}} \right]^{n_j} \right] \right] \exp\left[- \left[\frac{RT \, \ln(P_{\mathrm{sat},i}/P_{\mathrm{i}})}{E_{\mathrm{i}}} \right]^{n_i} \right]}{1 - \exp\left[- \left[\frac{RT \, \ln(P_{\mathrm{sat},i}/P_{\mathrm{i}})}{E_{\mathrm{i}}} \right]^{n_i} - \left[\frac{RT \, \ln(P_{\mathrm{sat},j}/P_{\mathrm{j}})}{E_{\mathrm{j}}} \right]^{n_j} \right]} \tag{3.33}$$

where $E_{\mathrm{i,j}} = \beta E_{0,\mathrm{i,j}}$. The Dubinin-Radushkevich is obtained substituting n_{i} and n_{j} by 2.

Chapter 4

Experimental Section

Gas permeation measurements of single gases and multicomponent mixtures are a fundamental tool for dynamic membrane characterization. The permeation of certain molecules may be used to evaluate membrane quality, detecting not only macro and/or meso-defects but also the transport mechanism(s) behind the whole process. The separation of multicomponent mixtures will evaluate for instance the real performance of the membrane.

In the present work the synthesis of AM-3 (Aveiro Manchester number 3) powder and membranes were studied. AM-3 membranes were prepared by seeded hydrothermal synthesis on porous α-alumina and the number of membrane depositions as well as the pH conditions were studied.

4.1 Membrane Installation

The experimental installation is composed of several elements connected to each other [9]. Figure 4.1 provides a global overview over the whole set-up.

Figure 4.1: Overall view of the experimental set-up.

The experimental apparatus consists essentially of the following components:

1. three mass flow controllers (MFC) (ALicat, MC-500SCCM-D/5M) controlling the feed

and sweep gas mass flow rates (figure 4.2 a);

2. a mass flow meter (MFM) (ALicat, M-500SCCM-D) measuring the permeate mass flow rate;

3. back pressure regulator (BPR) (ALicat, PC-100PSIG-D/5P) measuring and regulating the pressure at the retentate side, controlling in this way the transmembrane pressure difference (figure 4.2 a);

4. a pressure transducer (PT) (ALicat, P-100PSIG-D), placed before the MFM, measuring the permeate pressure (figure 4.2 a);

5. 16 electric solenoid valves (V1–V16) (Mega Control) opening and closing the gas lines of the experimental set-up; gases are fed to the system and flow through the set-up in 1/4" and 1/8" stainless-steel and polypropylene tubing (figure 4.2 a);

6. a gas detector (GD) (Oldham MX 2100) detecting any gas leakage; ventilation is also available for a quick evacuation of gases;

7. a tubular electric oven coupled with a PID controller (TC) (Eurotherm, Type 818) allowing the regulation of temperature and heating rate. A double thermocouple (Omega, Type K, CASS-IM15U-300-DUAL) is introduced inside the membrane and simultaneously connected to the temperature controller and to a data acquisition system (figure 4.2 b);

8. a stainless-steel membrane module which is used to accommodate the membrane during the permeation experiments (figure 4.2 c);

9. a gas chromatograph (GC) (DANI 1000 DPC), with a thermal conductivity detector (TCD), equipped with two separation capillary columns: a ValcoPLOT Molesieve 0.5×30 5A column for permanent gases, and a ValcoPLOT HayeSep D 0.5×30 column for CO2 separation (figure 4.2 d);

A graphical interface is available to exchange information between the user and the experimental set-up in an expeditious way. With this interface one may open or close specific solenoid valves in order to select the desired gas to be studied and control the feed flow. The retentate pressure can also be regulated from this interface. Feed and permeate flow rates, rententate and permeate pressures and temperature are recorded and saved into a spreadsheet file (figure 4.3). These parameters are also displayed in the computer and their evolution may be seen in a graphical form (figure 4.4).
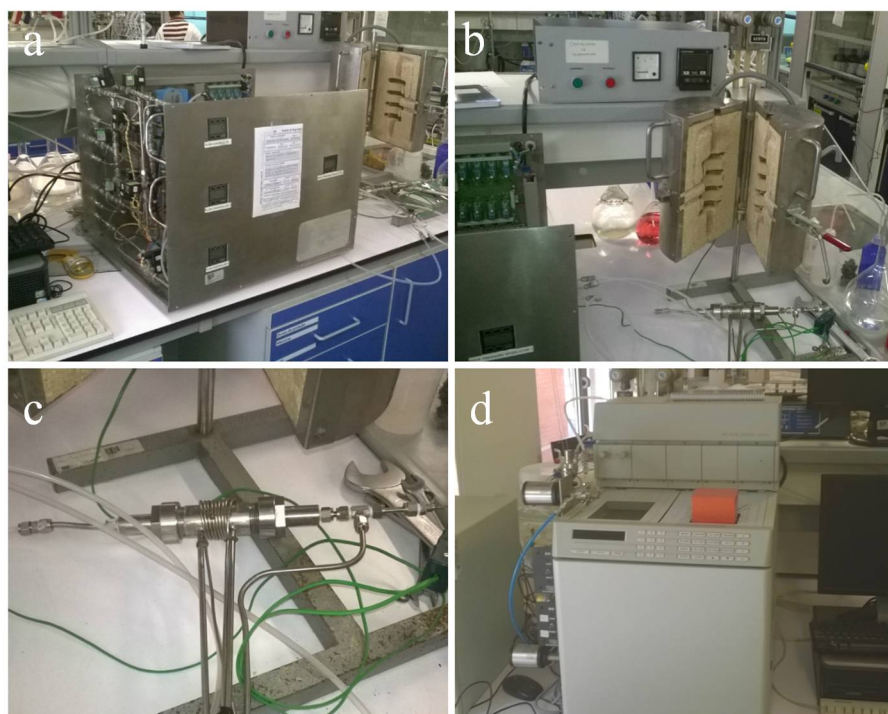
Figure 4.2: Main parts composing the membrane installation: a - unit containing all mass flow controllers and mass flow meters; b - stainless steel oven and temperature controller (at the top of the picture); c - stainless steel membrane module; d - gas chromatograph.
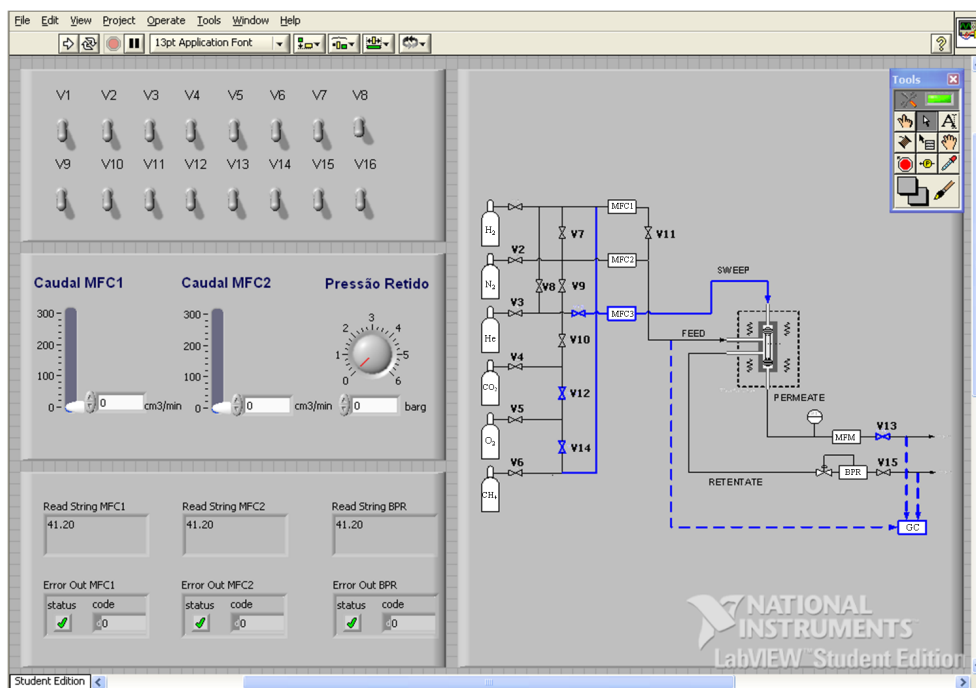
Figure 4.3: LabView interface allowing the adjustment of valves (according to the desired gas), the pressure drop across the membrane and the flow rate of the studied gas.
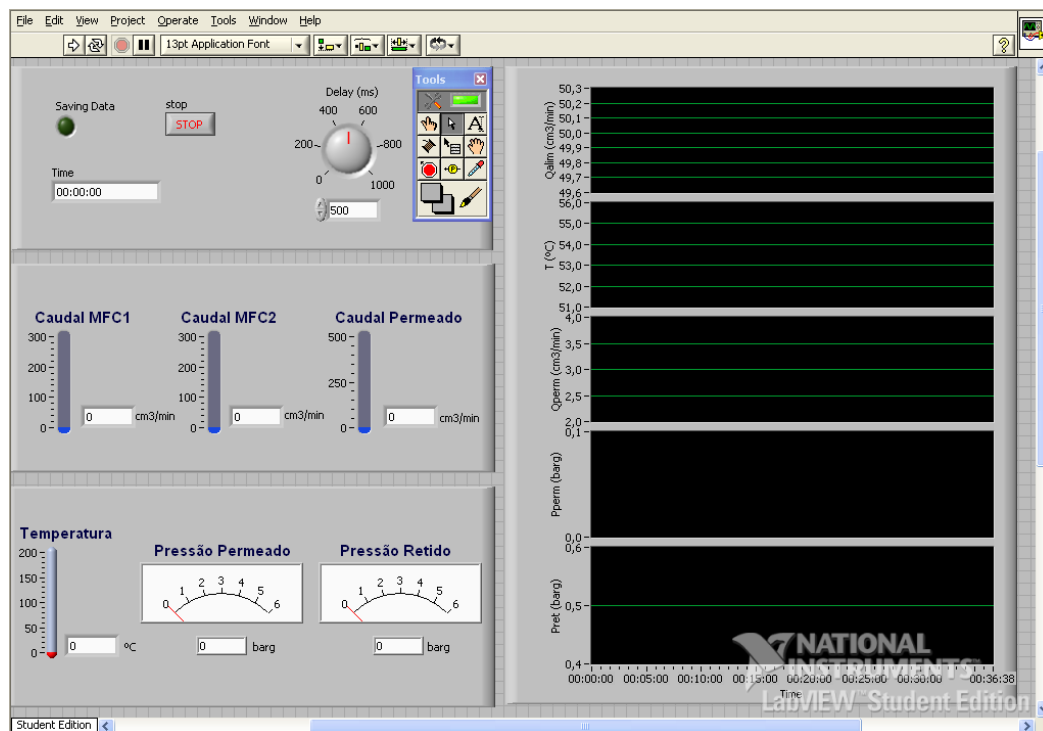
Figure 4.4: LabView interface for data acquisition. In the right side a graphical evolution (with time) of the temperature, permeate and feed flow rates and pressures is shown.

4.2 Membrane Synthesis

During this work several membranes were synthesized. AM-3 membranes were prepared on commercial tubular symmetric α-alumina supports. The supports were scratched with AM-3 seeds, and then subjected to a secondary growth step in Teflon-lined autoclaves at 230 ℃ under autogenous pressure. The molar compositions used to prepare AM-3 membranes were in the range of: $5.3 - 5.4$ Na_2O : 0.6 K_2O : $5.0 - 5.1$ SiO_2 : 1.0 TiO_2 : $113 - 274$ H_2O. The α-alumina supports have an average pore size of $900\,nm$ and a thickness of ca. $1.5\,mm$. The supports were placed vertically at the bottom of a Teflon-lined autoclave with a Teflon holder and the gel was poured into it. Sodium silicate solution ($27\,wt.\%$ SiO_2, $8\,wt.\%$ Na_2O, Sigma-Aldrich) and $TiCl_3$ (≥ 12 wt.% $TiCl_3$, 10 wt.% HCl, Sigma-Aldrich) were used as Si and Ti sources, respectively.

The resulting viscous gel was treated at 230 ℃ during 48 h. After that the autoclave was cooled down with fresh water and the samples washed with distilled water. In the case of multiple depositions, the washed samples were dried in the oven and then immersed into fresh gel and treated at the same temperature during the same period of time.

A typical synthesis of an AM-3 membrane consists of mixing $1.118\,g$ of KCl, $0.483\,g$ of NaCl, $2.877\,g$ of NaOH in $3.969\,g$ of H_2O. Sodium silicate solution (SSS) ($13.496\,g$) and $TiCl_3$ ($14.994\,g$) are added by this order, forming a final viscous gel which is stirred by hand until a uniform gel is obtained. According to the desired amount of gel and/or number of membranes

26

to synthesize, the quantity of reactants should change, but the relative proportions must be respected in order to obtain AM-3.

The structure and morphology of synthesized membranes were investigated using X-ray diffraction and scanning electron microscopy (SEM) (Hitachi, S-4100). While permeation measurements were performed using large porous supports, each sample for the previous characterization techniques was prepared on small porous supports (figure 4.5). The autoclaves as well were available in two different sizes according to the support dimensions (figure 4.6).
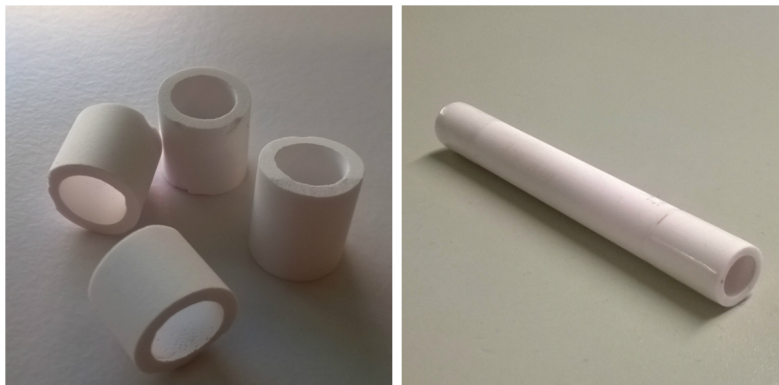
Figure 4.5: Small (left) and big (right) α-alumina porous supports.

Figure 4.6: Small (left) and big (right) autoclaves.

4.3 Gas Permeation Measurements

The permeation measurements were carried out placing the membrane inside the stainless steel module as depicted in figure 4.7. The membrane is sealed inside the module with two viton o-rings at each end in order to avoid any possible mixing between the permeate and the feed. The installation allows to carry out two alternative approaches for creating the driving force responsible for gas permeation: the pressure drop generation method and the Wicke-Kallenbach (WK) method. In the first one the driving force is imposed by generating a total pressure drop across the membrane. In the second one a sweep gas is used to sweep the permeate side (figure 4.7) in order to decrease the partial pressure of permeating species.

In this case the total pressure drop across the membrane may be zero, which eliminates the presence of viscous flow across membrane. Another advantage of employing this procedure is the fact that the turbulence generated by the flow of the sweep gas may contribute to eliminate the flow resistance to mass transfer. Nonetheless, one must remember that if a sweep gas is utilized, an additional downstream separation is needed in order to recover the target gas.
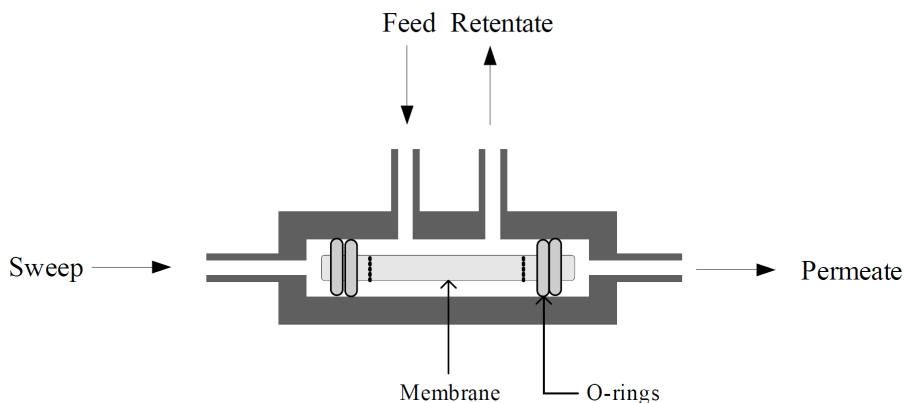
Figure 4.7: Schematic representation of the membrane module.

4.3.1 Membrane Pre-treatment

The presence of adsorbed compounds, particularly water, on the titanosilicate pores affects the permeation results. To remove these molecules, a heating and cooling cycle was always carried out in advance at temperatures up to 120 °C during one week. Membranes were not submitted to higher temperatures due to thermal limitations of the employed o-rings. During the heat treatment the continuous flow rate of He was 50 cm^3(PTN)/min facilitating the removal of desorbed species.

Chapter 5

Results and Discussion

This chapter presents all the modeling and experimental results obtained in this work. Regarding modeling, new expressions for Maxwell-Stefan thermodynamic factors were derived for the first time for the Dubinin-Astakhov and Dubinin-Radushkevich isotherms. These expressions were validated using permeation data of methane and ethane in a silicalite-1 membrane. Additionally, water permeation across zeolites 13X and 4A membranes was totally predicted by the Maxwell-Stefan equations and detailed in terms of adsorption and diffusion phenomena.

Concerning the experimental part, static and dynamic characterization of several AM-3 membranes is presented. The influence of the number of depositions as well as pH were investigated.

5.1 Modeling results

All the fitted parameters present in this section were obtained through unconstrained nonlinear optimization using the *fminsearch* function of MATLAB® employing the Nelder-Mead algorithm. The objetive function in all optimization procedures was the average absolute relative deviation ($AARD$, %)

$$AARD(\%) = \frac{100}{n} \sum_{i=1}^{n} \left| \frac{Var_{\text{calc}} - Var_{\text{exp}}}{Var_{\text{exp}}} \right| \tag{5.1}$$

where Var_{calc} and Var_{exp} are, respectively, the calculated and experimental variables, and n is the number of data points. The differential equations were solved using the *ode23* function of the same software, which is an implementation of an explicit Runge-Kutta (2,3) pair of Bogacki and Shampine.

5.1.1 Modeling permeances through silicalite-1 membrane

As reported previously in chapter 3, the selection of different isotherms gives rise to different thermodynamic factors of the MS main transport formulation. The simple and common

gaseous isotherms of Langmuir and Freundlich are accurate for some zeolites but they are often unsuitable for others. Dubinin-Astakhov (DA), and particularly Dubinin-Radushkevich (DR), are widely used to describe the adsorption behavior of organic vapors in activated carbons. Nonetheless their application to zeolite and zeolite-type materials is also reported in the literature [41, 42, 43]. Thus, the derivation of thermodynamic factors for both DA and DR isotherms becomes handy in the modeling field. The MS single component thermodynamic factor obtained for the DA (DR isotherm, n=2) isotherm is:

$$\Gamma = \frac{\ln(P_{\text{sat}}/P)}{nB[\ln(P_{\text{sat}}/P)]^{\text{n}}}, \; B = \left(\frac{RT}{E}\right)^{\text{n}} \tag{5.2}$$

The calculation of the thermodynamic factors requires differentiation of the isotherms explicitly in terms of fugacity or partial pressure (equation 3.18). Nonetheless, while Langmuir and Langmuir-Freundlich isotherms are easily inverted, the Dubinin-Astakhov and Dubinin-Radushkevich isotherms are not so straightforward. To overcome such limitation, the DA and DR isotherms in the fractional loading-form were differentiated with respect to the partial pressures and the functions obtained followed by calculus relations. Accordingly, taking into account that $\theta_i = \theta_i(p_i, p_j)$ and $\theta_j = \theta_j(p_i, p_j)$ the following system of differential equations is obtained:

$$\begin{cases} d\theta_1 = \left(\frac{\partial\theta_1}{\partial p_1}\frac{\partial p_1}{\partial\theta_1} + \frac{\partial\theta_1}{\partial p_2}\frac{\partial p_2}{\partial\theta_1}\right)d\theta_1 + \left(\frac{\partial\theta_1}{\partial p_1}\frac{\partial p_1}{\partial\theta_2} + \frac{\partial\theta_1}{\partial p_2}\frac{\partial p_2}{\partial\theta_2}\right)d\theta_2 \\ d\theta_2 = \left(\frac{\partial\theta_2}{\partial p_1}\frac{\partial p_1}{\partial\theta_1} + \frac{\partial\theta_2}{\partial p_2}\frac{\partial p_2}{\partial\theta_1}\right)d\theta_1 + \left(\frac{\partial\theta_2}{\partial p_1}\frac{\partial p_1}{\partial\theta_2} + \frac{\partial\theta_2}{\partial p_2}\frac{\partial p_2}{\partial\theta_2}\right)d\theta_2 \end{cases} \tag{5.3}$$

and solved using Cramer's rule to get the desired inverse partial derivatives:

$$\begin{aligned} \left(\frac{\partial p_1}{\partial\theta_2}\right)_{\theta_1} &= -\left(\frac{\partial\theta_1}{\partial p_2}\right)_{p_1}/D \\ \left(\frac{\partial p_2}{\partial\theta_2}\right)_{\theta_1} &= \left(\frac{\partial\theta_1}{\partial p_1}\right)_{p_2}/D \\ \left(\frac{\partial p_1}{\partial\theta_1}\right)_{\theta_2} &= \left(\frac{\partial\theta_2}{\partial p_2}\right)_{p_1}/D \\ \left(\frac{\partial p_2}{\partial\theta_1}\right)_{\theta_2} &= -\left(\frac{\partial\theta_2}{\partial p_1}\right)_{p_2}/D \end{aligned} \tag{5.4}$$

where

$$D \equiv \left(\frac{\partial\theta_1}{\partial p_1}\right)_{p_2}\left(\frac{\partial\theta_2}{\partial p_2}\right)_{p_1} - \left(\frac{\partial\theta_1}{\partial p_2}\right)_{p_1}\left(\frac{\partial\theta_2}{\partial p_1}\right)_{p_2} \tag{5.5}$$

The obtained thermodynamic factors for a binary mixture are listed in equations 5.6 to 5.9

$$\Gamma_{11} = \frac{[\exp(-A) - 1][\exp(-B) - 1]\ln(P_{\text{sat},1}/P_1)}{Bn_1[\exp(-B) + \exp(-A) - \exp(-B - A)) - 1]} \tag{5.6}$$

$$\Gamma_{12} = \frac{[\exp(-A) - 1]\exp(-B)[\exp(-A) - \exp(-B - A)]\ln(P_{\text{sat},1}/P_1)}{Bn_1\exp(-A)[\exp(-B) + \exp(-A) - \exp(-B - A)) - 1]} \tag{5.7}$$

$$\Gamma_{21} = \frac{\exp(-A)[\exp(-B) - 1][\exp(-B) - \exp(-B - A)]\ln(P_{\text{sat},2}/P_2)}{An_2\exp(-B)[\exp(-B) + \exp(-A) - \exp(-B - A)) - 1]} \quad (5.8)$$

$$\Gamma_{22} = \frac{[\exp(-A) - 1][\exp(-B) - 1]\ln(P_{\text{sat},2}/P_2)}{An_2[\exp(-B) + \exp(-A) - \exp(-B - A)) - 1]} \quad (5.9)$$

where $A = \left[\frac{RT \ln(P_{\text{sat},2}/P_2)}{E2}\right]^{n_2}$ and $B = \left[\frac{RT \ln(P_{\text{sat},1}/P_1)}{E1}\right]^{n_1}$. The thermodynamic factors for the DR isotherm are obtained from the previous equations by substituting n_1 and n_2 by 2.

In order to validate the derived expressions, each isotherm was fitted to the experimental data published by Zhu *et al.* [44] for both methane/silicalite-1 and ethane/silicalite-1, and then the thermodynamic factors were used with experimental data concerning the methane and ethane permeation through silicalite-1 membrane published by van de Graaf *et al.* [45]. Tables 5.1 and 5.2 present the single component adsorption data of methane and ethane in silicalite-1 at three different temperatures 303, 338 and 373 K.

Table 5.1: Single-component adsorption for methane at 303, 338 and 373 K (adapted from [9]).

303 K		338 K		373 K	
P (10^5 Pa)	q (mol kg^{-1})	P (10^5 Pa)	q (mol kg^{-1})	P (10^5 Pa)	q (mol kg^{-1})
0.104	0.045	0.097	0.026	0.306	0.037
0.142	0.065	0.127	0.035	0.415	0.050
0.172	0.078	0.171	0.041	0.495	0.060
0.200	0.088	0.206	0.047	0.564	0.067
0.254	0.116	0.262	0.058	0.665	0.080
0.294	0.136	0.310	0.072	0.737	0.089
0.393	0.180	0.405	0.093	0.820	0.098
0.477	0.214	0.490	0.108	0.902	0.105
0.547	0.243	0.552	0.121	1.011	0.117
0.641	0.280	0.655	0.145	1.102	0.129
0.707	0.304	0.720	0.156	1.504	0.171
0.789	0.335	0.800	0.174	1.998	0.221
0.829	0.354	0.883	0.187	2.498	0.266
0.876	0.371	0.986	0.207	2.997	0.309
0.918	0.386	1.104	0.230	3.503	0.349
0.980	0.406	1.501	0.297	4.003	0.388
1.095	0.445	1.999	0.380	4.502	0.424
1.490	0.569	2.498	0.452	5.002	0.457
2.000	0.685	2.998	0.517		
2.500	0.800	3.498	0.580		
2.999	0.898	4.003	0.634		
3.505	0.981	4.503	0.684		
4.017	1.056	5.003	0.731		
4.505	1.121				
5.004	1.175				

Table 5.2: Single-component adsorption for ethane at 303, 338 and 373 K (adapted from [9]).

303 K		338 K		373 K	
P (10^5 Pa)	q (mol kg^{-1})	P (10^5 Pa)	q (mol kg^{-1})	P (10^5 Pa)	q (mol kg^{-1})
0.033	0.220	0.051	0.147	0.023	0.038
0.054	0.405	0.079	0.208	0.054	0.064
0.086	0.548	0.102	0.255	0.085	0.088
0.106	0.666	0.122	0.296	0.101	0.111
0.134	0.768	0.149	0.346	0.120	0.129
0.154	0.839	0.188	0.422	0.143	0.146
0.193	0.953	0.227	0.480	0.193	0.187
0.233	1.041	0.305	0.597	0.224	0.219
0.318	1.172	0.371	0.688	0.313	0.280
0.388	1.254	0.444	0.758	0.387	0.332
0.450	1.318	0.549	0.848	0.452	0.379
0.558	1.385	0.618	0.906	0.552	0.443
0.631	1.429	0.726	0.962	0.626	0.484
0.724	1.469	0.826	1.023	0.726	0.536
0.827	1.507	0.965	1.083	0.830	0.582
0.973	1.553	1.108	1.159	0.972	0.646
1.109	1.592	1.502	1.275	1.101	0.707
1.508	1.652	2.003	1.366	1.501	0.836
2.004	1.696	2.511	1.430	2.002	0.958
2.506	1.720	3.006	1.478	2.498	1.046
3.007	1.740	3.508	1.515	3.000	1.117
3.509	1.753	4.009	1.548	3.501	1.174
4.010	1.766			4.009	1.225

Here the ratio W_0/V_m^0 and the product βE_0 (equation 3.32) were optimized as q_{sat} and E, respectively, for each component. Tables 5.3 and 5.4 lists the obtained parameters for both unary isotherms as well as the associated deviations ($AARD$). Since the experimental data reported by van de Graaf *et al.* [45] were obtained at 303 and 373 K the isotherms were adjusted simultaneously only for these two temperatures.

From the small AARD (1.39-7.93%) one may state that both equations are able to represent the adsorption equilibrium. Nevertheless both DA and DR models tend to describe more accurately the adsorption behavior of methane. Both E fitted parameters are analogous and increase with temperature being the only exception the ethane E parameter obtained for the DR isotherm. The saturation capacity (q_{sat}) decreases with temperature.

The heterogeneity parameter n of the DA equation characteristic of the adsorbent and is related with its structure; the more homogeneous the pores, the greater its value. However its exact value is a function of the adsorbate as well. Thus, finding a universal exponent for each material is very difficult [41]. Zeolite pores come in regular arrays and have a very uniform size distribution, typically lower than 10 Å. As stated in the literature the vast majority of n values for activated carbons are lower than 3, and for adsorption on zeolites values greater than 4

have been proposed. Therefore it can be stated that due to the homogeneity of zeolite and zeolite-type materials in comparison with activated carbons values of 3-4 may be expected.

In the present work a value closer to 3 (2.869) was obtained for ethane and a value of 2.082 obtained for methane. Abdul-Rehman *et al.* [46], Buss and Heuckel [47] and Lito *et al.* [37] obtained heterogeneity parameters for Langmuir-Freundlich and Toth isotherms closer to unity, attributing that fact to the high surface homogeneity as well as the channel like pore geometry of silicalite-1. Thus in the present work, the results obtained may reflect the dependency of the n parameter on the type of adsorbate.

In this way, particularly in zeolite systems, the homogeneity factor (n) should be an adjustable and experimentally derived parameter instead of being considered a value of 2 or nearby, the most common value for activated carbons. Therefore the most general DA adsorption isotherm should be used. Figure 5.1 shows graphically the DA and DR isotherms fitted to the experimental points.

Table 5.3: Single component parameters of Dubinin-Astakhov isotherm for methane/silicalite-1 and ethane/silicalite-1 unary systems.

	Dubinin-Astakhov			
	q_{sat} (mol kg^{-1})	E (kJ mol^{-1})	n	*AARD* (%)
Methane 303 K	5.071	10.540	2.082	1.390
Methane 373 K	4.603	13.480		
Ethane 303 K	2.131	14.530	2.869	6.830
Ethane 373 K	1.701	16.040		

Table 5.4: Single component parameters of Dubinin-Radushkevich isotherm for methane/silicalite-1 and ethane/silicalite-1 unary systems.

	Dubinin-Radushkevich		
	q_{sat} (mol kg^{-1})	E (kJ mol^{-1})	*AARD* (%)
Methane 303 K	5.679	10.120	1.646
Methane 373 K	5.258	12.900	
Ethane 303 K	2.696	12.950	7.933
Ethane 373 K	3.089	12.540	

The prediction of the separation of binary mixtures on silicalite-1 was possible by first studying the individual gas permeances using the experimental data reported by van de Graaf *et al.* ([45]), consisting of pure gas fluxes for several transmembrane pressure drops at temperatures of 303 and 373 K.

For each isotherm and thus for each thermodynamic factor, the parameters $Ð_{\text{s}}^0$ and $E_{\text{a,s}}$ of equation 3.13 were optimized simultaneously for the two temperatures. The determination of these two parameters was carried out solving simultaneously the MS equations for both
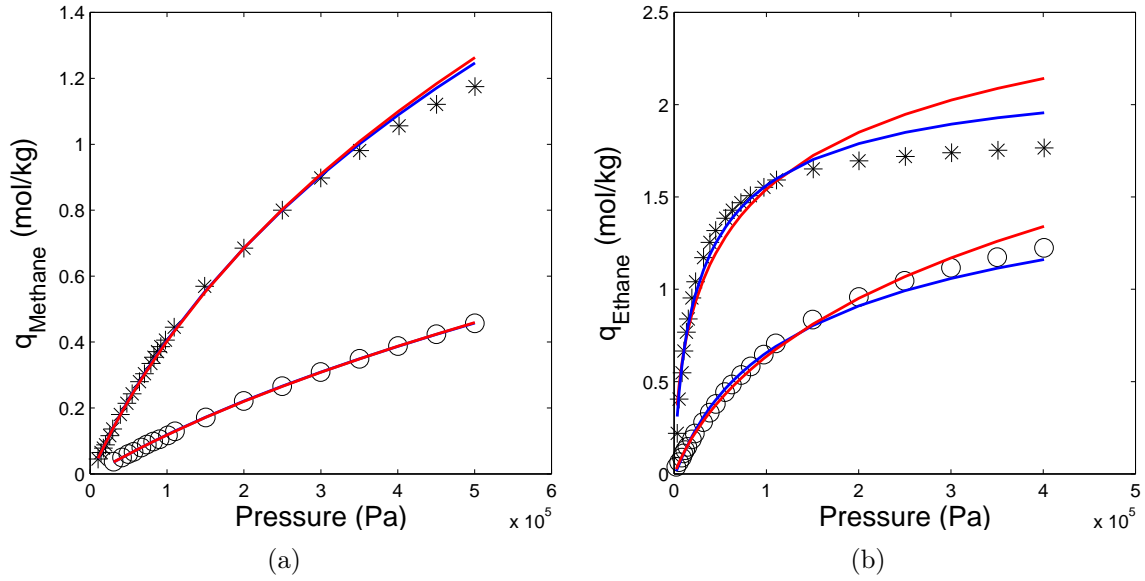
Figure 5.1: Single component isotherms for methane/silicalite-1 (a) and ethane/silicalite-1 (b); ∗ - 303 K, ∘ - 373 K, − - Dubinin-Astakhov equation, − - Dubinin-Radushkevich equation.

support and zeolite layers, calculating their profiles of θ and pressure. At each interface of the membrane layer the isotherms equations were used to calculate the compositions in the zeolite/support and feed/zeolite interfaces. The isotherm parameters for Langmuir, Nitta, Langmuir-Freundlich and Toth equations of methane/silicalite-1 and ethane/silicalite-1 were collected from the literature [37]. The main features of the membrane are in table 5.5.

Table 5.5: Physical features of the membrane used by van de Graaf *et al.* [45].

Surface membrane area, m^2	2.00×10^{-4}
Zeolite layer thickness, m	1.0×10^{-5}
Zeolite density, g m^{-3}	1.8×10^{6}
Support thickness, m	3.0×10^{-3}
Support porosity	0.2

A detailed description of the entire calculation can be found in the appendix A. The obtained results for each isotherm are plotted in figure 5.2 and the obtained parameters are presented in table 5.6.

The analyzed isotherms, particularly the DA and DR, are able to describe the permeation of both methane and ethane at 303 and 373 K over all range of experimental pressures, i.e. up to ca. 5 bar. At high pressures the fitted isotherms for methane tend to underestimate their fluxes while for ethane almost all isotherms overlap their results. The flux of methane shows approximately a linear behavior with pressure while the ethane fluxes tend to a plateau at 303 K, which may be attributed to its stronger adsorption strength in the zeolite. Moreover, the increase of temperature decreases methane fluxes, these being inclusively inferior to ethane fluxes. The decrease of methane flux may be a consequence of the decrease of adsorbed

Table 5.6: Single-component diffusion parameters fitted to the experimental data of van de Graaf *et al.* [45] for methane (1) and ethane (2).

	$Ð_{s,1}^0$ (m^2/s)	$E_{a,s,1}$ (kJ/mol)	$Ð_{s,2}^0$ (m^2/s)	$E_{a,s,2}$ (kJ/mol)
Langmuir	1.995×10^{-8}	7.225	1.236×10^{-7}	16.810
Nitta	1.082×10^{-8}	7.098	1.220×10^{-7}	16.780
Langmuir-Freundlich	2.141×10^{-8}	7.331	1.225×10^{-7}	16.800
Toth	1.914×10^{-8}	7.086	1.236×10^{-7}	16.820
Dubinin-Astakhov	2.757×10^{-8}	7.911	1.687×10^{-7}	18.850
Dubinin-Radushkevich	2.370×10^{-8}	7.527	1.377×10^{-7}	17.320

(a) (b)
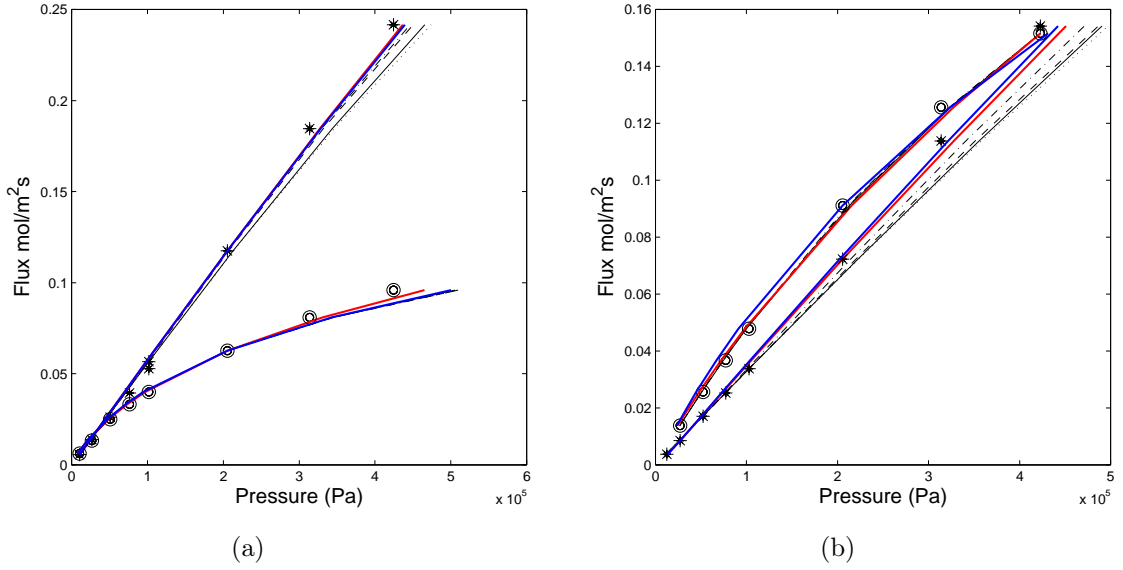
Figure 5.2: Permeation fluxes of methane and ethane as a function of gas pressure in the feed: modeling (this work) and experimental data by van de Graaf *et al.* [45] (a) 303 K (b) 373 K; ∗ - methane, ∘ - ethane, — - Dubinin-Astakhov equation, — - Dubinin-Radushkevich equation, full lines - Langmuir, dotted lines - Nitta, dashed-dotted lines - Langmuir-Freundlich, dased dashed lines - Toth isotherm.

molecules while for ethane the diffusivity overcomes the desorption phenomena for these temperatures.

With the single component diffusion parameters fitted to the experimental data, the separation of a binary mixture of ethane and methane was totally predicted at 303 K by just using the multicomponent isotherms and the Vignes relation (equation 3.21) for the calculation of the MS surface pair diffusivities $Ð_{ij}^s$ from the single ones on the solid, $Ð_i^s$. The experiments performed by van de Graaf [45] were conducted using the Wicke-Kallenbach technique, i.e. using a constant flow rate of helium to sweep the permeate side. Both sides of the membrane were considered well mixed and the counter-flux of helium was neglected in the calculations. The numerical solution was accomplished solving simultaneously the generalized MS equations for both support and zeolite layers. A detailed description of the full calculation procedure

can be found in the appendix A. The obtained results are displayed in figure 5.3.
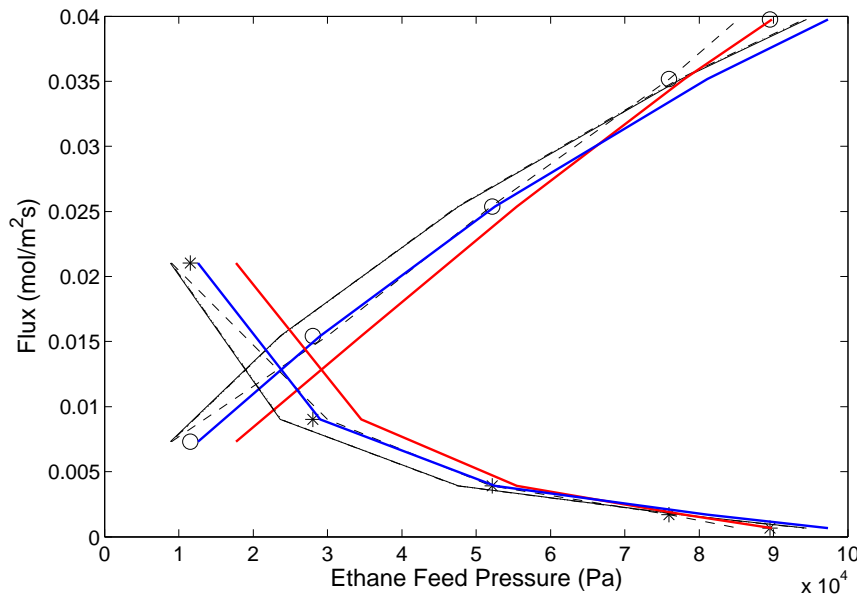
Figure 5.3: Permeation fluxes of $*$ - methane and $\circ$ - ethane as a function of ethane partial pressure at 303 K: modeling (this work) and experimental data (van de Graaf *et al.* [45]). Lines: full lines - Langmuir, dotted lines - Nitta, dashed-dotted lines - Langmuir-Freundlich, dashed dashed lines - Toth isotherm, $-$ - Dubinin-Astakhov equation, $-$ - Dubinin-Radushkevich equation.

The obtained results clearly highlight the predictive capability of the MS model combined with the thermodynamic factors published in the literature and those derived in this work. While Langmuir, Nitta and Langmuir-Freundlich tend to underestimate methane flux and overestimate ethane flux at lower pressures, the opposite happens with the DR isotherm. The Toth and DA isotherms represent both fluxes accurately. Nonetheless, the DA isotherm tends to underestimate ethane's flux at higher ethane feed pressures. These results are in agreement with figure 5.4 in which the binary adsorption of methane and ethane was totally predicted using pure component data. It can be seen that for methane, the DR isotherm gives higher adsorption values in comparison with the remaining ones, being the opposite verified for ethane, explaining the differences in the fluxes for both species and for the considered isotherms. The same occurs with the DA isotherm in which the adsorption of both species lies always between the Langmuir/Langmuir-Freundlich and the DR isotherms being the same fact verified in figure 5.3 for the fluxes. Additionally, Langmuir and Langmuir-Freundlich describe similarly the equilibrium of ethane and methane, and thus, the flux of both species. Therefore, the selection of different models should be regarded carefully.

The flux of methane decreases with pressure while methane flux behaves oppositely. This is a characteristic of this system since one of the gases adsorbs much strongly than the other, and thus it permeates preferentially through the zeolitic pores, hindering the diffusion of the second gas.
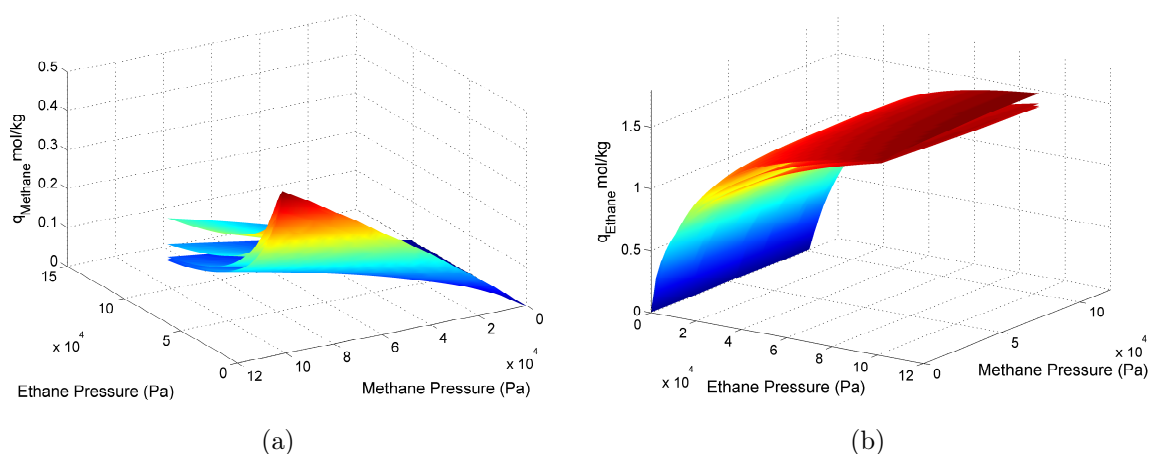
Figure 5.4: Prediction of binary adsorption of (a) methane and (b) ethane using different isotherm models. Isotherms: (a) Dubinin-Radushkevich, Dubinin-Astakhov, Toth, Langmuir-Freundlich and Langmuir from the top to the bottom, respectively, and (b) Dubinin-Radushkevich, Dubinin-Astakhov, Toth, Langmuir-Freundlich and Langmuir from the bottom to the top, respectively.

5.1.1.1 Influence of surface loading upon diffusivities

In spite of being generally constant, the Maxwell-Stefan diffusivities in zeolites show a variety of dependencies on molecular loading or occupancies in zeolites. Such influence is caused by a variety of factors, including zeolite topology, connectivity and molecular interactions, that affect in different ways the energy barrier for diffusion [34]. Molecular dynamic simulations performed for a variety of zeolites with different topologies by Skoulidas and Sholl have disclosed several scenarios other than the previous two present in chapter 3 as shown in figure 5.5 [48, 49]. While CF_4 tends to follow the strong confinement scenario, none of the other molecules considered follow the weak confinement scenario. Some of them present also a little maximum (Xe). Lito *et al.* [27] performed a similar modeling of methane/silicalite-1 and ethane/silicalite-1 assuming a weak confinement scenario as was presented in the previous section (figures 5.2 and 5.3), i.e. assuming that the MS diffusivities are loading-independent. Here it will be proven that this is a fairly good approximation since it has never been demonstrated before. Contrarily of what was done previously with the modeling of methane/silicalite-1 and ethane/silicalite-1, for each experimental point published by van de Graaf *et al.* [45] the MS diffusivities were determined for both temperatures (303 and 373 K), and the obtained diffusivities were plotted against the fractional occupancy on the feed side. Since our aim is to observe the behavior of the MS diffusivities with the surface loading, the Langmuir isotherm, a simple adsorption model, was used to calculate the θ at the feed side and the thermodynamic factor for solving the MS equations. The results obtained are shown in figure 5.6.

As one may see the diffusivities of both permeating species are almost independent of the fractional occupancy, particularly those of ethane (for methane, the diffusivities at 373 K
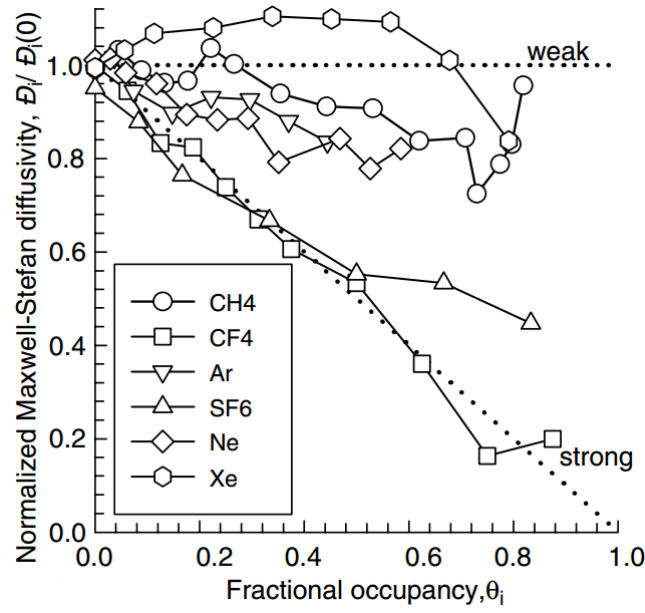
Figure 5.5: Occupancy dependences for diffusion of CH_4, CF_4, Ar, SF_6, Ne and Xe in MFI at 298 K (adapted from [34]). Dotted lines identify weak and strong confinement.
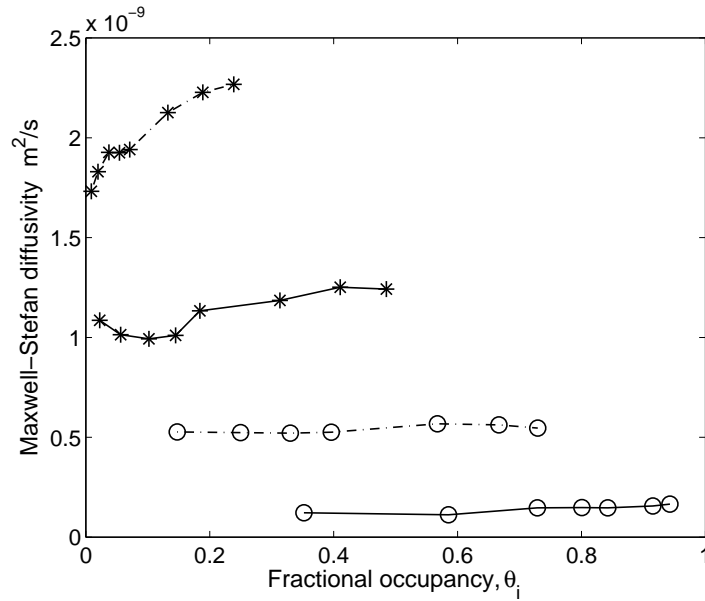
Figure 5.6: Occupancy dependences of MS diffusivities of methane and ethane in silicalite-1 at 303 (full lines) and 373 K (dashed-dotted lines) (calculated in this work). $\ast$ - methane, $\circ$ - ethane.

increase ca. 34 % with θ). This is in agreement with the results shown in figure 5.2 in which the zero loading dependence was adopted ($Đ_i = Đ_i^s(0) =$ constant) and produced generally good representations. At higher pressures the adsorption models underestimate methane fluxes while for ethane, throughout the pressure range considered, they are quite accurate, and as already stated, all isotherms are almost overlapped. Hence, these modeling differences

should be attributed to the accuracy of the equilibrium isotherms.

For solving practical problems it is therefore necessary to possess knowledge on how the MS single-component diffusivities change with the surface loading. In the present work, the zero loading dependence was a reasonably good assumption, though a linear relationship for methane at 373 K could be introduced.

5.1.2 Modeling water permeance through 13X and 4A zeolite membranes

Growing concerns of indoor air quality and increasing energy demand have driven the development of new energy-efficient cooling processes. Currently the most common cooling technology is the vapor compression refrigeration (VCR), widely used for space cooling, ice making, food storage, among other applications [50, 51]. However its performance depends strongly on ambient conditions. In warm and humid climates, VCR requires a high energy cost per unit of sensible heat removed due to the water condensation from air. Thus, a system capable of water removal preceding the VCR stage is highly desirable [52].

Several desiccant materials have been reported in the literature, but their necessity for constant adsorption/regeneration cycles is a great drawback [53, 54]. In this context, membrane dehumidification for air conditioning has received great attention [55]. Firstly used by NASA researchers for space traveling [56], the use of a membrane for air drying consists essentially on a semi-permeable barrier utilized selectively to remove water from a humid air stream. During the dehumidification process there is no need for a heat source, and therefore the dried air remains at the same initial temperature, no regeneration is involved and no emissions are released to the environment. Thus, membrane dehumidification is an environmentally friendly process. The main downside of membrane air-drying is the need for a driving force for water permeation across the membrane, which is generally accomplished by reducing the water partial pressure at the permeate side of the membrane [57].

Zeolites, namely those of faujasite framework type (X and Y zeolites) and those of type A are well suited for the separation of polar/non-polar molecules due to their high hydrophilicity, non-linear isotherms, and high water adsorption capacity [58].

In this dissertation, with the knowledge on how the effective diffusivities vary with temperature and solid loading for zeolites 13X and 4A, the Maxwell-Stefan equations for a single component (in this case, water) were solved and the water flux through a theoretically designed membrane was computed.

Using TableCurve 3D® software, a surface was fitted to the data presented in the literature, and an equation for the water diffusivity as function of solid loading and temperature through both zeolites was found (see appendix B for the diffusivities data used here). Equations 5.10, and 5.11, and figures 5.7 and 5.8, represent the diffusivity of water on zeolites 13X

and 4A, respectively:

$$D_{\text{eff, 13X}} = \exp\Bigg[-27.889 + 4.420 \times 10^{-4} T^{1.5} - 284.341 q^2 - \frac{107.152 q}{\ln q} + 3.839 q^{0.5}$$
$$- \frac{4.042 \times 10^{-3}}{q^{1.5}} \Bigg] \tag{5.10}$$

$$D_{\text{eff, 4A}} = -7.915 \times 10^{-9} + 2.026 \times 10^{-9} \ln T - 9.907 \times 10^{-10} \ln q - 1.197 \times 10^{-10} (\ln T)^2$$
$$- 7.707 \times 10^{-11} (\ln q)^2 + 1.209 \times 10^{-10} \ln T \ln q \tag{5.11}$$

where T and q represent the temperature and solid loading, respectively.
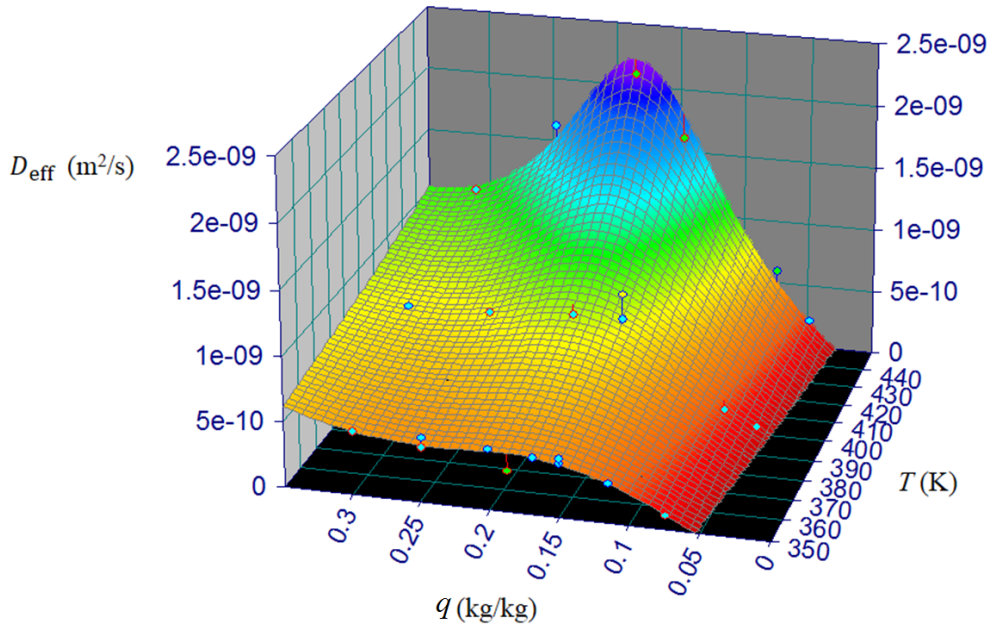
Figure 5.7: Effective diffusion coefficient of water on zeolite 13X as a function of temperature and surface loading. The surface was fitted to experimental data of Demontis *et al.* [59], being given by equation 5.10. $R^2 = 0.968$.

Equation 3.19 may be integrated between $z = 0$, $\theta = \theta_{\text{feed}}$ and $z = \delta$, $\theta = \theta_{\text{perm}}$, and the following relation for determining the water flux arises:

$$N_{\text{water}}^{\text{s}} = -\frac{\rho_{\text{p}} q_{\text{sat}}}{\delta} \int_{\theta_{\text{feed}}}^{\theta_{\text{perm}}} \Gamma(\theta) Ð_{\text{i}}(\theta) \, d\theta \tag{5.12}$$

where δ is the zeolite layer thickness of the membrane, and the subscripts feed and perm stand for feed and permeate sides, respectively. The integral was numerically evaluated in Matlab® using the composite Simpson's rule with 40 equally spaced points. The simple Langmuir isotherm was adopted since our aim is not to extract a numerical value but to examine the behavior of water flux for both zeolites. For the same reason the resistance of the support was
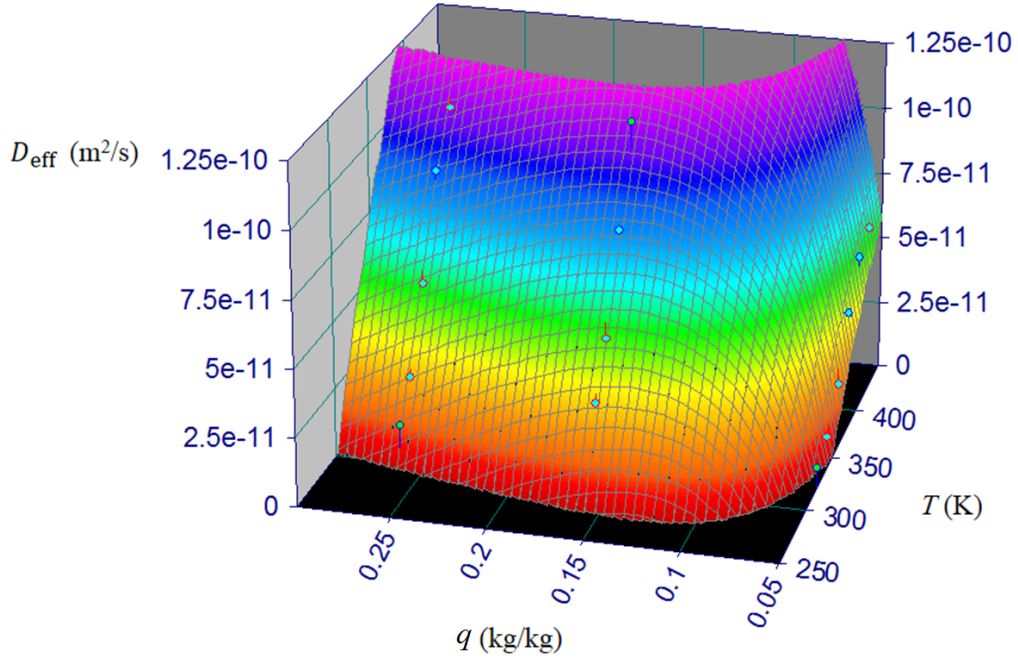
Figure 5.8: Effective diffusion coefficient of water on zeolite 4A as a function of temperature and surface loading. The surface was fitted to experimental data of Paoli *et al.* [60], being given by equation 5.11. $R^2 = 0.977$.

not considered. A value of 50 µm was chosen for the membrane thickness, a value reported in the literature for which defect-free 4A zeolite membranes with high selectivities are obtained [61].

Langmuir isotherm was then adjusted to the adsorption data present in the literature for both zeolite 13X and 4A and the obtained parameters are shown in table 5.7 (see appendix B for the adsorption data used here). In figure 5.9 the obtained results are displayed graphically. It should be noticed that the Langmuir isotherm tends to underestimate the saturation capacity, particularly for the case of zeolite 4A at 290 K.

Table 5.7: Parameters of the Langmuir isotherms of water in zeolites 13X and 4A. The reference temperatures are 294 and 290 K, respectively.

	b_0 (Pa^{-1})	Qst (J mol^{-1})	$q_{sat,0}$ (kg kg^{-1})	χ	AARD %
Zeolite 13X	3.420×10^{-2}	4.85×10^4	2.92×10^{-1}	1.880	12.4
Zeolite 4A	4.666×10^{-1}	6.39×10^4	1.97×10^{-1}	0.137	11.7

With the isotherm parameters known, the surface coverage on both sides of the membrane was evaluated and the water flux calculated by equation 5.12. Two different scenarios were considered: (i) the pressure drop across the membrane was kept constant and the feed pressure was increased, and (ii) the permeate pressure was kept constant and the feed pressure was
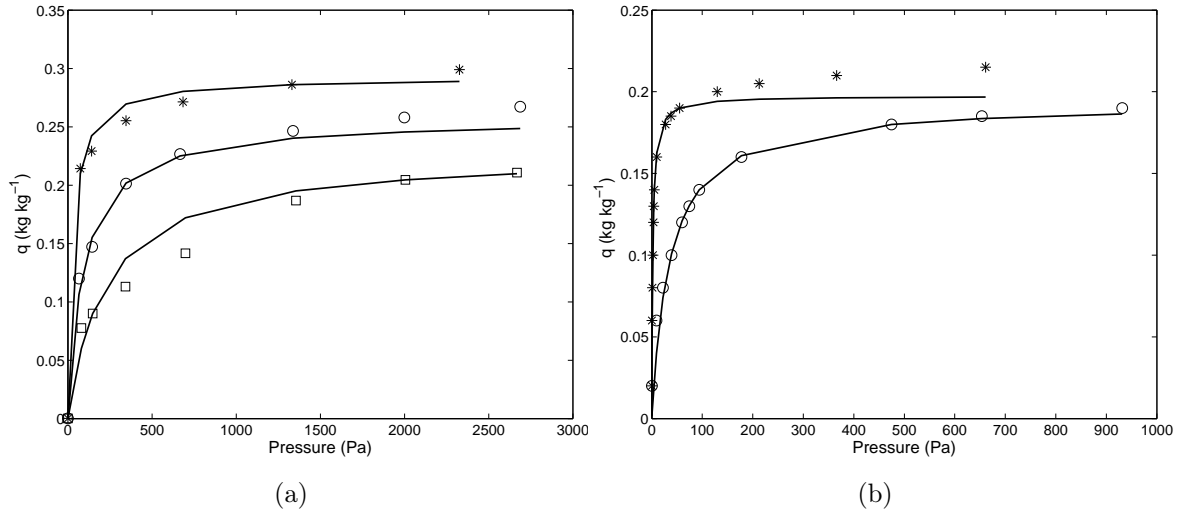
Figure 5.9: Adjusted Langmuir isotherm to the adsorption data for (a) zeolite 13X ($*$ 294 K, $\circ$ 314 K, $\square$ 333 K) and (b) zeolite 4A ($*$ 290 K, $\circ$ 330 K).

increased, i.e. the water flux was computed for different transmembrane pressure drops. A comparison between the results for both zeolites is provided in the following.

5.1.2.1   Constant transmembrane pressure drop

Keeping the pressure drop across the membrane constant and increasing feed pressure leads to a decrease in the water flux as illustrated in figures 5.10 and 5.11. This observation can be easily explained regarding the shape of the isotherms as depicted in figure 5.12. Due to the non-linearity of the isotherm, increasing the feed pressure and keeping the pressure drop constant leads to a successive decrease in the "surface loading drop", the difference between the surface loading on the feed and the permeate sides, decreasing the true driving force behind the permeation mechanism in th membrane. Additionally increasing the pressure drop, the difference between the surface coverage on both sides increases and the flux of water increases.

The water flux decreases as the temperature increases for the zeolite 13X and for the zeolite 4A the opposite occurs. Taking into consideration the diffusivities of zeolite 4A, one may state that, for the given range of temperatures, they present significant variations in comparison with those of zeolite 13X, which only presents the "peak" as a major variation with respect to temperature. The fact that the diffusivities increase much more with temperature throughout the whole range of loading for zeolite 4A may explain this behavior. A decrease in the loading of the solid as a result of an increase in temperature may be compensated by an increase in the diffusivity, increasing the water flux. For the zeolite 13X, especially at lower temperatures for which the diffusivities do not change significantly (see figure 5.7), and therefore, the loading effect is not offsetted, the water flux decreases. For the zeolite 13X another effect appears at higher temperatures. For low pressures an increase in the feed pressure increases the flux until a maximum value and after that the flux decreases with the increase of feed pressure.

42

(a)   (b)
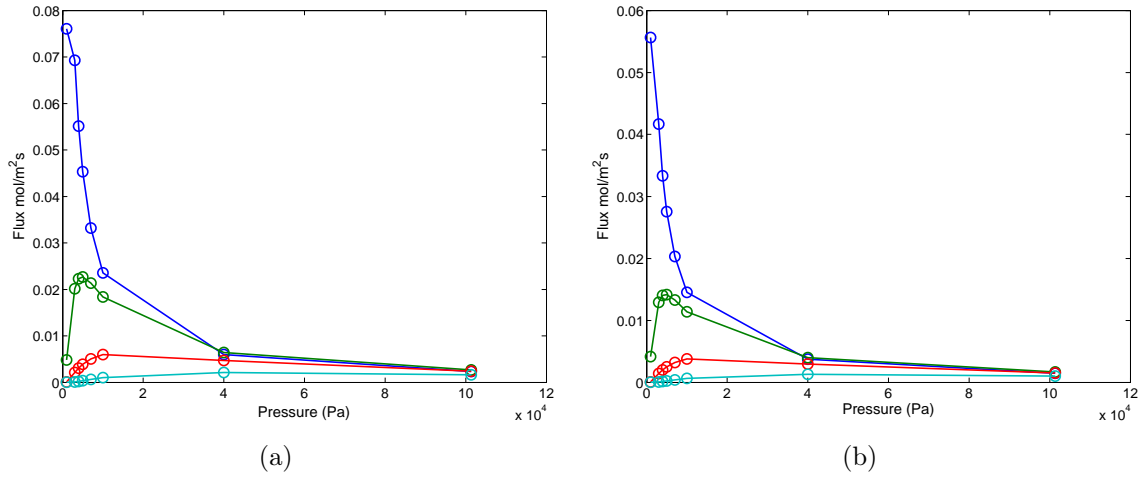
Figure 5.10: Water flux through zeolite 13X for a pressure drop of 800 Pa (a) and 500 Pa (b). Low to high temperatures from the top to the bottom of the figure: 350, 380, 410 and 440 K, respectively.

(a)   (b)
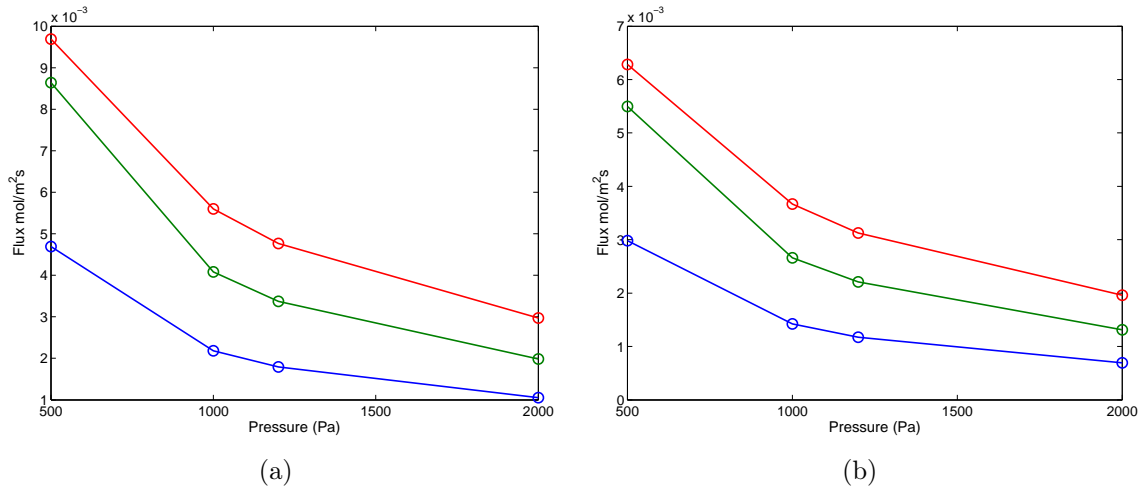
Figure 5.11: Water flux through zeolite 4A for a pressure drop of 120 Pa (a) and 80 Pa (b). Low to high temperatures from the bottom to the top of the figure: 300, 320 and 350 K, respectively.

This behavior may be ascribed to two competing effects: adsorption and diffusion. At lower pressures an increase in the feed pressure decreases the "true driving force" (see figure 5.12), but at the same time the effective diffusivity increases, being this last effect predominant at lower pressures. At higher pressures the increment of pressure decreases both parameters, and thus, the flux decreases. At lower temperatures this maximum is not observed since the diffusion remains practically constant and here the effect of the reduction of the "surface loading drop" is dominant. For the zeolite 4A this effect is not observed and the flux decreases always with the increase of pressure.

43
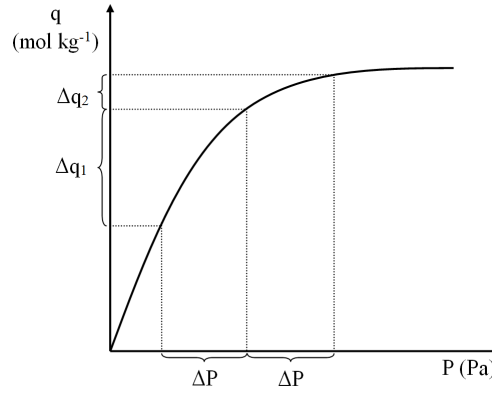
Figure 5.12: Illustrative behavior of an isotherm showing a decrease in the loading for the same pressure drop.

5.1.2.2 Constant permeate pressure and variable transmembrane pressure drop

Here the permeate pressure was held constant and the feed pressure was increased. The same behavior with the temperature is visible and the explanation is the same. The flux increases as the pressure increases due to the increment of the pressure drop and thus the increase in the "true driving force". This increase, however, tends to decrease with the increase of the pressure since the saturation is reached and the pressure drop approaches a "constant value". The results are presented in figure 5.13.
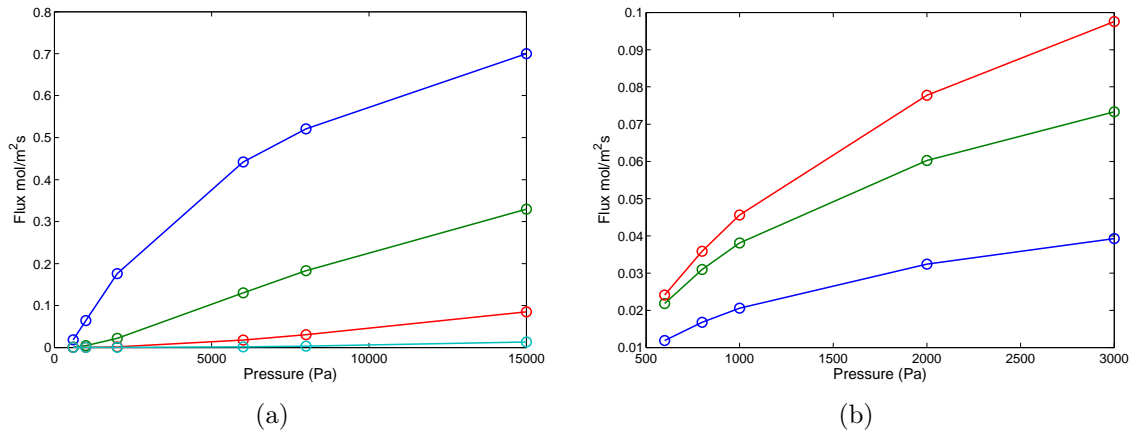
Figure 5.13: Water fluxes as function of feed pressure. (a) zeolite 13X: Low to high temperatures from the top to the bottom of the figure: 350, 380, 410 and 440 K, respectively; (b) - zeolite 4A: Low to high temperatures from the bottom to the top of the figure: 300, 320 and 350 K, respectively).

5.1.2.3 Comparison between both zeolites

In figure 5.14 a comparison between both zeolites is presented for 350 K. Water flux shows higher values for zeolite 13X due primarily to its higher diffusivity rather than solid loading,

since for this temperature the loading difference for both zeolites is negligible (0.2044 kg kg^{-1} against 0.1919 kg kg^{-1} for zeolite 4A). The different diffusivities between the microporous materials may be explained in terms of their pore diameter, in which zeolite 13X presents a pore size of 10 Å against 4 Å for zeolite 4A [62]. The smaller the pore, the higher the interactions between the molecules and solid surface, leading to a reduction in their mobility, and thus a smaller diffusivity is observed.
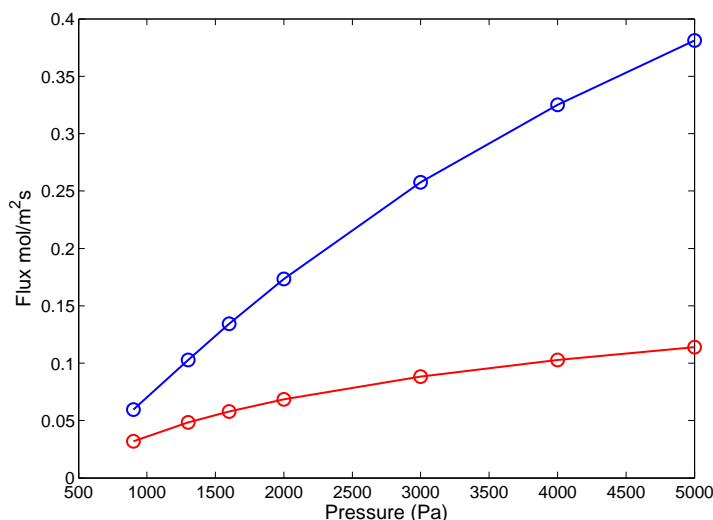
Figure 5.14: Comparison between both zeolites 13X (top line) and 4A (bottom line) at 350 K.

5.2   Membrane Characterization

The techniques used in this work to characterize the membrane were scanning electron microscopy (SEM) and X-ray diffraction (XRD). The results show that after three synthesis/depositions, the AM-3 becomes evident.

5.2.1   Static Characterization

5.2.1.1   Number of depositions

The number of depositions is an important parameter to control the membrane quality. One deposition may be successful in the sense of obtaining a pure phase of material, but the final result may be poor concerning the separation of mixtures, due largely to the presence of macro, meso or even micro-defects. Thus, more than one deposition (synthesis) of material is usually required, increasing the selectivity of the membrane. However it should be taken into account that the increase of zeolite film thickness as a result of the number of depositions may lead to a substantial decrease in the production of the desired product. Therefore the number of depositions is a parameter that should be regarded carefully.

In figure 5.15 the effect of the increase of the number of depositions (from left to right) is explored. One may see that the AM-3 becomes increasingly visible and easily identifiable, particularly in the exterior side of the support.

The supports were previously seeded, scratching their surface with AM-3 crystals with the help of a brush in both interior and exterior sides. The seeds have the function of providing new nucleation sites from which the AM-3 crystals may grow. Thus the amount of seeds present in the first crystallization may not be sufficiently enough to allow an appropriate growth of the crystals. Therefore after one deposition the new synthesized crystals may act like new nucleation points and the desired phase becomes more and more evident after depositions.
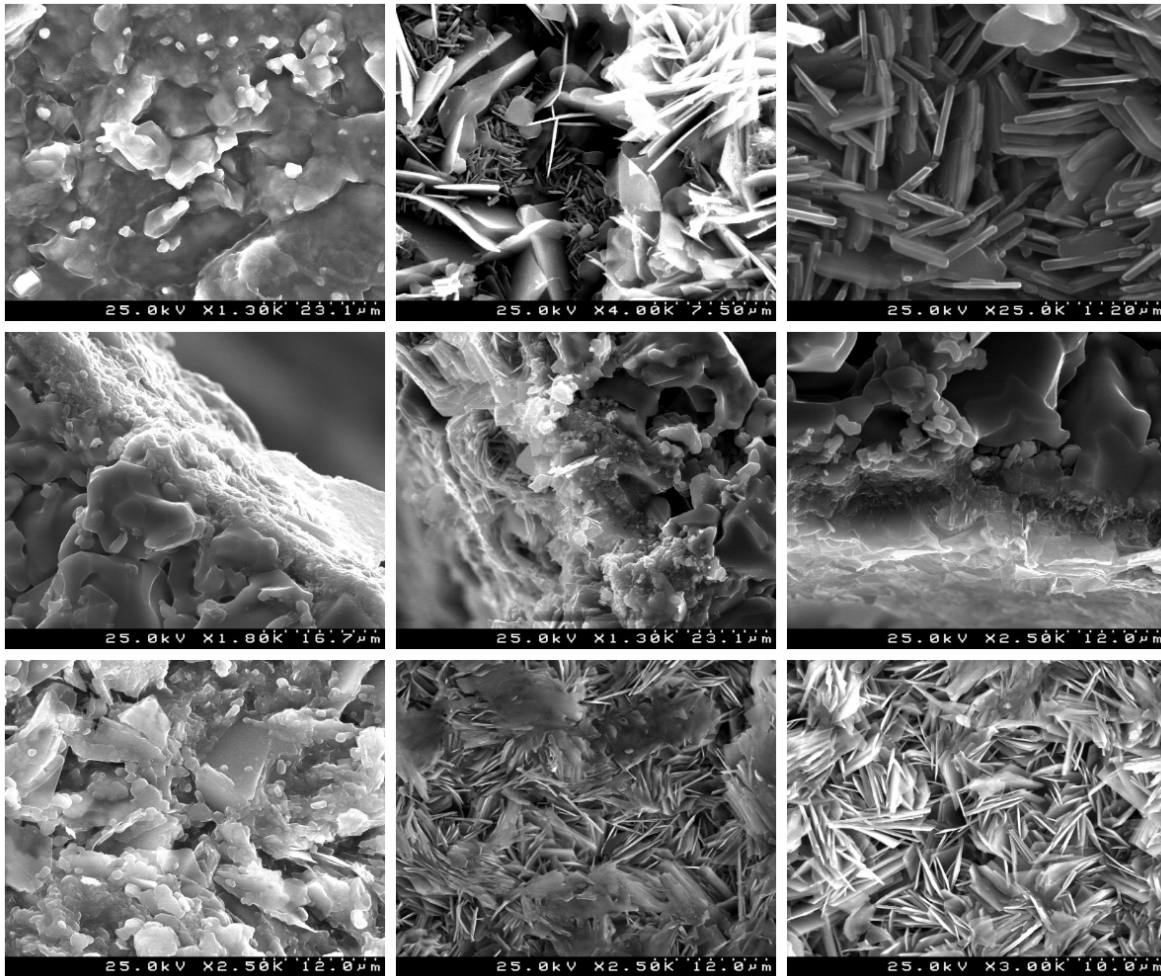
Figure 5.15: Effect of the number of depositions (AM-3 synthesis). Interior, lateral and exterior view from top to bottom, respectively. First, second and third depositions from left to right, respectively.

Another technique reported in the literature [63] to seed the supports consists of immersing them in water and the desired seeds material. Through an ultrasound bath the suspension is kept agitated. With this technique the seeds penetrate the support pores and a quick drying at 110 ℃ creates the necessary forces to keep the seeds adhered on the support during

the hydrothermal synthesis. However this technique was already applied without further advantages over the scratching technique used in this work.

The results obtained by SEM are in agreement with those obtained with XRD. In figures 5.16 and 5.17 the XRD patterns for both exterior and interior sides of the membrane are presented. In both figures one may see that the intensity of the peaks associated to AM-3 increase with the number of depositions (dashed lines). Nevertheless, with the increase of the number of depositions one may also regard the appearing of new peaks. Those peaks may be attributed to AM-1, another element of the Aveiro-Manchester titanosilicate family. As reported in the literature [64], the optimum pH value to successfully obtain AM-1 is within the range of 9.9 to 10.5 while to obtain AM-3 the pH should be between 10.4 and 10.8. The pH is then another important variable that may affect seriously the purity of the material obtained.
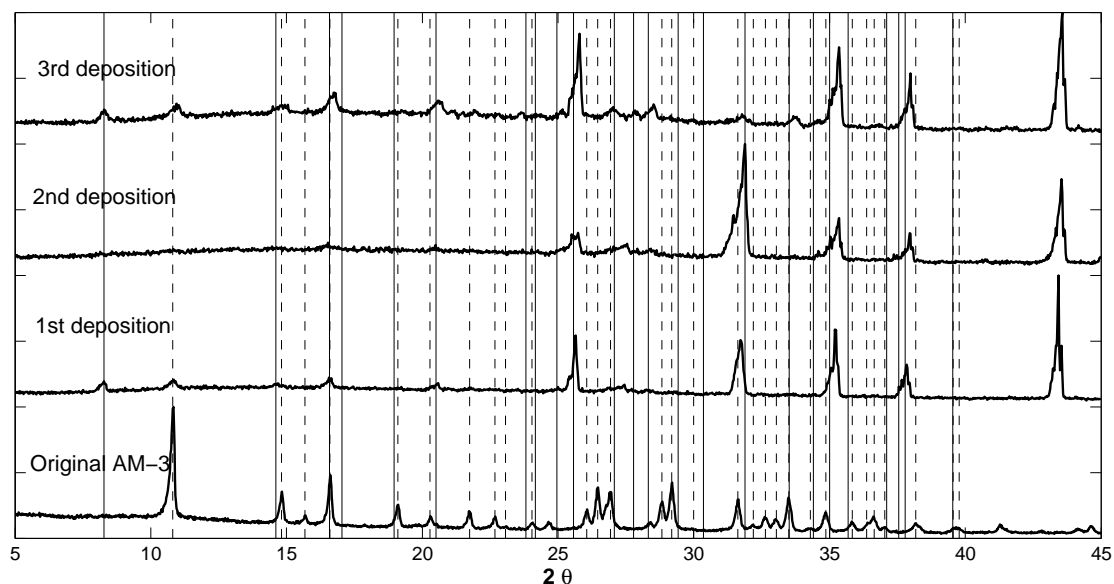
Figure 5.16: XRD patterns as function of the number of depositions on the exterior side of the membrane. Lines: full lines - AM1; dashed lines - AM-3.

In the present work the influence of the pH of the synthesis gel was also assessed. For that, five experiments were carried out in which the proportions of sodium hydroxide and sodium chloride were adjusted trying to scan a range of pH in order to evaluate its influence upon the final result. The masses of the remaining components were held constant and respected always the established proportions. The obtained pH for each experiment is presented in table 5.8 along with all used quantities.

In order to obtain values close to those reported in the literature, a dilution of the synthesis gel had to be performed. Thus, 1 g of the synthesis gel was diluted in 99 g deionized water. While reading the pH, an awkward behavior was observed. The pH meter was not able to give a steady value of pH, decreasing continuously with time. So, the values listed in table 5.8
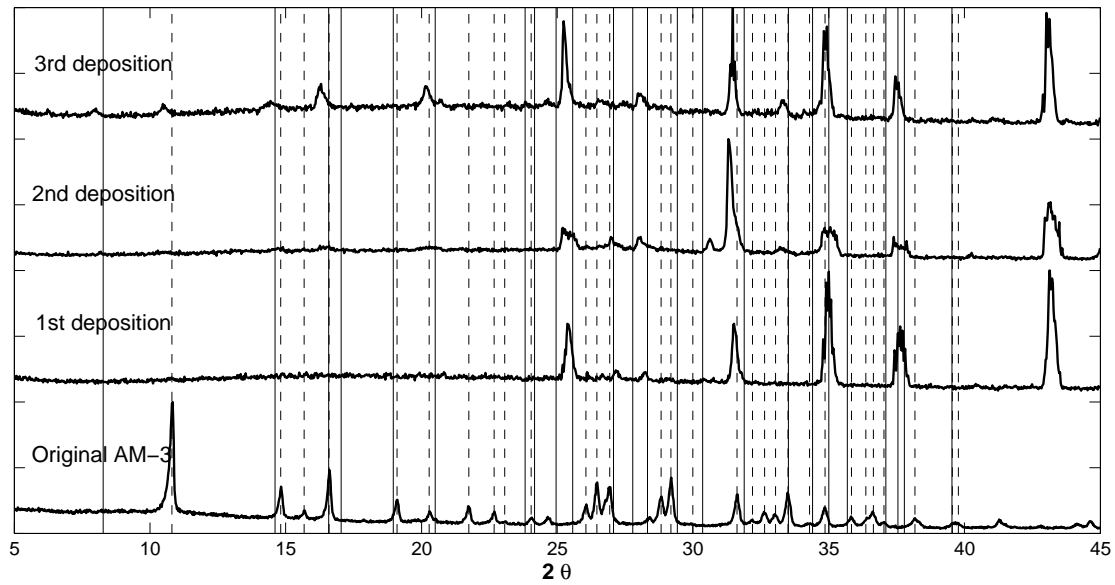
Figure 5.17: XRD patterns as function of the number of depositions on the interior side of the membrane. Lines: full lines - AM1; dashed lines - AM-3.

were obtained roughly after 5 minutes of continuous reading. The same experiment was then repeated in two different devices in order to detect any possible damage. However the same trend was observed. Additionally, another set of experiments was performed, in which the pH was measured immediately after the synthesis, aiming with that to prevent any possible oxidation of the synthesis gel, which tends to develop a lighter color with time.

Table 5.8: Mass of each component used in each experiment to assess the influence of the pH.

	Exp. 1	Exp. 2	Exp. 3	Exp. 4	Exp. 5
m_{NaOH} (g)	1.25	1.3	1.35	1.4	1.45
m_{NaCl} (g)	0.3	0.25	0.21	0.1	0.05
m_{SSS} (g)			6.42		
m_{H_2O} (g)			1.89		
m_{TiCl_3} (g)			7.14		
m_{KCl} (g)			0.55		
pH	10.055	10.136	10.152	10.209	10.254

Nevertheless, the samples obtained with this experiments were characterized by XRD and SEM. Instead of synthesizing a membrane (with a small tube) only the powder was analyzed. For that, 0.1 g of AM-3 pure seeds (provided by CICECO) were added to the gel providing the nucleation points necessary for the crystal growth.

In figure 5.18 the XRD patterns of the synthesized samples are presented and in figures 5.19 to 5.23 the SEM images for each experiment.

For the experiments 1 to 4 AM-1 is clearly present with the characteristic peak at 2θ=8.28°
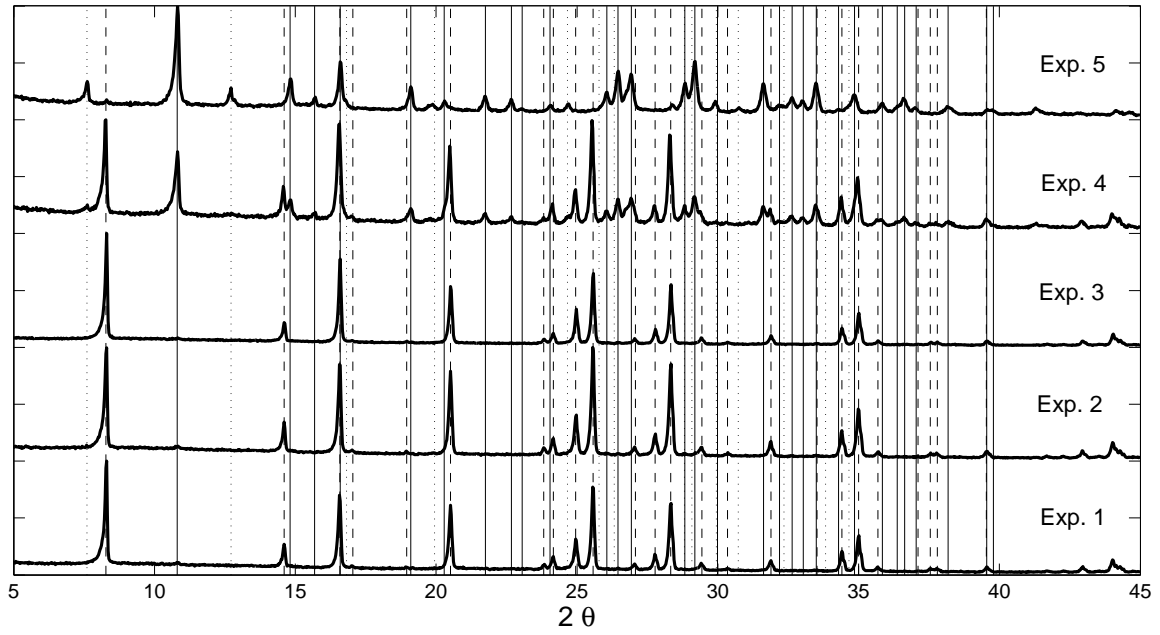
Figure 5.18: XRD patterns for each experiment of table 5.8. Lines: full lines - AM-3 pattern; dashed lines - AM-1 pattern; dotted lines - ETS-4 (titanosilicate engelhard-4) pattern.
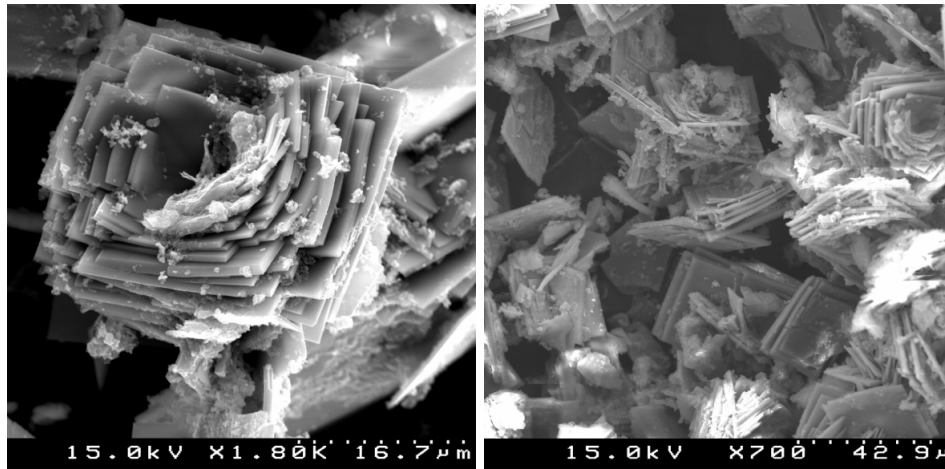
Figure 5.19: SEM images for the experiment 1.

(dashed line) confirmed by the SEM images presenting a flower-like shape. For the experiments 4 and 5, AM-3 appears with the peaks $2\theta=10.81°$ (full lines). In the experiment 5, however, the AM-1 phase is practically non-existent but the ETS-4 (titanosilicate engelhard-4) with a characteristic peak at $2\theta=7.604°$ (dotted lines). The results point out that for the conditions run, the experiments in which the sodium hydroxide content is higher (exp. 4 and 5) favor the development of AM-3, though not pure.

49
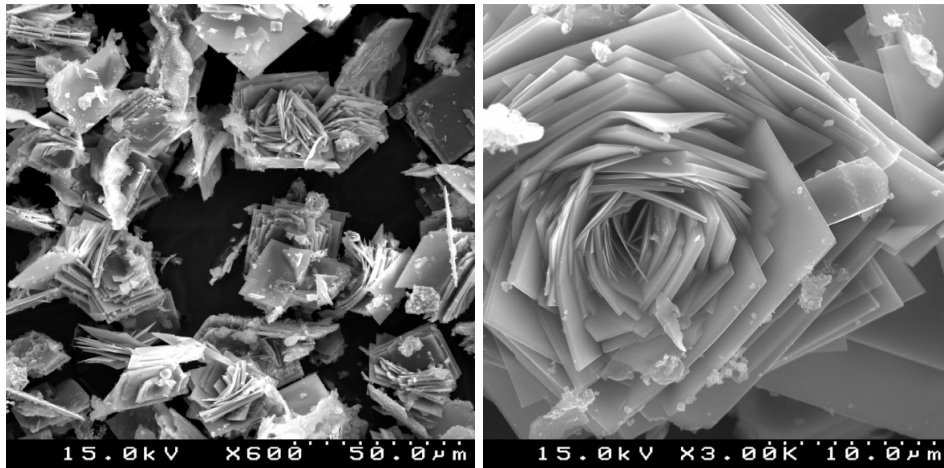
Figure 5.20: SEM images for the experiment 2.
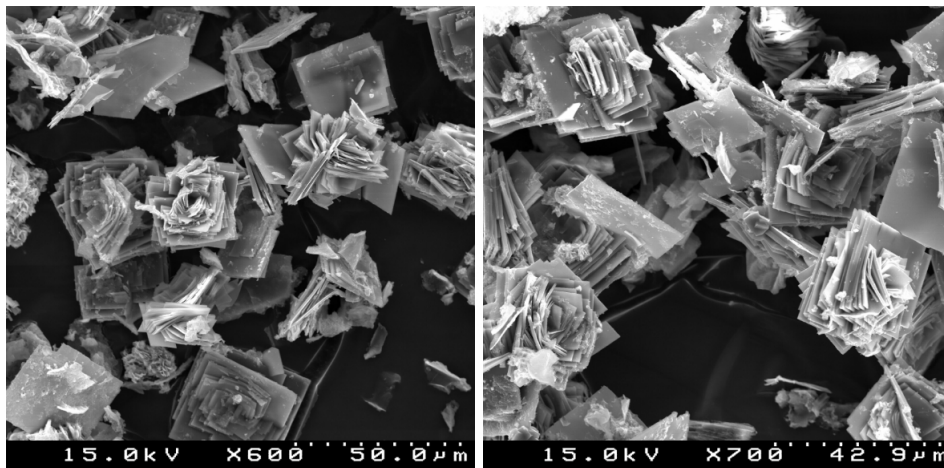
Figure 5.21: SEM images for the experiment 3.
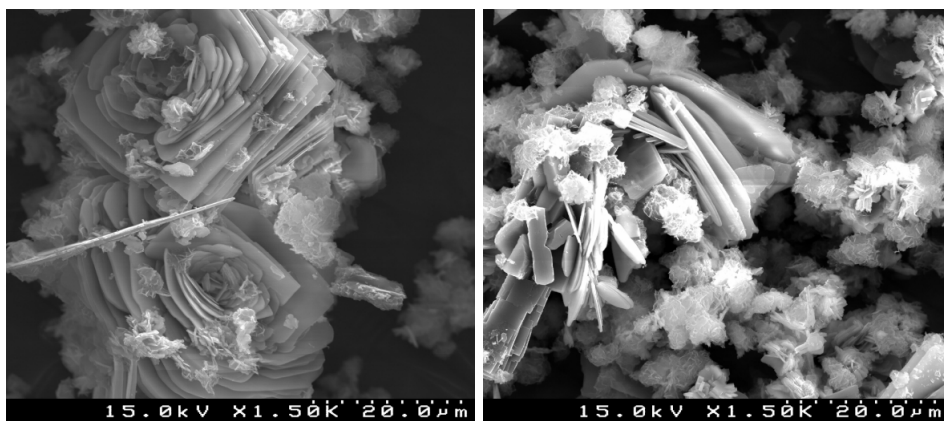
Figure 5.22: SEM images for the experiment 4.
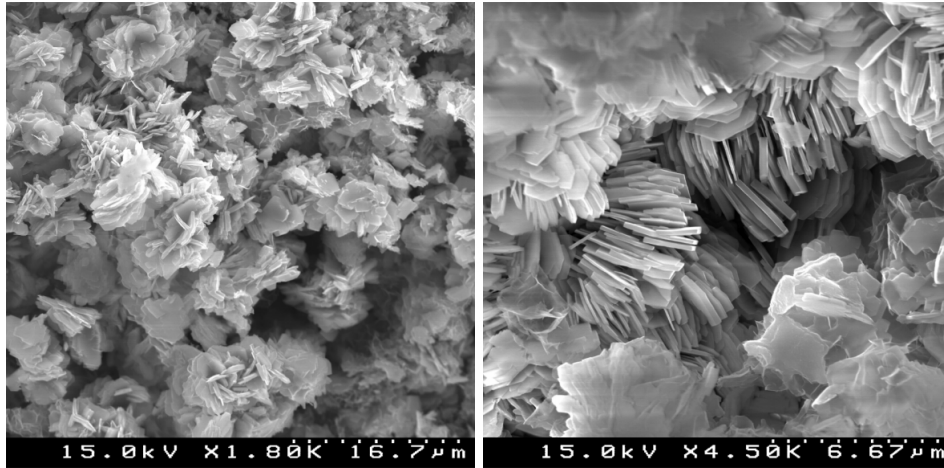
Figure 5.23: SEM images for the experiment 5.

5.2.2 Dynamic Characterization

Despite the fact that a pure AM-3 phase was not obtained, membrane permeation tests were carried out in order to assess the permeation mechanism involved and therefore, the eventual presence of defects. For that, big α-alumina supports were used and the synthesis conditions were the same as those reported in chapter 4. The permeation tests were performed using a helium flowrate of 50 cm^3 min^{-1}, with a transmembrane pressure drop of 0.5 bar, and subjecting the membranes to heating and cooling cycles during one week between the depositions in which each heating and cooling cycle has the duration of one day. In figures 5.24 and 5.25 the results after one deposition are presented and in figure 5.26 the results after two depositions.
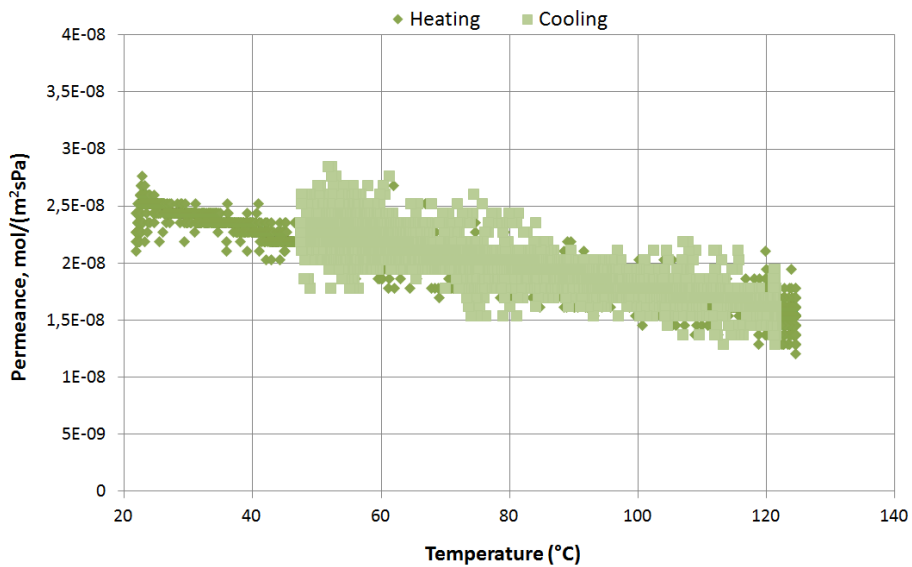
Figure 5.24: Helium permeance after one deposition and one heating and cooling cycles.
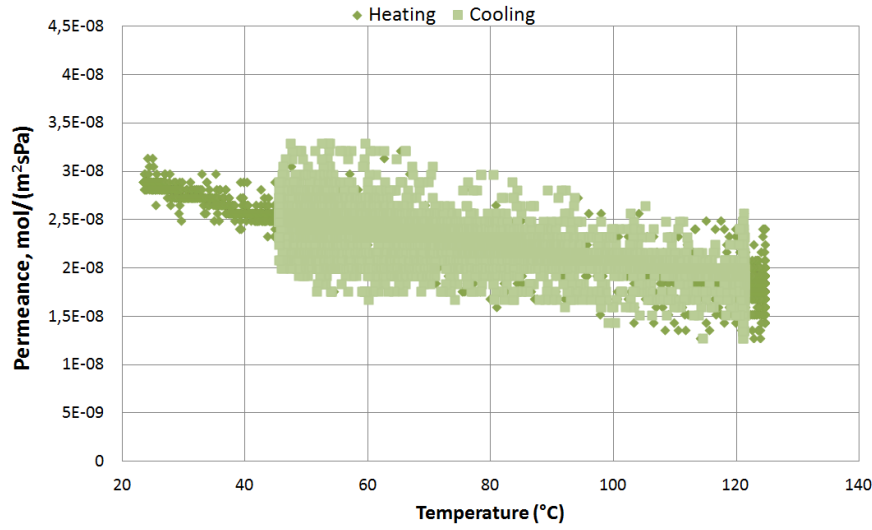
Figure 5.25: Helium permeance after one deposition and six heating and cooling cycles.
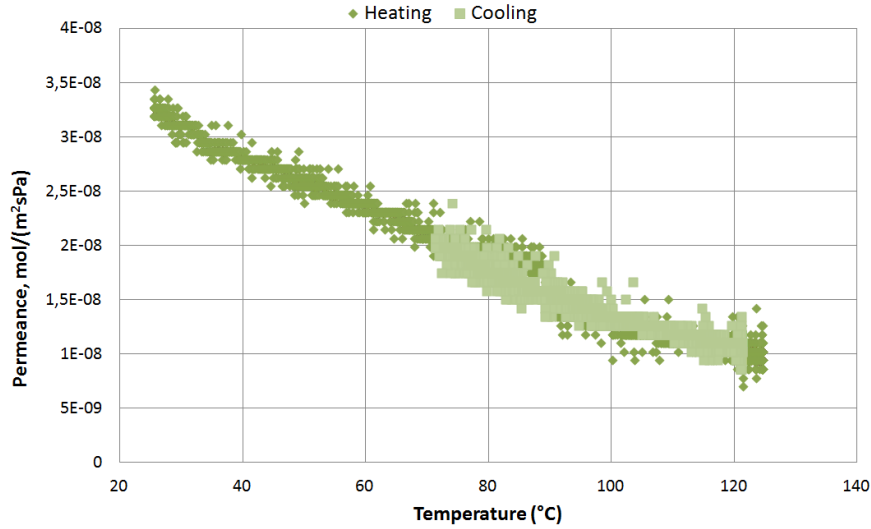
Figure 5.26: Helium permeance after two depositions and one heating and cooling cycle.

In all figures, the permeance and thus, the flux decreases with the increase of temperature. This puts in evidence the existence of macro and/or meso-deffects (see chapter 3) in which the viscous flow and/or Knudsen transport are the dominant permeating mechanisms. It is also worth to note the small increase in the permeance for the first deposition after six heating and cooling cycles revealing the presence of water blocking the membrane pores. For the second deposition, a series of heating and cooling cycles was also carried out, but there was no changes in the permeance cycle after cycle. It is important to refer that after the second deposition, the membrane itself was placed previously in an oven at 130 °C for about 24 h. Unfortunately, due to time limitations, these were the only permeation tests carried out in this work.

Chapter 6

Conclusions and future work

In this work the modeling was performed using as a solid basis the elegant Maxwell-Stefan approach. New thermodynamic factors were derived here for the first time for the Dubinin-Astakhov and Dubinin-Radushkevich isotherms. The derived thermodynamic factors pointed out that they are able to represent data for pure substances, namely, the permeation of methane and ethane through a silicalite-1 membrane and, more important they are able to predict reliably the binary permeation of those gases based only on data for pure components. The assumption initially made of zero loading dependence of the diffusivities was assessed and the results showed that it is a valid consideration, particularly for the case of ethane for which the effective diffusivities remained constant throughout the entire range of pressures considered at both 303 and 373 K. The diffusivities of methane showed a small increase with pressure particularly at 373 K. With these kinetic parameters obtained for pure methane and ethane, the permeation of a binary mixture of the two gases was purely predicted using the Vignes relation. The calculated results demonstrated the validity of this relation of the MS approach and diffusivity mixing rule for the prediction of multicomponent transport through membranes.

Furthermore, the water permeation through zeolites 13X and 4A membranes was totally predicted with diffusion and adsorption data available in the literature using once again the Maxwell-Stefan formalism applied to microporous materials. The obtained results show a higher flux for the zeolite 13X attributed to the higher diffusivities in this zeolite due to the larger pores (10 Å versus 4Å for zeolite 4A). It was also verified that the flux in the zeolite 13X decreases with increasing temperature, and the opposite was observed for the zeolite 4A, which may be explained regarding the higher variation of diffusivities for the zeolite 4A.

With respect to the synthesis of titanosilicate AM-3, a hydrothermal secondary growth technique was adopted in tubular $\alpha-$alumina supports. The static characterization pointed out that after three depositions the AM-3 becomes evident. This may be attributed to the successive increase in the number of nucleation points after each synthesis, which provides a base for subsequent crystal growth. The influence of the pH was also assessed changing

the gel composition. It was verified that, for the range of prepared compositions, it was not possible to obtain a pure AM-3 phase. Nevertheless, permeation tests were carried out using helium. After two depositions the presence of macro and/or meso-defects is clearly visible, since helium permeance decreased with increasing temperature.

Suggestions for future work

The binary thermodynamic factors derived in this work for the Dubinin-Astakhov and Dubinin-Radushkevich isotherms should be tested for other materials and permeating species, broadening their validated range of application. For that, a characterization of the physical features of the membrane should be previously performed in order to describe as accurately as possible the permeation of the species.

The separation of other gas mixtures should be studied in order to identify the real influence of temperature and loading upon diffusivities, with the objective to interpret correctly the permeation phenomenon. At this stage the literature almost always considers that the MS diffusivities are essentially constant which is not accurate.

Regarding the AM-3 membrane preparation, further attempts should be carried out and all variables involved in the synthesis process should be carefully inspected and investigated (reactants, pH, number of depositions, crystallization time, composition, among others) in order to produce a phase with a high degree of purity and a defect-free membrane.

Bibliography

[1] G. Nicoletti, N. Arcuri, G. Nicoletti, and R. Bruno. A technical and environmental comparison between hydrogen and some fossil fuels. *Energy Conversion and Management*, 89(0):205 – 213, 2015.

[2] J.D. Holladay, J. Hu, D.L. King, and Y. Wang. An overview of hydrogen production technologies. *Catalysis Today*, 139(4):244 – 260, 2009.

[3] M.V. Twigg and V. Dupont. 3 - Hydrogen production from fossil fuel and biomass feedstocks. In A. Basile and A. Iulianelli, editors, *Advances in Hydrogen Production, Storage and Distribution*, pages 43 – 84. Woodhead Publishing, 2014.

[4] B. Michalkiewicz and Z. Koren. Zeolite membranes for hydrogen production from natural gas: state of the art. *Journal of Porous Materials*, 22(3):635–646, 2015.

[5] M. Mulder. *Basic Principles of Membrane Technology*. Kluwer Academic, 1991.

[6] J.D. Seader and E.J. Henley. *Separation process principles*. Wiley, 2010.

[7] A.J. Burggraaf and L. Cot. *Fundamentals of Inorganic Membrane Science and Technology*. Membrane Science and Technology. Elsevier Science, 1996.

[8] A. Tavolaro and E. Drioli. Zeolite membranes. *Advanced Materials*, 11(12):975–996, 1999.

[9] P. F. Lito. *Caracterizaçao de Novas Membranas de Titanosilicatos Microporosos por Ensaios de Permeabilidade*. PhD thesis, University of Aveiro, 2010.

[10] T. Sun and K. Seff. Silver clusters and chemistry in zeolites. *Chemical Reviews*, 94(4):857–870, 1994.

[11] B. McCusker and D. H. Olson. In *Atlas of Zeolite Framework Types (Sixth Edition)*. 2007.

[12] S.M. Auerbach, K.A. Carrado, and P.K. Dutta. *Handbook of Zeolite Science and Technology*. Taylor & Francis, 2003.

[13] S. Tsai, P. Chao, Y. Chuang, G. H. Ho, S. Chuang, T. Tsai, C. Lee, and J. F. Huang. Study of molecular-shape selectivity of zeolites by gas chromatography. *Journal of Chemical Education*, 85(11):1558, 2008.

[14] P. F. Lito, C. F. Zhou, A. S. Santiago, A. E. Rodrigues, J. Rocha, Z. Lin, and C. M. Silva. Modelling gas permeation through new microporous titanosilicate AM-3 membranes. *Chemical Engineering Journal*, 165(2):395 – 404, 2010.

[15] P. Gorgojo, Ó. de la Iglesia, and J. Coronas. Preparation and characterization of zeolite membranes. In Reyes Mallada and Miguel Menéndez, editors, *Inorganic Membranes: Synthesis, Characterization and Applications*, volume 13 of *Membrane Science and Technology*, pages 135 – 175. Elsevier, 2008.

[16] J. Cejka. *Zeolites and Ordered Mesoporous Materials: Progress and Prospects: The 1st FEZA School on Zeolites, Prague, Czech Republic, August 20-21, 2005*. Studies in Surface Science and Catalysis. Elsevier Science, 2005.

[17] J. Caro and M. Noack. Chapter 1 - Zeolite Membranes – Status and Prospective. In Stefan Ernst, editor, *Advances in Nanoporous Materials*, volume 1 of *Advances in Nanoporous Materials*, pages 1 – 96. Elsevier, 2010.

[18] A. Julbe. Zeolite membranes—A short overview. In J. Čejka and H. van Bekkum, editors, *Zeolites and Ordered Mesoporous Materials: Progress and Prospects*, volume 157 of *Studies in Surface Science and Catalysis*, pages 135 – 160. Elsevier, 2005.

[19] Y. Lin and M. C. Duke. Recent progress in polycrystalline zeolite membrane research. *Current Opinion in Chemical Engineering*, 2(2):209 – 216, 2013.

[20] J. Caro and M. Noack. Zeolite membranes – recent developments and progress. *Microporous and Mesoporous Materials*, 115(3):215 – 233, 2008.

[21] Y. Liu, H. Du, Y. Xu, H. Ding, W. Pang, and Y. Yue. Synthesis and characterization of a novel microporous titanosilicate with a structure of penkvilksite-1M. *Microporous and Mesoporous Materials*, 28(3):511 – 517, 1999.

[22] X. Li, C. Zhou, Z. Lin, J. R., P. F. Lito, A. S. Santiago, and C. M. Silva. Titanosilicate am-3 membrane: A new potential candidate for H_2 separation. *Microporous and Mesoporous Materials*, 137(1–3):43 – 48, 2011.

[23] J. Rocha and M. W. Anderson. Microporous titanosilicates and other novel mixed octahedral-tetrahedral framework oxides. *European Journal of Inorganic Chemistry*, 2000(5):801–818, 2000.

[24] Z. Lin, J. Rocha, P. Brandão, A. Ferreira, A. P. Esculcas, J. D. P. de Jesus, A. Philippou, and M. W. Anderson. Synthesis and structural characterization of microporous umbite, penkvilksite, and other titanosilicates. *The Journal of Physical Chemistry B*, 101(36):7114–7120, 1997.

[25] R. Mallada and M. Menéndez. *Inorganic Membranes: Synthesis, Characterization and Applications: Synthesis, Characterization and Applications*. Membrane Science and Technology. Elsevier Science, 2008.

[26] T. Q. Gardner, J. L. Falconer, R. D. Noble, and M. M.P. Zieverink. Analysis of transient permeation fluxes into and out of membranes for adsorption measurements. *Chemical Engineering Science*, 58(10):2103 – 2112, 2003.

[27] P. F. Lito, S. P. Cardoso, A. E. Rodrigues, and C. M. Silva. Kinetic modeling of pure and multicomponent gas permeation through microporous membranes: Diffusion mechanisms and influence of isotherm type. *Separation & Purification Reviews*, 44(4):283–307, 2015.

[28] R. Krishna. Multicomponent surface diffusion of adsorbed species: a description based on the generalized Maxwell-Stefan equations. *Chemical Engineering Science*, 45(7):1779 – 1791, 1990.

[29] R. Krishna and J.A. Wesselingh. The Maxwell-Stefan approach to mass transfer. *Chemical Engineering Science*, 52(6):861 – 911, 1997.

[30] J. Xiao and J. Wei. Diffusion mechanism of hydrocarbons in zeolites—I. Theory. *Chemical Engineering Science*, 47(5):1123 – 1141, 1992.

[31] J. M. van de Graaf, F. Kapteijn, and J. A. Moulijn. Methodological and operational aspects of permeation measurements on silicalite-1 membranes. *Journal of Membrane Science*, 144(1–2):87 – 104, 1998.

[32] R. Krishna. Describing the diffusion of guest molecules inside porous structures. *The Journal of Physical Chemistry C*, 113(46):19756–19781, 2009.

[33] R. Krishna and R. Baur. Modelling issues in zeolite based separation processes. *Separation and Purification Technology*, 33(3):213 – 254, 2003.

[34] R. Krishna, D. Paschek, and R. Baur. Modeling the occupancy dependence of diffusivities in zeolites. *Microporous and Mesoporous Materials*, 76(1–3):233 – 246, 2004.

[35] D. A. Reed and G. Ehrlich. Surface diffusion, atomic jump rates and thermodynamics. *Surface Science*, 102(2–3):588 – 609, 1981.

[36] J. Kangas, L. Sandström, I. Malinen, J. Hedlund, and J. Tanskanen. Maxwell–Stefan modeling of the separation of H_2 and CO_2 at high pressure in an MFI membrane. *Journal of Membrane Science*, 435(0):186 – 206, 2013.

[37] P. F. Lito, A. S. Santiago, S. P. Cardoso, B. R. Figueiredo, and C. M. Silva. New expressions for single and binary permeation through zeolite membranes for different isotherm models. *Journal of Membrane Science*, 367(1–2):21 – 32, 2011.

[38] G.O Wood. Review and comparisons of D/R models of equilibrium adsorption of binary mixtures of organic vapors on activated carbons. *Carbon*, 40(3):231 – 239, 2002.

[39] D. D. Duong. *Adsorption Analysis: Equilibria and Kinetics*. Number vol. 1 in Adsorption Analysis: Equilibria and Kinetics. Imperial College Press, 1998.

[40] K. Nieszporek. On the correct use of the Dubinin-Astakhov equation to study the mixed-gas adsorption equilibria. *Adsorption*, 8(1):45–57, 2002.

[41] V.J. Inglezakis. Solubility-normalized Dubinin–Astakhov adsorption isotherm for ion-exchange systems. *Microporous and Mesoporous Materials*, 103(1–3):72 – 81, 2007.

[42] S. Kleineidam, C. Schüth, and P. Grathwohl. Solubility-normalized combined adsorption-partitioning sorption isotherms for organic pollutants. *Environmental Science & Technology*, 36(21):4689–4697, 2002.

[43] A. Gil and P. Grange. Application of the Dubinin-Radushkevich and Dubinin-Astakhov equations in the characterization of microporous solids. *Colloids and Surfaces A: Physicochemical and Engineering Aspects*, 113(1–2):39 – 50, 1996.

[44] W. Zhu, J. M. van de Graaf, L. J. P. van den Broeke, F. Kapteijn, and J. A. Moulijn. TEOM: a unique technique for measuring adsorption properties. Light alkanes in silicalite-1. *Industrial & Engineering Chemistry Research*, 37(5):1934–1942, 1998.

[45] J. M. van de Graaf, F Kapteijn, and J. A. Moulijn. Modeling permeation of binary mixtures through zeolite membranes. *AIChE Journal*, 45(3):497–511, 1999.

[46] H. B. Abdul-Rehman, M. A. Hasanain, and K. F. Loughlin. Quaternary, ternary, binary, and pure component sorption on zeolites. 1. Light alkanes on Linde S-115 silicalite at moderate to high pressures. *Industrial & Engineering Chemistry Research*, 29(7):1525–1535, 1990.

[47] E. Buss and M. Heuchel. Adsorption equilibria of methane and tetrafluoromethane and their binary mixtures on silicalite. *J. Chem. Soc., Faraday Trans.*, 93:1621–1628, 1997.

[48] A. I. Skoulidas and D. S. Sholl. Transport diffusivities of CH_4, CF_4, He, Ne, Ar, Xe, and SF_6 in silicalite from atomistic simulations. *The Journal of Physical Chemistry B*, 106(19):5058–5067, 2002.

[49] A. I. Skoulidas and D. S. Sholl. Molecular dynamics simulations of self-diffusivities, corrected diffusivities, and transport diffusivities of light gases in four silica zeolites to assess influences of pore shape and connectivity. *The Journal of Physical Chemistry A*, 107(47):10132–10141, 2003.

[50] W. Yuan, B. Yang, B. Guo, X. Li, Y. Zuo, and W. Hu. A novel environmental control system based on membrane dehumidification. *Chinese Journal of Aeronautics*, 28(3):712 – 719, 2015.

[51] T. D. Bui, F. C., A. Nida, K. J. Chua, and K. C. Ng. Experimental and modeling analysis of membrane-based air dehumidification. *Separation and Purification Technology*, 144(0):114 – 122, 2015.

[52] R. Xing, Y.Rao, W. TeGrotenhuis, N. Canfield, F. Zheng, D. W. Winiarski, and W. Liu. Advanced thin zeolite/metal flat sheet membrane for energy efficient air dehumidification and conditioning. *Chemical Engineering Science*, 104(0):596 – 609, 2013.

[53] M. Sultan, I. I. El-Sharkawy, T. Miyazaki, B. B. Saha, and S. Koyama. An overview of solid desiccant dehumidification and air conditioning systems. *Renewable and Sustainable Energy Reviews*, 46(0):16 – 29, 2015.

[54] S.K. Henninger, F.P. Schmidt, and H.-M. Henning. Water adsorption characteristics of novel materials for heat transformation applications. *Applied Thermal Engineering*, 30(13):1692 – 1702, 2010.

[55] K. Zaw, M. Reza Safizadeh, J. Luther, and K. Ch. Ng. Analysis of a membrane based air-dehumidification unit for air conditioning in tropical climates. *Applied Thermal Engineering*, 59(1–2):370 – 379, 2013.

[56] R. Ray, D. D. Newbold, S. B. McCray, D. T. Friesen, and M. Kliss. A Novel Membrane Device for the Removal of Water Vapor and Water Droplets from Air. Technical report, July 1992.

[57] H.T. El-Dessouky, H.M. Ettouney, and W. Bouhamra. A novel air conditioning system: Membrane air drying and evaporative cooling. *Chemical Engineering Research and Design*, 78(7):999 – 1009, 2000.

[58] M. Tatlier, B. Tantekin-Ersolmaz, and A. Erdem-Şenatalar. A novel approach to enhance heat and mass transfer in adsorption heat pumps using the zeolite–water pair. *Microporous and Mesoporous Materials*, 27(1):1 – 10, 1999.

[59] P. Demontis, H. Jobic, M. A. Gonzalez, and G. B. Suffritti. Diffusion of water in zeolites nax and nay studied by quasi-elastic neutron scattering and computer simulation. *The Journal of Physical Chemistry C*, 113(28):12373–12379, 2009.

[60] H. Paoli, A. Méthivier, H. Jobic, C. Krause, H. Pfeifer, F. Stallmach, and J. Kärger. Comparative QENS and PFG NMR diffusion studies of water in zeolite NaCaA. *Microporous and Mesoporous Materials*, 55(2):147 – 158, 2002.

[61] W. Zhu, L. Gora, A.W.C. van den Berg, F. Kapteijn, J.C. Jansen, and J.A. Moulijn. Water vapour separation from permanent gases by a zeolite-4A membrane. *Journal of Membrane Science*, 253(1–2):57 – 66, 2005.

[62] A. Aittomäki and M. Härkönen. Zeolite heat pump — adsorption of methanol in synthetic zeolites 13X, 4A and 5A. *International Journal of Refrigeration*, 9(4):240 – 244, 1986.

[63] Z. Lin, J. Rocha, A. Navajas, and C. Téllez. Synthesis and characterisation of titanosilicate ets-10 membranes. *Microporous and Mesoporous Materials*, 67(1):79 – 86, 2004.

[64] A. J. Ferreira. *Síntese e Caracterização de Titanossilicatos Microporosos*. PhD thesis, University of Aveiro, 1997.

[65] J. M. van de Graaf. *Permeation and Separation Properties of Supported Silicalite-1 Membranes - A Modeling Approach*. PhD thesis, 1999.

[66] S. Farooq and I.A Karimi. Modeling support resistance in zeolite membranes. *Journal of Membrane Science*, 186(1):109 – 121, 2001.

[67] R. Krishna and R. Baur. Analytic solution of the Maxwell–Stefan equations for multicomponent permeation across a zeolite membrane. *Chemical Engineering Journal*, 97(1):37 – 45, 2004.

[68] D. Green and R. Perry. *Perry's Chemical Engineers' Handbook, Eighth Edition*. McGraw-Hill Education, 2007.

[69] S.M. Kuznicki, K.A. Thrush, and H.M. Garfinkel. Use of crystalline molecular sieves containing charged octahedral sites in cyclic desiccating processes, January 7 1993. WO Patent App. PCT/US1992/005,178.

[70] G. Cacciola, G. Restuccia, and G.H.W. van Benthem. Influence of the adsorber heat exchanger design on the performance of the heat pump system. *Applied Thermal Engineering*, 19(3):255 – 269, 1999.

[71] P. Malbrunot, D. Vidal, J. Vermesse, R. Chahine, and T. K. Bose. Adsorbent helium density measurement and its effect on adsorption isotherms at high pressure. *Langmuir*, 13(3):539–544, 1997.

Appendix A

Modeling gas permeation through silicalite-1 membrane

For single component measurements using a sweep gas (helium, in our case), the permeation may be described by Maxwell-Stefan equations for a binary mixture. The partial pressure gradient across the support layer as a result of molecular diffusion may be evaluated by

$$-\frac{1}{RT}\nabla p_i = \frac{y_{he}N_i - y_i N_{he}}{\varepsilon_{sup}\mathcal{D}_{i,he}} \qquad (A.1)$$

The sum of the mole fractions y_i and y_{he} equals unity. Additionally the average of each mole fraction is used as an approximation:

$$y_{he} = 1 - y_i \qquad (A.2)$$

$$y_i = \bar{y}_i = \frac{P_{i,inter} + P_{i,perm}}{2P_{total}} \text{ (zeolite layer faces the feed side)} \qquad (A.3)$$

$$y_i = \bar{y}_i = \frac{P_{i,inter} + P_{i,ret}}{2P_{total}} \text{ (zeolite layer faces the permeate side)} \qquad (A.4)$$

The rearrangement of equations A.1 to A.4 gives the relation for the partial pressure at the zeolite/support interface for the situation when the zeolite layer is facing the feed side (equation A.5) or when the zeolite is facing the permeate side (equation A.6):

$$P_{i,inter} = \frac{P_{i,perm}\frac{\varepsilon_{sup}\mathcal{D}_{i,he}}{RTl} + N_i - \frac{P_{i,perm}}{2P_{total}}(N_i + N_{he})}{\frac{\varepsilon_{sup}\mathcal{D}_{i,he}}{RTl} - \frac{1}{2P_{total}}(N_i + N_{he})} \qquad (A.5)$$

$$P_{i,inter} = \frac{P_{i,perm}\frac{\varepsilon_{sup}\mathcal{D}_{i,he}}{RTl} + N_i - \frac{P_{i,perm}}{2P_{total}}(N_i + N_{he})}{\frac{\varepsilon_{sup}\mathcal{D}_{i,he}}{RTl} - \frac{1}{2P_{total}}(N_i + N_{he})} \qquad (A.6)$$

When the feed is a binary mixture, three components must be included in the calculation of the pressure gradients in the support layer. The MS equation (A.1) can be extended by

just adding extra frictional terms (components i, j and helium).

$$-\frac{1}{RT}\nabla p_{\mathrm{i}} = \frac{y_{\mathrm{j}}N_{\mathrm{i}} - y_{\mathrm{i}}N_{\mathrm{j}}}{\varepsilon_{\mathrm{sup}}\mathcal{D}_{\mathrm{i,j}}} + \frac{y_{\mathrm{he}}N_{\mathrm{i}} - y_{\mathrm{i}}N_{\mathrm{he}}}{\varepsilon_{\mathrm{sup}}\mathcal{D}_{\mathrm{i,he}}} \tag{A.7}$$

For simplicity, in both single gas and binary mixture permeation experiments the counter flux of sweep gas was neglected. The main reason for that was the lack of data. Nevertheless, particularly in binary experiments, this is a reasonable assumption at temperatures up to 400 K in the presence of a strongly adsorbing component in the feed [65]. The pressure gradient of each feed component can then be evaluated as follows:

$$\begin{aligned} -\frac{1}{RT}\nabla p_1 =\ &N_1\left[\frac{(P_{2,\mathrm{perm}} + P_{2,\mathrm{inter}})}{2P_{\mathrm{total}}\mathcal{D}_{1,2}} + \frac{[2P_{\mathrm{total}} - (P_{1,\mathrm{perm}} + P_{1,\mathrm{inter}}) - (P_{2,\mathrm{perm}} + P_{2,\mathrm{inter}})]}{2P_{\mathrm{total}}\mathcal{D}_{1,\mathrm{he}}}\right] \\ &- N_2\left[\frac{(P_{1,\mathrm{perm}} + P_{1,\mathrm{inter}})}{2P_{\mathrm{total}}\mathcal{D}_{1,2}}\right] \end{aligned}$$

$$\tag{A.8}$$

For the second component a similar expression can be derived [65, 66].

Knowing the partial pressures at the permeate side, the partial pressures at the zeolite / support interface can be obtained. Starting from the permeate, with the fluxes of i and helium, one may calculate the molar fraction of the component i by:

$$y_{\mathrm{i}} = \frac{N_{\mathrm{i}}}{N_{\mathrm{he}} + N_{\mathrm{i}}} \tag{A.9}$$

With the permeate composition, the pressure at the zeolite/support interface ca be determined (equation A.5) and with the respective isotherm the surface coverage may be determined. The surface coverage on the feed side is calculated using the Maxwell-Stefan equation (equation 3.19) rewritten as:

$$\frac{d\theta}{dz} = -\frac{N_{\mathrm{i}}}{\rho q^{\mathrm{sat}}\Gamma\mathcal{D}_{\mathrm{i}}} \tag{A.10}$$

and integrated between $(z = \delta, \theta = \theta_{\mathrm{permeate}})$ and $(z = 0, \theta = \theta_{\mathrm{feed}})$. At the feed side the pressure is evaluated using the isotherm. In figure A.1 a general layout of the zeolite layer and support is depicted.

For Langmuir, Nitta, Langmuir-Freundlich and Toth isotherms, the parameters used in this work were collected from the literature [37]. For the Dubinin-Radushkevich and Dubinin-Astakhov equations, the parameters were optimized for each temperature and the above procedure was followed. The saturation pressures of methane and ethane were calculated by:

$$P_{\mathrm{sat}} = \exp(c1 + c2/T + c3\ln\mathrm{T} + c4T^{c5}) \tag{A.11}$$

where the c parameters are listed in table A.1.

(a) (b)
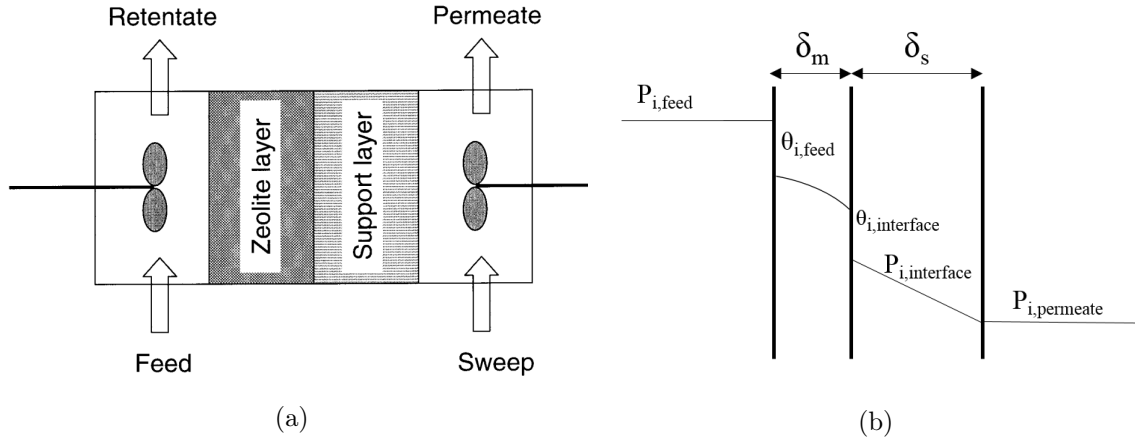
Figure A.1: General layout of the membrane and support evidencing the interfaces [67].

Table A.1: Vapor pressure parameters for methane and ethane (from [68]).

	c1	c2	c3	c4	c5	T_{min} / K	T_{max} / K
Methane	39.21	-1324.40	-3.44	3.10×10^{-5}	2	90.69	290.56
Ethane	51.86	-2598.70	-5.13	1.49×10^{-5}	2	90.35	305.32

Appendix B

Modeling water permeance through 13X and 4A membranes

In tables B.1-B.4 the diffusivity and adsorption data for zeolites 4A and 13X necessary in chapter 5 for the water permeation modeling are presented. In table B.5 the zeolite densities used in the Maxwell-Stefan equations are shown.

Table B.1: Adsorption data of water on zeolite 13X [69].

294 K		314 K		333 K	
P (Pa)	q (kg kg^{-1})	P (Pa)	q (kg kg^{-1})	P (Pa)	q (kg kg^{-1})
0	0	0	0	0	0
74.146	21.427	67.085	11.986	81.208	5.030
141.231	22.917	144.762	14.718	141.231	5.650
346.017	25.522	346.017	20.118	342.486	7.509
684.972	27.130	667.318	22.658	670.849	8.807
1331.105	28.609	1338.167	24.633	1394.659	12.521
2326.786	29.895	1998.423	25.801	2005.485	13.255
		2686.926	26.720	2729.295	16.036

Table B.2: Effective diffusivities of water on zeolite 13X [59].

350 K		400 K		450 K	
q (kg kg^{-1})	D$_{\text{eff}}$ (10^{-10} m^{2}s^{-1})	q (kg kg^{-1})	D$_{\text{eff}}$ (10^{-9} m^{2}s^{-1})	q (kg kg^{-1})	D$_{\text{eff}}$ (10^{-10} m^{2}s^{-1})
0.336	3.739	0.336	0.487	0.026	0.445
0.269	4.099	0.268	0.501	0.053	2.046
0.202	3.093	0.200	0.539	0.080	5.961
0.162	4.024	0.161	0.532	0.161	16.192
0.081	0.495	0.081	0.112	0.201	20.996
0.054	0.105	0.053	0.035	0.269	16.237
0.027	0.090	0.027	0.009	0.335	10.320

Table B.3: Adsorption data of water on zeolite 4A [70].

290 K		330 K		350 K	
P (Pa)	q (kg kg^{-1})	P (Pa)	q (kg kg^{-1})	P (Pa)	q (kg kg^{-1})
0.001	0.000	0.022	0.000	0.083	0.000
0.016	0.020	0.344	0.020	1.226	0.020
0.509	0.060	9.352	0.060	31.226	0.060
1.248	0.080	22.304	0.080	73.643	0.080
2.212	0.100	39.266	0.100	129.298	0.100
3.371	0.120	60.077	0.120	198.138	0.120
4.152	0.130	74.194	0.130	244.955	0.130
5.257	0.140	94.057	0.140	310.695	0.140
9.980	0.160	177.409	0.160	584.472	0.160
27.434	0.180	474.674	0.180	717.494	0.165
38.197	0.185	653.560	0.185		
55.170	0.190	931.548	0.190		
129.889	0.200				
212.876	0.205				
365.872	0.210				
661.237	0.215				

Table B.4: Effective diffusivities of water on zeolite 4A [60].

0.0528 (kg kg^{-1})		0.158 (kg kg^{-1})		0.264 (kg kg^{-1})	
T (K)	D_{eff} (10^{-12} m^{2}s^{-1})	T (K)	D_{eff} (10^{-12} m^{2}s^{-1})	T (K)	D_{eff} (10^{-12} m^{2}s^{-1})
434	60.183	353	119.127	374	112.828
414	57.569	333	83.298	353	94.371
394	42.091	313	51.383	333	58.209
374	20.750	298	32.556	313	28.960
353	7.149			298	15.202
333	3.027				

Table B.5: Zeolite Densities [71].

	Zeolite 13X	Zeolite 4A
ρ_{s} (kg m^{-3})	2561	2391

Appendix C

Diffusion parameters optimization - Matlab routine

This matlab routine has the purpose to optimize the diffusion parameters as described in chapter 5. For simplicity and illustrative intentions the Langmuir isotherm is the only isotherm shown here.

```matlab
%MAXWELL-STEFAN EQUATIONS
function silicalite1p ()
clear all;clc
global a
a.R=8.314;                                          %J/(mol K)

%-------------------------------------------------------------------
%MEMBRANE AND SUPPORT DATA
a.sa=2.0e-4;                              % MEMBRANE SURFACE AREA (m^2)
a.Lz=10e-6;                                % MEMBRANE THICKNESS (m)
a.rho=1.8e6/1000;                          % ZEOLITE DENSITY (kg/m^3)
a.Ls=3.0e-3;                                % SUPPORT THICKNESS (m)
a.epss=0.2;                                  % SUPPORT POROSITY (m)

%-------------------------------------------------------------------
%SWEEP GAS DATA
a.sgfl=100e-6;                                        %m^3/min
a.sgflow=a.sgfl*100000/(a.R*273.15*60);                  %mol/s

%-------------------------------------------------------------------
%TOTAL PRESSURE (PERMEATE SIDE)
a.Ptot=101325;                                        %Pa
```

```matlab
%-------------------------------------------------------------------
%ISOTHEM PARAMETERS (P. Lito, 2011)
%LANGMUIR
    %METHANE
a.qsat0langmet=2.24;                                        %(mol/kg)
a.Qstmet=14.7;                                              %(kJ/mol)
a.b0met=2.22e-6;                                             %(Pa^-1)
a.quilangmet=1.22;


    %ETHANE
a.qsat0langet=1.86;                                         %(mol/kg)
a.Qstet=28.32;                                              %(kJ/mol)
a.b0et=5.26e-5;                                              %(Pa^-1)
a.quilanget=0.38;


%-------------------------------------------------------------------------
%SINGLE PERMEATION EXPERIMENTAL DATA (van de Graaf, 1999)
    %303K
a.T01=303;                                          %TEMPERATURE (K)
a.pmetbt=[10.33; 26.85; 51.12; 76.41; 101.70       %METHANE PRESSURE(Pa)
    101.70; 205.46; 313.86; 424.29]*1000;
a.fmetbt=[5.54 ;13.86 ;26.06 ;39.37 ;52.68;        %METHANE FLUX (mol/m^2s)
    56.56 ;117.56 ;184.65 ;241.77]/1000;


a.petbt=[10.33; 26.853; 51.12; 76.41; 101.70       %ETHANE PRESSURE(Pa)
    205.46; 313.86; 424.29]*1000;
a.fetbt=[6.09; 13.30; 24.95; 33.27; 39.92          %METHANE FLUX (mol/m^2s)
    62.66; 80.96; 95.93]/1000;


    %373K
a.T02=373; %TEMPERATURE (K)
a.pmetat=[12.28; 27.12; 52.19; 77.27; 102.86       %METHANE PRESSURE(Pa)
    205.73; 313.74; 422.80]*1000;
a.fmetat=[3.70; 8.52; 17.05; 25.20; 33.73          %METHANE FLUX (mol/m^2s)
    72.27; 113.78; 154.18]/1000;


a.petat=[27.12; 52.19; 77.27; 102.86               %ETHANE PRESSURE(Pa)
    205.73; 313.74; 422.80]*1000;
a.fetat=[13.70; 25.55; 36.67; 47.78; 91.13         %METHANE FLUX (mol/m^2s)
    125.61; 151.59]/1000;


%-------------------------------------------------------------------------
%INITIAL ESTIMATES (MS DIFUSIVITIES, ACTIVATION ENERGY)
D0smet=(8e-8)^(1/4);                                        %m^2/s
Easm=(4000)^(1/2);                                          %J/mol


Eimet=[D0smet Easm];
```

67

```matlab
D0set=(1.3e-7)^(1/4);                                          %m^2/s
Easet=(16000)^(1/2);                                           %J/mol
Eiet=[D0set Easet];


%-----------------------------------------------------------------------
%OPTIMAL VALUES
    %%%LANGMUIR
    %METHANE
options=optimset('MaxIter',10000,'MaxFunEval',10000);
[Paramet fvalmetL exitflg output]=fminsearch(@fobj,Eimet,options);


Paramet(1)=Paramet(1).^4;
Paramet(2)=Paramet(2).^2;


T=a.T01;
a.R=8.314;
bLmet=a.b0met*exp(a.Qstmet*10^3/(a.R*a.T01)*(a.T01/T-1));
qsat=a.qsat0langmet*exp(a.quilangmet*(1-T/a.T01));


int_integracao=[a.Lz 0];                              %Integration range

fluxo=a.fmetbt;
Pteorica=zeros(1,length(a.fmetbt));
for i=1:length(a.fmetbt)
    P0=fluxo(i)*a.sa/(fluxo(i)*a.sa+a.sgflow)*a.Ptot;
    psuporte=(P0*a.epss*6.7e-5/(a.R*T*a.Ls)+fluxo(i)-P0/(2*a.Ptot)
        *(fluxo(i)))/(a.epss*6.7e-5/(a.R*T*a.Ls)+1/(2*a.Ptot)*(fluxo(i)));
    teta0=(bLmet*psuporte/(1+bLmet*psuporte));
    [z teta]=ode23(@EDOmet,int_integracao,teta0,[],i,Paramet,T,fluxo,qsat);
    Pteorica(i)=(teta(end)/(bLmet*(1-teta(end))));
end

figure(1)
plot(a.pmetbt,a.fmetbt,'k*',Pteorica,a.fmetbt,'k-')
hold on

T=a.T02;
bLmet=a.b0met*exp(a.Qstmet*10^3/(a.R*a.T01)*(a.T01/T-1));
qsat=a.qsat0langmet*exp(a.quilangmet*(1-T/a.T01));
fluxo=a.fmetat;
Pteorica1=zeros(1,length(a.fmetat));
for i=1:length(a.fmetat)
    P0=fluxo(i)*a.sa/(fluxo(i)*a.sa+a.sgflow)*a.Ptot;
    psuporte=(P0*a.epss*9.6e-5/(a.R*T*a.Ls)+fluxo(i)-P0/(2*a.Ptot)
        *(fluxo(i)))/(a.epss*9.6e-5/(a.R*T*a.Ls)+1/(2*a.Ptot)*(fluxo(i)));
    teta0=(bLmet*psuporte/(1+bLmet*psuporte));
    [z teta]=ode23(@EDOmet,int_integracao,teta0,[],i,Paramet,T,fluxo,qsat);
```

```matlab
    Pteorica1(i)=(teta(end)/(bLmet*(1-teta(end))));
end

figure(2)
plot(a.pmetat,a.fmetat,'k*',Pteorica1,a.fmetat,'k-')
hold on

    %ETHANE
options1=optimset('MaxIter',10000,'MaxFunEval',10000);
[Paraet fvaletL exitflg output]=fminsearch(@fobj1,Eiet,options1);

Paraet(1)=Paraet(1).^4;
Paraet(2)=Paraet(2).^2;

T=a.T01;
a.R=8.314;
bLet=a.b0et*exp(a.Qstet*10^3/(a.R*a.T01)*(a.T01/T-1));
qsat=a.qsat0langet*exp(a.quilanget*(1-T/a.T01));

int_integracao=[a.Lz 0];

fluxo=a.fetbt;
Pteorica2=zeros(1,length(a.fetbt));
for i=1:length(a.fetbt)
    P0=fluxo(i)*a.sa/(fluxo(i)*a.sa+a.sgflow)*a.Ptot;
    psuporte=(P0*a.epss*4.8e-5/(a.R*T*a.Ls)+fluxo(i)-P0/(2*a.Ptot)
    *(fluxo(i)))/(a.epss*4.8e-5/(a.R*T*a.Ls)+1/(2*a.Ptot)*(fluxo(i)));
    teta0=(bLet*psuporte/(1+bLet*psuporte));
    [z teta]=ode23(@EDOet,int_integracao,teta0,[],i,Paraet,T,fluxo,qsat);
    Pteorica2(i)=(teta(end)/(bLet*(1-teta(end))));
end

figure(1)
plot(a.petbt,a.fetbt,'ok',Pteorica2,a.fetbt,'k-')
hold on

T=a.T02;
bLet=a.b0et*exp(a.Qstet*10^3/(a.R*a.T01)*(a.T01/T-1));
qsat=a.qsat0langet*exp(a.quilanget*(1-T/a.T01));
fluxo=a.fetat;
for i=1:length(a.fetat)
    P0=fluxo(i)*a.sa/(fluxo(i)*a.sa+a.sgflow)*a.Ptot;
    psuporte=(P0*a.epss*6.9e-5/(a.R*T*a.Ls)+fluxo(i)-P0/(2*a.Ptot)
    *(fluxo(i)))/(a.epss*6.9e-5/(a.R*T*a.Ls)+1/(2*a.Ptot)*(fluxo(i)));
    teta0=(bLet*psuporte/(1+bLet*psuporte));
    [z teta]=ode23(@EDOet,int_integracao,teta0,[],i,Paraet,T,fluxo,qsat);
    Pteorica3(i)=(teta(end)/(bLet*(1-teta(end))));
```

```matlab
end

figure(2)
plot(a.petat,a.fetat,'ok',Pteorica3,a.fetat,'k-')
hold on

%------------------------------------------------------------------------
%BINARY PERMEATION EXPERIMENTAL DATA (ETHANE (1)/METHANE (2))
ethanepf=[89.559; 75.931; 52.165;
    28.049; 11.559]*1000;                       %ETHANE FEED PRESSURE (Pa)

ethanefl=[39.738; 35.163; 25.359;
    15.424; 7.320]/1000;                        %METHANE FLUX (mol/(m^2 s))
methanefl=[0.653; 1.699; 3.921;
    9.019; 21.045]/1000;                        %ETHANE FLUX (mol/(m^2 s))

int_integracao=[a.Lz 0];                        %INTEGRATION RANGE
Temp=303;                                       %TEMPERATURE
D12=1.7e-5;
D1He=4.8e-5;
D2He=6.7e-5;

%LANGMUIR ISOTHERM
Ds1=Paraet(1)*exp(-Paraet(2)/(a.R*Temp));
Ds2=Paramet(1)*exp(-Paramet(2)/(a.R*Temp));
difus=[Ds1 Ds2];

npontos=length(ethanefl);
Pteorica_etano=zeros(1,npontos);
 for j=1:npontos
    etteoflux=fliplr(ethanefl);
    metteoflux=fliplr(methanefl);
    N=[etteoflux(j); metteoflux(j)];
    P0permeate_et=etteoflux(j)*a.sa/(etteoflux(j)*a.sa
        +metteoflux(j)*a.sa+a.sgflow)*a.Ptot;
    P0permeate_met=metteoflux(j)*a.sa/(etteoflux(j)*a.sa
        +metteoflux(j)*a.sa+a.sgflow)*a.Ptot;
    P1perm=P0permeate_et;
    P2perm=P0permeate_met;
    Pinters=fsolve(@pinter,[P0permeate_et P0permeate_met],[],j,
        etteoflux,metteoflux,D12,D1He,D2He,P1perm,P2perm,Temp);
    Pinter_et=Pinters(:,1);
    Pinter_met=Pinters(:,2);
    bLet=a.b0et*exp(a.Qstet*10^3/(a.R*a.T01)*(a.T01/Temp-1));
    bLmet=a.b0met*exp(a.Qstmet*10^3/(a.R*a.T01)*(a.T01/Temp-1));

    teta10=bLet*Pinter_et/(1+bLet*Pinter_et+bLmet*Pinter_met);
```

```matlab
    teta20=bLmet*Pinter_met/(1+bLmet*Pinter_met+bLet*Pinter_et);

    [z, teta]=ode23(@sedoL,int_integracao,[teta10 teta20],[],difus,N);

    Pteorica_etano(j)=teta(end,1)/(bLet*(1-teta(end,1)-teta(end,2)));
 end

figure(3)
plot(ethanepf,ethanefl,'b*',ethanepf,methanefl,'r*')
hold on
plot(Pteorica_etano,fliplr(ethanefl),Pteorica_etano,fliplr(methanefl))
xlabel('Ethane feed pressure (Pa)')
ylabel('Flux mol/m^2s')


%------------------------------------------------------------------------
%%%%%%%%%%%%%%%%%%%%%% OBJECTIVE FUNCTIONS %%%%%%%%%%%%%%%%%%%%%%%%%
%LANGMUIR ISOTHERM
    %METHANE
function f=fobj(Paramet)
global a

Paramet(1)=Paramet(1).^4;
Paramet(2)=Paramet(2).^2;

T=a.T01;
a.R=8.314;
bLmet=a.b0met*exp(a.Qstmet*10^3/(a.R*a.T01)*(a.T01/T-1));
qsat=a.qsat0langmet*exp(a.quilangmet*(1-T/a.T01));


int_integracao=[a.Lz 0];

f=0;
fluxo=a.fmetbt;
for i=1:length(a.fmetbt)
    P0=fluxo(i)*a.sa/(fluxo(i)*a.sa+a.sgflow)*a.Ptot;
    psuporte=(P0*a.epss*6.7e-5/(a.R*T*a.Ls)+fluxo(i)-P0/(2*a.Ptot)
        *(fluxo(i)))/(a.epss*6.7e-5/(a.R*T*a.Ls)+1/(2*a.Ptot)*(fluxo(i)));
    teta0=(bLmet*psuporte/(1+bLmet*psuporte));
    [z teta]=ode23(@EDOmet,int_integracao,teta0,[],i,Paramet,T,fluxo,qsat);
    f=f+abs((teta(end)/(bLmet*(1-teta(end)))- a.pmetbt(i))/a.pmetbt(i));
    Pteorica(i)=(teta(end)/(bLmet*(1-teta(end))));
end

T=a.T02;
bLmet=a.b0met*exp(a.Qstmet*10^3/(a.R*a.T01)*(a.T01/T-1));
qsat=a.qsat0langmet*exp(a.quilangmet*(1-T/a.T01));
```

```matlab
fluxo=a.fmetat;
for i=1:length(a.fmetat)
    P0=fluxo(i)*a.sa/(fluxo(i)*a.sa+a.sgflow)*a.Ptot;
    psuporte=(P0*a.epss*9.6e-5/(a.R*T*a.Ls)+fluxo(i)-P0/(2*a.Ptot)
        *(fluxo(i)))/(a.epss*9.6e-5/(a.R*T*a.Ls)+1/(2*a.Ptot)*(fluxo(i)));
    teta0=(bLmet*psuporte/(1+bLmet*psuporte));
    [z teta]=ode23(@EDOmet,int_integracao,teta0,[],i,Paramet,T,fluxo,qsat);
    f=f+abs((teta(end)/(bLmet*(1-teta(end)))-a.pmetat(i))/a.pmetat(i));
    Pteorica1(i)=(teta(end)/(bLmet*(1-teta(end))));
end
f=f/(length(a.fmetbt)+length(a.fmetat));


    %ETHANE
function f1=fobj1(Paraet)
global a

Paraet(1)=Paraet(1).^4;
Paraet(2)=Paraet(2).^2;

T=a.T01;
a.R=8.314;
bLet=a.b0et*exp(a.Qstet*10^3/(a.R*a.T01)*(a.T01/T-1));
qsat=a.qsat0langet*exp(a.quilanget*(1-T/a.T01));


int_integracao=[a.Lz 0];


f1=0;
fluxo=a.fetbt;
for i=1:length(a.fetbt)
    P0=fluxo(i)*a.sa/(fluxo(i)*a.sa+a.sgflow)*a.Ptot;
    psuporte=(P0*a.epss*4.8e-5/(a.R*T*a.Ls)+fluxo(i)-P0/(2*a.Ptot)
        *(fluxo(i)))/(a.epss*4.8e-5/(a.R*T*a.Ls)+1/(2*a.Ptot)*(fluxo(i)));
    teta0=(bLet*psuporte/(1+bLet*psuporte));
    [z teta]=ode23(@EDOet,int_integracao,teta0,[],i,Paraet,T,fluxo,qsat);
    f1=f1+abs((teta(end)/(bLet*(1-teta(end)))- a.petbt(i))/a.petbt(i));
end

T=a.T02;
bLet=a.b0et*exp(a.Qstet*10^3/(a.R*a.T01)*(a.T01/T-1));
qsat=a.qsat0langet*exp(a.quilanget*(1-T/a.T01));
fluxo=a.fetat;
for i=1:length(a.fetat)
    P0=fluxo(i)*a.sa/(fluxo(i)*a.sa+a.sgflow)*a.Ptot;
    psuporte=(P0*a.epss*6.9e-5/(a.R*T*a.Ls)+fluxo(i)-P0/(2*a.Ptot)
        *(fluxo(i)))/(a.epss*6.9e-5/(a.R*T*a.Ls)+1/(2*a.Ptot)*(fluxo(i)));
    teta0=(bLet*psuporte/(1+bLet*psuporte));
    [z teta]=ode23(@EDOet,int_integracao,teta0,[],i,Paraet,T,fluxo,qsat);
```

```matlab
    f1=f1+abs((teta(end)/(bLet*(1-teta(end)))-a.petat(i))/a.petat(i));
end

f1=f1/(length(a.fetbt)+length(a.fetat));

%-------------------------------------------------------------------
%ODEs
%LANGMUIR
    %METHANE
function dtetadz=EDOmet(z,teta,i,Paramet,T,fluxo,qsat)
global a
Dsmet=Paramet(1)*exp(-Paramet(2)/(a.R*T));
dtetadz = -(fluxo(i)*(1-teta))/(a.rho*qsat*Dsmet);


    %ETHANE
function dtetadz=EDOet(z,teta,i,Paraet,T,fluxo,qsat)
global a
Dset=Paraet(1)*exp(-Paraet(2)/(a.R*T));
dtetadz = -(fluxo(i)*(1-teta))/(a.rho*qsat*Dset);


%-------------------------------------------------------------------
%BINARY MIXTURES ODEs (METHANE/ETHANE)
    %lANGMUIR ISOTHERM

function dtetadz=sedoL(z,thetas,difus,N)
global a

%thetas(1)=teta1
%thetas(2)=teta2

Ds12=((difus(1))^(thetas(1)/(thetas(1)+thetas(2))))
    *((difus(2))^(thetas(2)/(thetas(1)+thetas(2))));
Ds21=Ds12;

%B MATRIX (MS DIFUSIVITIES)
B(1,1)=1/difus(1)+thetas(2)/Ds12;
B(1,2)=-thetas(1)/Ds12;
B(2,1)=-thetas(2)/Ds21;
B(2,2)=1/difus(2)+thetas(1)/Ds21;

%THERMODYNAMIC FACTORS MATRIX
TauL(1,1)=1+thetas(1)/(1-(thetas(1)+thetas(2)));
TauL(1,2)=thetas(1)/(1-(thetas(1)+thetas(2)));
TauL(2,1)=thetas(2)/(1-(thetas(1)+thetas(2)));
TauL(2,2)=1+thetas(2)/(1-(thetas(1)+thetas(2)));

qsat=mean([a.qsat0langmet a.qsat0langet]);
```

```matlab
%dethetasdz(1)=Etano
%dthetasdz(2)=Metano
dtetadz=-inv(TauL)*B*N/(a.rho*qsat);


    %INTER PRESSURE
function f=pinter(x,i,etteoflux,metteoflux,D12,D1He,D2He,P1perm,P2perm,T)
global a

%x(1)=P1,inter ----> Ethane
%x(2)=P2,inter ----> Methane

f=[x(1)-(P1perm*(a.epss/(a.R*T*a.Ls)-1/(2*a.Ptot)
    *(etteoflux(i)/D1He+metteoflux(i)/D12))+etteoflux(i)/(2*a.Ptot)
        *((P2perm+x(2))/D12+(2*a.Ptot-(P2perm+x(2)))/D1He))/
            (a.epss/(a.R*T*a.Ls)+(etteoflux(i)/D1He+metteoflux(i)/D12)
                /(2*a.Ptot));
    x(2)-(P2perm*(a.epss/(a.R*T*a.Ls)-1/(2*a.Ptot)
        *(etteoflux(i)/D12+metteoflux(i)/D2He))+metteoflux(i)/(2*a.Ptot)
            *((P1perm+x(1))/D12+(2*a.Ptot-(P1perm+x(1)))/D2He))/
                (a.epss/(a.R*T*a.Ls)+(etteoflux(i)/D12+metteoflux(i)/D1He)
                    /(2*a.Ptot))];
```

Appendix D

1/3 Simpson's rule - Matlab routine

Here the routine used to evaluate the integral of equation 5.12 to calculate the water flux on zeolites 13X and 4A is shown. The routine is based on the composite simpson's rule.

```matlab
function y = simpson(llim, ulim, incr, fun)
% Check that the provided increment has sense for our purpose
if (ulim - llim)/incr ~= floor((ulim - llim)/incr)
    disp('Warning:equal subintervals are required')
    disp('Change the increment')
    y = 'error';
    return
end
% Evaluate the function in the lower and upper limits
y1 = feval(fun, llim); y2 = feval(fun, ulim);
% Initialize the intervals
c = 0; d = 0;
% Loop for each subinterval
for i = 1 : (upper_lim - lower_lim)/incr - 0.5;
    % Calculate the function at each subinterval
    y = feval(fun, llim + i*incr);
    % Interval even or odd?
    if i/2 == floor(i/2)
        % Sum all even-interval function values
        d = d + y;
        continue
    else
        % Sum all odd-interval function values
        c = c + y;
        continue
    end
end
% Numerical Value
y = incr/3 * (y1 + 4*c + 2*d + y2);
```